BEYOND SPONTANEOUS RAMAN SCATTERING:

RESONANT, COHERENT AND SURFACE ENHANCEMENTS FOR RAMAN SPECTROSCOPY

A Dissertation

by

ANTON SHUTOV

Submitted to the Office of Graduate and Professional Studies of
Texas A&M University
in partial fulfillment of the requirements for the degree of

DOCTOR OF PHILOSOPHY

Chair of Committee,	Marlan O. Scully
Committee Members,	Alexei V. Sokolov
	Olga Kocharovskaya
	Philip R. Hemmer
	Vladislav V. Yakovlev
	Aleksei M. Zheltikov
Head of Department,	Grigory Rogachev

May 2020

Major Subject: Physics

ABSTRACT

Since the discovery of Raman scattering at the beginning of the 20th century, spontaneous Raman spectroscopy has developed into a powerful tool for the study of matter. By probing vibrational and rotational molecular oscillations, Raman spectroscopy facilitates remote detection and identification of chemicals, allows to study a chemical structure of materials, permits close monitoring of chemical reactions, and more. The main disadvantage of the spontaneous Raman effect is its low efficiency, as typically only a small fraction of the scattered photons carries information about vibrational modes of the analyte. Hence, one has to increase the light intensity and use long acquisition times to achieve a reasonable signal-to-noise ratio. These factors limit the application of spontaneous Raman spectroscopy to probe low concentrations of analyte, to analyze chemicals with low damage threshold, and to monitor rapidly changing systems. Fortunately, this drawback can be overcome by exploiting the phenomena of resonant, coherent and surface enhancements of Raman scattering. Actually, these effects not only increase the Raman scattering efficiency but represent distinct spectroscopic techniques: deep ultraviolet (DUV) Raman spectroscopy, coherent anti-Stokes Raman scattering (CARS) spectroscopy, surface-enhanced Raman scattering, and surface-enhanced CARS spectroscopies (SERS and SECARS).

Besides yielding higher signals than spontaneous Raman spectroscopy, these techniques provide additional spectroscopic data which is complementary to the vibrational-rotational spectrum. They offer additional means of examining electronic

molecular structure, evolution of chemical reactions, and imaging of dynamic systems such as gas flows, among other phenomena.

In this dissertation we will demonstrate the advantages of the DUV Raman spectroscopy, CARS and, especially, SECARS over spontaneous Raman scattering spectroscopy. We will describe the mechanism responsible for the superiority of the abovementioned techniques over spontaneous Raman spectroscopy, however we will focus on the experimental implementation of each of these methods. We will briefly outline the basic physical principles of non-resonance and resonance Raman scattering and demonstrate how the resonant enhancements can be exploited in DUV Raman spectroscopy. As an experimental demonstration, we will show the tunable laser system specifically designed for this application. Then, we will provide an example of a CARS spectroscopic system designed to measure gas concentrations and to image gas flows. Finally, we will show the surface enhancement of the semiconductor nanoparticles used in SECARS spectroscopy of pyridine-ethanol complexes. The application of the semiconductor nanoparticles results in over 9 orders of magnitude stronger signals than regular CARS spectroscopy. This application promises to yield highly customized and affordable semiconductor nanoparticles (instead of metallic) in SECARS spectroscopy. Ultimately, the demonstrated combination of methods and enhancements opens a path towards the spectroscopy of nano-analytes and, ultimately, of single molecules.

DEDICATION

To my wife and parents.

ACKNOWLEDGEMENTS

During the 6 years of my PhD program at Texas A&M University, I have grown significantly both professionally and personally and gained a great basis of skills and techniques to develop my future career. All of this would not be possible without many people: colleagues, mentors and friends, who helped and guided me through this journey.

First, I would like to gratefully thank my advisor, Professor Marlan Scully, for his financial and academic support through these years. His passion for physics and nature will always serve as an example of a pure scientist for me. I am also thankful to the members of my committee: Professors Alexei Sokolov, Olga Kocharovskaya, Phillip Hemmer, Vladislav Yakovlev, and Aleksei Zheltikov. I have had the honor to work closely with each of them and all of them mentored me during my research. I would like to extend my sincere thanks to Professors Alexey Belyanin, Tatiana Erukhimova, Edward Fry, David Lee, Valery Pokrovsky, and Suhail Zubairy for their support and passion about teaching physics.

I am especially thankful to Dr. Alexander Goltsov and Dr. Georgi Petrov, who taught me the vast majority of the experimental skills and techniques I know now. Also, I am grateful for the working experience with all my colleagues, many of whom became close friends: Timur Akhmedzhanov, Narangerel Altangerel, Aysan Bahari, Tuguldur Begzjav, Jonathan Ben-Benjamin, Sean Blakley, Kim Chapin, Anton Classen, Dominik Doktor, Ben Faltesek, Mariya Khmelenko, Barnabas Kim, Fu Li, Chris Marble, Patrick McColgan, Dawson Nodurft, Sean O'Connor, Esther Ocola, Dmitri Pestov, Gavriil Shchedrin, Yujie Shen, Alexander Sinyukov, Ben Strycker, Jonathan Thompson, Dmitri Voronine, Jizhou

Wang, Zhenhuan Yi, Alexandra Zhdanova, He Zhe, and Peter Zhokhov. Moreover, I would like to thank Dr. Zheltikov's group at the Russian Quantum Center: Ilya Fedotov, Alexander Mitrofanov, Maxim Nazarov, Mikhail Rozhko, Sergey Ryabchuk, Evgenii Serebryannikov, Alexander Voronin, Professors Andrey Fedotov and Dmitry Sidorov-Biryukov, who welcomed me to their group during a very difficult time for me.

My gratitude also goes to my Russian *alma mater*: Moscow Institute of Physics and Technology and the professors and staff there. In particular, I would like to thank Professors Alexander V. Fedorov and Yuri V. Manoshkin for their inspiration to study physics and optics, as well as their encouragement and guidance during my application to graduate school.

I thank my friends and classmates in Russia and USA: Alexander Anisimov, Roman Dmitriev, Pavel Galeev, Andrey Pacera, Pavel Rogozhkin, Sergey Sazonov, and Dmitri Sipiev for cheering me up during my darkest times.

Finally, I cannot express enough gratitude to my wonderful family: Alla, Aleksei and Aleksei Pulkin, Svetlana Kozlova, Yuri and Natalia Shvydko. They always support me and provide me with constant inspiration and hope. They taught me to be honest, dedicated and responsible in every aspect of my life, including work. Lastly, I express my heartfelt gratitude to my beloved wife, Mariia Shutova. She is a constant source of encouragement, stimulus and motivation for me, and I cannot say enough to express my appreciation of what she does for me every day. My "PhD journey" would not have been possible without her.

CONTRIBUTORS AND FUNDING SOURCES

Contributors

This work was supervised by a dissertation committee consisting of Professor Marlan O. Scully – advisor, Professors Alexei V. Sokolov, Olga Kocharovskaya, and Aleksei M. Zheltikov of the Department of Physics and Astronomy, Professor Philip Hemmer of the Department of Electrical and Computer Engineering, and Professor Vladislav V. Yakovlev of the Department of Biomedical Engineering.

Part of the data analyzed in Chapter 3 was provided by Doctor Dmitry Pestov and Professor Alexei V. Sokolov.

All other work conducted for the dissertation was completed by the student independently.

Funding Sources

Graduate study was supported by the Herman F. Heep and Minnie Belle Heep Texas A&M University Endowed Fund held/administered by the Texas A&M Foundation.

NOMENCLATURE

BBO	Beta Barium Borate
BiBO	Bismuth Borate
BPF	Bandpass filter
BS	Beamsplitter
CARS	Coherent anti-Stokes Raman scattering
CCD	Charge-coupled device
CSRS	Coherent Stokes Raman scattering
CW	Continuous wave
DM	Dichroic mirror
DUV	Deep ultraviolet
EF	Enhancement factor
EM	Electromagnetic
FAST	Femtosecond adaptive spectroscopic technique
FHG	Fourth harmonic generation
FWHM	Full width at half maximum
FWM	Four-waves mixing
LBO	Lithium Niobate
LPF	long wavelengths pass filter
MoS_2	Molybdenum disulfide
ND	Neutral density
NIR	Near infrared

NP	Nanoparticle
NR	Non resonant
OPA	Optical parametric amplification
SECARS	Surface-enhanced coherent anti-Stokes Raman scattering
SERS	Surface-enhanced Raman scattering
SHG	Second harmonic generation
SPF	Short wavelengths pass filter

TABLE OF CONTENTS

Page

ABSTRACT ii

DEDICATION iv

ACKNOWLEDGEMENTS v

CONTRIBUTORS AND FUNDING SOURCES vii

NOMENCLATURE viii

TABLE OF CONTENTS x

LIST OF FIGURES xii

LIST OF TABLES xvi

1. INTRODUCTION: SPONTANEOUS AND RESONANCE RAMAN SCATTERING SPECTROSCOPY 1

1.1. Conceptual framework 1
1.2. Historical perspective of Raman scattering and Raman spectroscopy 3
1.3. Spontaneous Raman Scattering 6
1.3.1. Molecular polarizability 10
1.3.2. Resonance Raman scattering 16

2. DEEP ULTRAVIOLET RAMAN SPECTROSCOPY WITH HIGLY EFFICIENT TUNABLE PICOSECOND LASER SYSTEM 21

2.1. Highly efficient tunable picosecond laser system 21
2.2. DUV Raman spectroscopy and identification of chemicals with the tunable picosecond laser system 31
2.2.1. Results 31
2.3. Conclusion 41

3. COLLINEAR FAST CARS FOR CHEMICAL MAPPING OF GASES 43

3.1. Introduction 43
3.2. Experimental Setup 45
3.3. Results and Discussion 48

3.4. Conclusion....52

4. SURFACE-ENHACED RAMAN SCATTERING AND SURFACE-ENHANCED COHERENT RAMAN SCATTERING....54

4.1. Giant chemical surface enhancement of coherent anti-Stokes Raman scattering on MoS_2....55
4.1.1. Introduction....55
4.1.2. Experimental details....59
4.1.3. Results....61
4.2. Discussion....75

5. CONCLUSION AND FUTURE OUTLOOK....81

REFERENCES....82

APPENDIX A DIPOLE RADIATION....94

APPENDIX B A THEORETICAL ESTIMATION OF RAMAN SCATTERING CROSS SECTION USING QUANTUM MECHANICS....100

APPENDIX C EXPERIMENTALLY OBTAINED RAMAN SCATTERING CROSS SECTION VALUES....111

LIST OF FIGURES

Page

Figure 1-1. Rayleigh and Raman scattering diagrams. Ω_1—incoming photon, $\omega_{Rayleigh}$—Rayleigh (elastic) scattering, ω_S—Raman scattering (Stokes), ω_{AS}—anti-Stokes, ω_R—molecular oscillation (Raman) frequency. 8

Figure 1-2. Energy level and Feynman diagrams showing the contribution of each term in the Equation 1.3. ω_1 — incident (laser) photon frequency, ω_S — Stokes photon frequency, ω_{FG} —the energy separation between the ground state and the final state. 12

Figure 1-3. Non-resonant and resonant excitation in Raman scattering, where ω_1— laser photon frequency. In the resonant case the overtones can be observed. 16

Figure 1-4. Franck-Cordon principle. During the electronic transition, a change from vibrational level to another will more likely to happen if the two vibrational wave functions overlap significantly. The diagram illustrates the overlap favors the transition with $\Delta\nu = \nu' - \nu = \pm 2$. 19

Figure 2-1. Experimental setup. BBO, LBO, BiBO – nonlinear crystals, HWP – half-wave plates, DM1,2 – dichroic mirrors, LPF – long wavelengths pass filters, SPF – short wavelengths pass filters. 23

Figure 2-2. The first stage optical parametric amplification (OPA) power and spectrum. (a) OPA signal and seed output powers at various wavelength. Inset shows the signal beam profile after the collimating lens, the scalebar is 1 mm. (b) OPA signal spectra at 877 nm and 942 nm. Dots – experiment, solid line – Voigt fit. 25

Figure 2-3. The second stage optical parametric amplification (OPA) power and cross correlation. (a) OPA signal and idler output powers at various wavelength. Inset shows the signal beam profile after the collimating lens, the scalebar is 1 mm. (b) The cross correlation of the signal pulse with the 532 nm pump at the second OPA stage. Dots: experiment; solid line: Gaussian fit. 27

Figure 2-4. Ultraviolet (UV) laser power and spectrum. (a) UV power at various wavelength. The inset shows the beam profile of the UV beam, measured after the collimating lens, the scalebar is 1 mm. (b) UV spectrum at 235.4 nm. Dots – experiment, solid line – Gaussian fit. 28

Figure 2-5. UV Raman spectrum of air. Excitation wavelength is 235.45 nm, integration time is 120 seconds. Inset shows enlarged 1350 – 1750 cm^{-1} spectral region. 29

Figure 2-6. Normalized Raman spectra of dietary (diet, black line) and regular (regular, red line) Coca Cola. Acquisition time is 5 seconds. The regular Coca Cola spectrum is offset for clarity. 33

Figure 2-7. Barium tungstate Raman spectrum. Top: barium tungstate powder, bottom: a 7M water suspension. Broad feature around 3500 cm^{-1} is the solvent band. 35

Figure 2-8. Ammonium nitrate Raman spectra. Top ammonia solid powder (acquisition time 30 s), bottom: 1.2 mg/mL solution in water (acquisition time 10 s). The peak marked by asterisk correspond to N_2 presented in the atmosphere. 36

Figure 2-9. Raman spectrum of pyrene. Acquisition time 30 s, laser power on the sample is 2 mW. 37

Figure 2-10. UV Raman spectra of different gasolines. The acquisition time is 15 seconds. The same baseline from all spectra was removed. 38

Figure 2-11. Raman spectrum of air. Top: log scale of the 1400-1700 and 2150-2500 cm^{-1} spectral regions, showing rovibrational spectra of oxygen and nitrogen molecules, correspondingly. Bottom: UV Raman spectrum, acquisition time 120 sec. 39

Figure 2-12. Gasoline Raman spectra taken with two different excitation wavelengths. The plot shows raw CCD signal with the baseline removed. The integration time in both cases is 5 seconds. 41

Figure 3-1. (a) CARS (coherent anti-stokes Raman scattering) level diagram. CARS signal is generated from the probe pulse scattering off the molecular vibration, coherently prepared by the pump (ω_{pump}) and Stokes (ω_{Stokes}) pulses, which are resonant with the Raman frequency of the molecule ($\Delta\omega_{Raman}$). v, J, v', J'—initial and final vibrational and rotational states correspondingly; (b) Phase matching CARS scheme for collinear beams configuration; (c) Experimental setup. DS1,2—delay stages. BS1,2—beamsplitters, L1–3—lenses (f = 100 mm), ND+BPF—set of neutral density and bandpass filters. 46

Figure 3-2. CARS spectrum of molecular oxygen in ambient air. Arrows mark the locations with maximum intensities, and corresponding wavenumbers and final quantum rotational numbers are given. 48

Figure 3-3. CARS signal dependence on O_2 partial pressure at constant total pressure in the cell (black circles, solid line), and at constant gas mixture at different pressures in the cell (red diamonds, dashed line). Both fittings are performed using "power1" fit in MATLAB R2016b (MathWorks, Natick, MA, USA). 95% confidence bounds are provided for each fitting parameter. 50

Figure 3-4. N_2 flow as it displaces air: (a) Setup schematics; (b) the CARS signal from O_2 in front of the nozzle. Darker regions correspond to higher concentrations of nitrogen. 51

Figure 3-5. N_2 flow as it displaces air with a flat barrier plate placed in front of the nozzle. (a) Setup schematic; (b) O_2 CARS signal from air in front of the nozzle. Darker regions correspond to higher concentrations of nitrogen. 52

Figure 4-1. Schematics of the time resolved SECARS experimental setup: (a) Energy level diagram of the CARS process. The molecular vibrational coherence is prepared by the pump (ω_{pump}) and Stokes (ω_{Stokes}) pulses. The CARS signal (ω_{CARS}) is generated by the probe pulse (ω_{probe}) scattering off the molecular vibration. (b) Time and frequency domain representations of the incident laser pulses. The narrowband (5 – 13 cm^{-1}) probe pulse has a duration of several ps, sinc-shape and is delayed ($\Delta\tau$) with respect to the broadband fs pump/Stokes pulses, which are two-photon resonant with the molecular vibrational modes ($\Delta\omega_{Raman}$). (c) Schematic of the (SE)CARS signal generation. The collinearly propagating pump, Stokes and probe beams are focused into the sample cell containing a mixture of pyridine (Py) and ethanol (EtOH) molecules, as well as MoS_2 nanoparticles and their complexes. The CARS signal is generated in the focal spot of the lasers and is collected in the same direction as the propagating laser beams. 59

Figure 4-2. CARS 2D spectrograms show the normalized intensity (log) of the CARS signal as a function of the Raman shift and probe pulse time delay for two slit sizes (10 μm for a, c, e and 180 μm for b, d, f) of pure pyridine (a, b), pyridine-MoS_2-ethanol solution (c, d), and pyridine-ethanol solution (e, f). The mole fraction of ethanol for all cases in (c) – (f) is the same. Horizontal dashed lines mark the vibrational modes at 989, 999 and 1029 cm^{-1}. The slit size determines the spectral bandwidth of the probe pulse: 10 μm and 180 μm slit sizes correspond to the probe bandwidth of ≈5 and ≈13 cm^{-1}, respectively. 63

Figure 4-3. Spectral line profiles obtained from the 2D CARS spectrograms for various MoS_2 and ethanol concentrations. (a) 10 μm slit size: pyridine (Py, black), pyridine-ethanol solution with MoS_2 (Py+MoS_2, red), pyridine-ethanol solution without MoS_2 (Py+EtOH, blue). Vertical dashed lines

indicate the positions of 989 cm^{-1} and 999 cm^{-1} (ring breathing) and 1029 cm^{-1} (ring stretching) modes. The inset shows the zoomed spectral region of 990-1020 cm^{-1}. (b) Same as (a), but for the 180 μm slit size. (c) Spectral line profiles for different MoS_2 concentrations $N \times c_0$, where c_0 is 4.38 μg/cm^3 and N varies from 0 to 4.2, where $N = 0$ corresponds to pure pyridine (black). (d) Same as (c), but for the 180 μm slit size. All spectra are offset for clarity with the baseline removed. 65

Figure 4-4. Temporal line profiles obtained from the 2D spectrograms show dephasing dynamics of pyridine vibrational modes for the 180 μm slit size for the maximum signal intensity from (a) the 983 - 1003 cm^{-1} range (ring breathing mode) and (b) the 1023 – 1037 cm^{-1} range (ring stretching mode) along with the fitting curves. Symbols represent experimental data, and curves represent the fitting: red circles, black curves (Py) – pure pyridine; light blue squares, blue curves (Py+EtOH) – pyridine and ethanol solution without MoS_2; blue triangles, purple curves (Py+MoS_2) – pyridine-ethanol solution with MoS_2. The dashed black line shows the fit to the Py+MoS_2 experimental data, taking into account the sinc probe pulse shape (see section 4.1.3.4 for fitting details). 68

Figure 4-5. Temporal CARS intensity profiles for (a) ring breathing and (b) ring stretching vibrational modes for various MoS_2 concentrations $N \times c_0$, where c_0 is 4.38 μg/cm^3. The curves were offset for clarity. 72

Figure 4-6. Comparison of spontaneous Raman spectra of pure pyridine (Py, black solid) and pyridine-ethanol mixture with MoS_2 (Py+MoS_2, red dotted). The integration time is 120 seconds. 75

LIST OF TABLES

Page

Table 4-1 Fitting parameters for the temporal CARS maximum intensity profiles which correspond to the data shown in Figure 4-4 and Figure 4-5. The amplitudes A_i in each fit were normalized to the maximum intensity. 69

1. INTRODUCTION: SPONTANEOUS AND RESONANCE RAMAN SCATTERING SPECTROSCOPY

1.1. Conceptual framework

In this chapter we briefly describe the history of discovery of Raman scattering and development of Raman spectroscopy. We provide the basic theoretical treatment of Raman scattering and start with the classical description of Raman scattering which can correctly predict the frequency shift of scattered photons but is not suitable for more sophisticated analysis. For instance, it cannot provide the estimation of intensities of Raman scattering. Hence, we concisely outline the main results from the quantum mechanical treatment of Raman scattering, which will be especially valuable for demonstrating how the resonance and shorter wavelength enhancements can be exploited to improve Raman scattering and for performing deep ultraviolet (DUV) Raman spectroscopy.

In Chapter 2, we consider the example of the experimental implementation of DUV Raman spectroscopy. We demonstrate the design of a laser system capable of generating tunable narrowband laser pulses in 219-235 nm spectral range. The applicability of this laser for DUV Raman spectroscopy is then proved by giving examples of DUV Raman spectra of various chemicals: explosives, coke and gases.

While Raman spectroscopy using DUV laser possesses higher selectivity and chemical sensitivity advantages in comparison with measurements done with visible and near-infrared (NIR) lasers, it is still based on the spontaneous Raman scattering phenomenon. In chapter 3 we demonstrate how Raman spectroscopy can be significantly

improved by introducing molecular coherence into a system, namely exploiting the effect of coherent anti-Stokes Raman scattering (CARS). Being a nonlinear technique CARS signal typically scales as the squared number of scatters, in contrast to the linear dependence in spontaneous Raman scattering. Hence, CARS spectroscopy has an intrinsic property of fast signal acquisition and great chemical sensitivity. However, often its experimental application is limited by strong non-resonant background which obscures the Raman signal and leads the concentration dependence to deviate from the square law. In this chapter we also demonstrate how this problem can be solved by employing a pulse shaping technique and varying time delay between laser pulses.

The enhancements we can employ to improve Raman spectroscopy are not limited to resonant and coherent effects. Hence, in chapter 4 we introduce surface-enhanced Raman scattering (SERS) spectroscopy and surface-enhanced coherent anti-Stokes Raman scattering (SECARS) spectroscopy. The enhancement factor of Raman scattering intensities can theoretically reach 10^{30} with some specifically designed nanoparticles. This tremendous enhancement in SERS and SECARS comes from two kinds of mechanisms: electromagnetic and chemical. The chemical enhancement is typically smaller than the electromagnetic enhancement by 2-6 orders of magnitude for metallic nanoparticles and is sometimes omitted altogether. However, as we will demonstrate in chapter 4, for semiconductor nanoparticles such as monolayer molybdenum disulfide, the pure chemical enhancement is on the same order of magnitude as the electromagnetic enhancement of metallic nanoparticles.

1.2. Historical perspective of Raman scattering and Raman spectroscopy

It all started exactly 99 years ago, as a young scientist named Chandrashekhara Venkata (C. V.) Raman was travelling on the ship *SS Narkunda* back to his homeland, India, from the visit of England, where he met many of his famous and eminent colleagues. As he was standing on the deck of the ship and looking into the waters of the Mediterranean Sea, he was puzzled by the origins of this magnificent deep blue color. Of course, he knew that more than 20 years prior that, Lord Rayleigh published his famous results explaining the nature of the blue sky [1]. But he could not agree with the explanation that the nature of the blue color of the sea water was simply the result of the blue sky reflecting in it. He continued to outline his thoughts and as soon as the ship docked in Bombay; he sent the manuscript [2] to the editors of *Nature* journal, suggesting that the origin of the blue color of sky and water was basically the same Rayleigh scattering effect – the elastic scattering of photons.

Since then C.V. Raman became obsessed by the optical scattering phenomenon and began his studies in the laboratory at Calcutta. The early experiments were challenging, since he had to use the focused sunlight to investigate scattering phenomena in liquids due to the absence of bright light sources. Meanwhile, in 1922, Compton discovered [3] inelastic scattering of X-ray photons on electrons, and Raman felt certain that the similar phenomena can be explored with the visible part of electromagnetic spectrum. Even though Raman and his group struggled with the weak intensity of the focused sunlight, all the hard work payed off at the end. In 1928 Raman reported [4] about his discovery of "A new radiation" – some portion of the light scattered in methyl and ethyl alcohols had a

different color than the incident light. This radiation could not be the fluorescence, as it was strongly polarized. Later Raman and his group performed more thorough experiments and detection of the new radiation carefully measuring its wavelength with a spectrometer [5] and demonstrating the similar phenomena with alcohol vapors as well [6].

The rest is history now. Shortly after his remarkable discovery, Raman again was on a ship heading to Sweden, where he was awarded the Nobel prize in Physics in 1930. We should note, though, Raman was not the only person who observed this new phenomenon. It is sometimes unfairly forgotten, that in 1928, many miles away from Raman's laboratory at Calcutta, the group of Russian physicists: Leonid Mandelstam and Grigory Landsberg were studying the light scattering in crystalline quartz. Indeed, two weeks before Raman discovery at Calcutta, they observed for the first time the effect of "combinatory" scattering of light, namely the same effect as observed by Raman. Unfortunately, due to the political turbulence, they published their results [7] with some theoretical notes only few months later in June of 1928. This was one of the reasons that Raman was the only person awarded the Nobel prize for this discovery. All these peripeteias are as intriguing as they are controversial and we refer the curious reader to follow this story somewhere else [8,9].

Regardless the controversies surrounding the 1930th Nobel prize in Physics, we can undoubtedly say that the discovery of Raman scattering and, most importantly, its appropriate relation to the vibrational modes of molecules started the whole new field of Raman spectroscopy. Thousands of chemicals and compounds were verified and tested to

obtain their Raman spectra. Of course, Raman spectroscopy especially shined since the development of intense and coherent light sources – lasers. In 1962, the first laser-based Raman spectroscopy experiment was demonstrated [10], and since that the whole field was revolutionized.

Raman spectroscopy became a standard tool for probing matter, since it is noninvasive and nondestructive. The field had been consciously improving with the improvement of spectrographs efficiency and development of more sensitive detectors, such as photomultiplier tubes (PMT) and charge-couple devices (CCD) [11]. Moreover, development of technologies had led to implementing new schemes in Raman spectroscopy: Fourier transform Raman spectroscopy [12], resonance Raman spectroscopy [13] and surface-enhanced Raman spectroscopy (SERS) [14,15]. Finally, the progress in laser engineering and availability of powerful laser sources led to the experimental implementation of nonlinear Raman spectroscopy, based on coherent anti-Stokes Raman scattering (CARS) [16,17].

With new techniques and technologies, scientist tried to overcome the main drawback of Raman spectroscopy, namely its low efficiency. Low values of spontaneous Raman scattering cross sections force to use long acquisition times (from seconds to minutes) in spectroscopic measurements. This fact, along with commonly presented fluorescent background, significantly impede the implementation of Raman spectroscopy for low-scattering medium (such as gases), dynamic chemical and biological systems and limits its application for remote sensing and rapid identification of chemicals. However, the resonance, coherent and surface enhancement can help to overcome these issues, as it will

be later demonstrated in this work. These enhancements have a different physical nature, but sometimes can be used together to yield an astonishing enhancement factors and sensitivity. But before proceeding to their experimental implementations, it will be instructional and helpful to understand the very basics of Raman spectroscopy and outline the fundamentals of spontaneous Raman scattering.

1.3. Spontaneous Raman Scattering

The complete development of the light scattering theory is beyond the scope of this work and can be found elsewhere [18]. Here, we will mainly focus on the fundamentals of the problem and outline several important consequences from the quantum mechanical treatment of Raman scattering. They will help us to understand how, for instance, the proximity of excited electronic levels of a molecule leads to a resonant enhancement in spontaneous Raman scattering. We note that the classical description of Raman scattering is possible, and, indeed, can correctly predict the frequency shifts and some symmetry selection rules (see for example Long [18], section 3). However, it cannot provide any information about intensities of Raman transitions or resonance effects.

In both the classical and quantum mechanical treatments, the source of scattered radiation is considered to be the oscillating the electric and magnetic multipole moments induced in a molecule by the electromagnetic fields of the incident light waves. Here we will consider the electrical dipole contribution in the scattering as the dominant factor. Hence, the incoming EM wave interacts with the molecule (which size is much smaller than the wavelength of the EM wave) and oscillating electric field induces an oscillating

dipole moment μ when electrons are moved back and forth. The molecule becomes polarized and most of the induced dipoles radiate (for the dipole radiation treatment see Appendix A and Griffiths [19] pp. 443-455) at the same frequency as incoming EM wave, which results in Rayleigh scattering. However, small fraction will radiate at the shifted frequency due to the intrinsic oscillations of the molecule (vibrations and rotations), producing Raman scattering. This frequency shift in Stokes (redshifted) and anti-Stokes (blueshifted) radiation equals to the molecular vibrational or rotational frequency.

The frequency shifts are easier to understand if we draw the level diagram of scattering process (Figure 1-1). The incoming photons $\omega_1$are scattered on some diatomic molecules. From Boltzmann thermal distribution, we know that at room temperature most of the molecules (although not all) are in the lowest vibrational level ($|G>$). Hence, if the energy of incoming photons ω_1 is much lower than the electronic excitation energy (non-resonance case), the intermediate state of the molecule after absorption ω_1 photon is "virtual" (showed by dash line). The virtual states are not the solutions of the time-dependent Schrodinger equation and do not correspond to a well-defined value of energy. Thus, they are short lived because of the uncertainty principle. After the absorption, the molecule quickly (within a few femtoseconds) reradiates and scattered photons are emitted. The major fraction of the emitted photons has the same frequency ($\omega_{Rayleigh} = \omega_1$, Rayleigh scattering) and the molecule is left in the ground state. Raman Stokes scattering involves the promotion of molecule into excited vibrational (or rotational) level $|F>$. Therefore, the emitted Stokes photon has smaller energy satisfying the energy conservation law ($\omega_S = \omega_1 - \Delta\omega_{FG}$). The similar argument applies to anti-

Stokes scattering, where the scattered photon has frequency ω_{AS} ($\omega_{AS} = \omega_1 + \Delta\omega_{FG}$). As mentioned earlier, at room temperature the thermal population of excited vibrational levels other than any some low-energy levels is expected to be small, so the ratio between Stokes and anti-Stokes scattering can be used for the temperature measurements. As we will see shortly, the exact intensities of scattered light are mainly determined by the transition dipole elements involving the ground, excited and all intermediate states of the molecule.

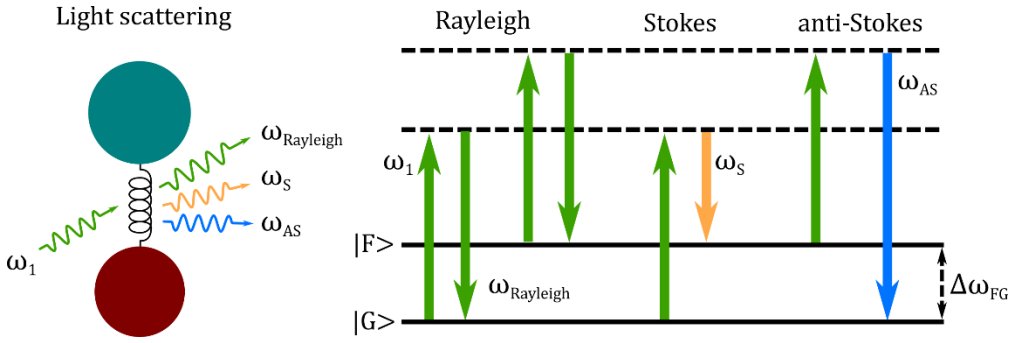

Figure 1-1. Rayleigh and Raman scattering diagrams. Ω_1—incoming photon, $\omega_{Rayleigh}$—Rayleigh (elastic) scattering, ω_S—Raman scattering (Stokes), ω_{AS}—anti-Stokes, ω_R—molecular oscillation (Raman) frequency.

Let us consider the scattering process of the initial beam of photons with intensity I_0 and frequency ω_1 averaged over all molecular orientations. During this event the molecule suffers a transition from the ground state $|G>$ to the exited state $|F>$. Then the amount of scattered light at frequency ω_S ($\omega_{AS} = \omega_1 - \Delta\omega_{FG}$) in rad/s, $I_{G,F}$, can be related with the Raman scattering cross section (for details see Appendix B and [20,21]):

$$I_{G,F} = \sigma_{Ram}(G,F) I_0 \,, \tag{1.1}$$

where

$$\sigma_{Ram}(G,F) = K\left(\frac{\omega_s^3 \omega_1}{c^4}\right)\left|\alpha_{G,F}\right|^2. \tag{1.2}$$

Here c is the speed of light, $\sigma_{Ram}(G,F)$ is the Raman scattering cross section, $\left|\alpha_{G,F}\right|^2$ is the molecular polarizability tensor, and K – numerical constant, which value depends on molecular orientation and light polarization. For the case, where the total (the whole scattering sphere) radiation is averaged over all possible molecular orientations and all polarizations, the value of K is $8\pi/9$. The value of $I_{G,F}$ is given in photons sec^{-1}, while I_0 is the flux photons in $sec^{-1}\cdot cm^{-2}$, so we see that σ_{Ram} (per orientationally averaged scattering center) indeed has the dimensionality of a true cross section: centimeters squared. It also became clear, that the dimensionality of the polarizability is cm^3 in the units used, *i.e.* in the centimeter–gram–second (CGS) system. They are different from SI units $C\cdot m^2\cdot V^{-1}$ but can be easily converted by multiplying the value in cm^3 by $4\pi\varepsilon_0 \times 10^{-6}$, where ε_0 is the vacuum permittivity.

The typical values for Raman scattering cross sections are on the order of 10^{-30} cm^2 (see Appendixes B and C), which is two orders of magnitude smaller than for Rayleigh scattering [22,23]. Hence, to maximize the potential of Raman scattering we can increase the laser intensity (I_0); thereby, increase the number of scattered photons. Unfortunately, the laser power cannot be increased indefinitely, as it will lead to the sample damage. Another approach we can pursue is to increase the frequency of the laser photons. Although the exact dependence of Raman scattering cross section is complicated due to the frequency dependence on the polarizability tensor, the shift of laser excitation from NIR to visible can yield an increase in Raman scattering intensity due to the fourth power dependence on the frequency of the dipole radiation.

Clearly, to fully understand the dependence of Raman scattering on the frequencies of photons and, most importantly, the molecular properties we must investigate the molecular polarizability tensor with the help of quantum mechanics.

1.3.1. Molecular polarizability

From the second order perturbation theory, the following expression for the molecular polarizability $(\alpha_{\rho,\sigma})_{GF}$ can be obtained using second order perturbation theory (see Appendix B, [24] pp.129-137 or [25] pp. 216-217):

$$\left(\alpha_{\rho\sigma}^{Raman}\right)_{GF} = \frac{1}{\hbar}\sum_{I}\left\{\frac{\langle F|\hat{r}_{\rho}|I\rangle\langle I|\hat{r}_{\sigma}|G\rangle}{\omega_{GI}-\omega_{1}-i\Gamma_{I}} + \frac{\langle F|\hat{r}_{\sigma}|I\rangle\langle I|\hat{r}_{\rho}|G\rangle}{\omega_{IF}+\omega_{1}+i\Gamma_{I}}\right\} \qquad (1.3)$$

Equation 1.3 is commonly called the Kramer Heisenberg Dirac (KHD) expression. Here $\hbar$ is Planck's CGS units, α is molecular polarizability in cm^3, while ρ and σ are the incident and scattered polarization directions. Typical orders of magnitude α^{Raman} are 10^{-26} cm^3 (or 10^{-42} $C\cdot m^2\cdot V^{-1}$) [25]. Since the Equation 1.3 is pretty much general and can be applied for any type of scattering, the summation Σ is done over all intermediate vibronic (vibrational + electronic) states of the molecule. Then, in Raman scattering process G is the ground state of the molecule, I – intermediate, and F – final as it is shown in Figure 1-2. We will consider two terms in the expression 1.3 separately, as well as the numerator and denominator [27].

As we can see, the numerator in each term includes two integrals written in standard 'bra' and 'ket' notation, where $\hat{r}_{\sigma,\rho}$ are the dipole operators. These integrals can be considered as terms which mix the ground and the excited states in order to describe the distorted electron configuration between the molecule and the light. Take, for instance,

$\langle I|\hat{r}_\sigma|G\rangle$ term. The operator $\hat{r}_\sigma$ (its mathematical process) acting on the vibronic wavefunction $|G\rangle$ and multiplying it with the intermediate state $\langle I|$ mixes these two states and then the result is summed over all states. After that, the similar process describing scattering effect takes place in the left-hand integral and leaves the molecule in the final state $|F\rangle$. Thus, the first one of the two integrals mixes the ground and the excited state and the second one mixes the excited and the final states. In other words, we conclude that the scattering can be regarded as involving all possible pathways (or mixes) through the intermediate states $|I\rangle$ which connect the initial state $|G\rangle$ and the final state $|F\rangle$. The transition is possible only when the electric dipole transition moments between the state $|G\rangle$ and both the state $|I\rangle$ and the state $|F\rangle$ are non-zero.

Before moving to the denominator terms, we note that the abovementioned process of mixture between the states described does not need necessarily start in the ground state. The second numerator described the “counterintuitive" process, where the emission of the photon occurs before the absorption. The following scenario can be easily understood by Feynman diagrams shown in Figure 1-2. Some objections can be raised against applying time-order for the perturbation treatment of non-resonance Raman scattering because of the short-lived of the virtual state. But as we will see shortly from analysis of the denominator, the second term describing virtual process in the equation 1.3 is typically much smaller than the first one and is completely negligible when resonance Raman scattering is discussed.

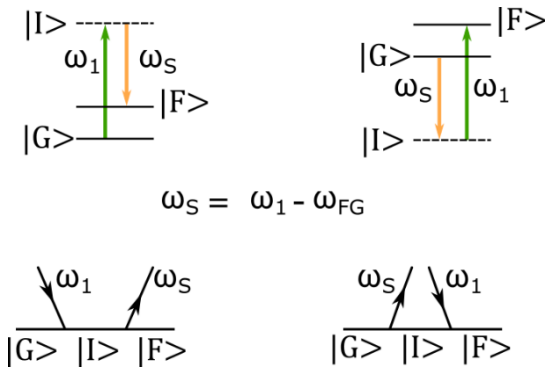

Figure 1-2. Energy level and Feynman diagrams showing the contribution of each term in the Equation 1.3. ω_1 — incident (laser) photon frequency, ω_S — Stokes photon frequency, ω_{FG} —the energy separation between the ground state and the final state.

In the denominators of both terms in KHD expression there are terms corresponding to the laser photon energy (frequency) – ω_1, along with the terms corresponding to the energy separation between levels G and I – ω_{GI} and levels F and I – ω_{IF}. The Γ_I term is the half width of the intermediate state I and is related to its lifetime τ_I through the uncertainty principle: $\tau_I = 1/(2\Gamma_I)$. Typically, Γ_I is much smaller compared to the energies ω_{GI}, ω_{IF} and ω_1, the former is on the order of $2\pi \times 10^{10} - 10^{12}$ Hz, while the later $2\pi \times 10^{14} - 10^{15}$ Hz. Hence, in the first term of the KHD expression the closer a specific excited state I is to the laser photon energy, the smaller becomes the denominator and the larger part of this particular state will play in the full expression. While, in the second term the frequencies ω_{IF} and ω_1 are added together, so the denominator will always be larger compared to that in the first term. Consequently, the second term plays a smaller role in describing the scattering process and will be neglected from here.

As stated before, the Γ_I term accounts for the final lifetime of the excited state and affects the natural breadth of Raman lines. Without it, the denominator of the first term

would go to zero when the frequency of the incident laser ω_1 equals the frequency of the electronic transition ω_{GI}. Thus, even though it is small, it is vitally important to keep this term for the latter discussion of the resonance Raman scattering.

Each of the expressions in the first term depends on the nature of the involved states and the way they are couple through the dipole moment operator. To continue our analysis of the KHD expression it is useful to implement Born Oppenheimer approximation. In this approximation the total wave function is split into separate electronic (θ), vibrational (Φ) and rotational (r) components: $\Psi = \theta \cdot \Phi \cdot r$. This approach has proved to be valid for many spectroscopic problems. The reason of that can be evident from its second name – adiabatic approximation. For instance, it works because of the difference in the timescales of electronic, vibrational and rotational transitions. The electrons are very light and in pure electronic transitions can be excited on the very short timescale (typically few femtoseconds (10^{-15} sec)) when the heavy nucleus does not significantly move. This is the reason why electronic transitions are drawn vertically in the diagrams presented in Figures Figure 1-1 and Figure 1-2. The internuclear distance plotted along x-axis cannot modify noticeably during the transition. Vibrational transitions, in turn, take place in about 10^{-12} of a second and are faster than rotational transitions. Although, the rotational-vibrational coupling is important for Raman spectroscopy of gases, and the rotational transition can be observed there, they will be omitted here for the sake of simplicity. The reader may refer to another source for the complete treatment of Raman scattering [18] including the analysis beyond the Born Oppenheimer approximation [28].

Hence, due to the different timescales, we can separate the electronic and vibrational terms. The electronic term θ will depend on both the electronic and nuclear coordinates (r and R respectively). In turn, the vibrational term Φ involved the movement of much heavier nuclei and will entirely depend on the nucleic coordinates (R). The separation of the wavefunctions allows the integrals in the numerator in the KHD expression to be split as well:

$$\langle I|\hat{r_\sigma}|G\rangle = \langle \theta_I \cdot \Phi_I|\hat{r}_\sigma(R)|\theta_G \cdot \Phi_G\rangle = \langle \theta_I|\hat{r}_\sigma(R)|\theta_G\rangle \cdot \langle \Phi_I|\Phi_G\rangle. \quad (1.4)$$

Now we can consider the electronics and vibrational parts of this equation. The Raman scattering process is so fast, that although the energy is transferred away or to the nuclei, no significant movement can occur during the scattering event. In fact, it can be said that the nuclei movements occur as small displacements around some equilibrium position defined by the chemical bond. Then the electronic term can be evaluated at this position plus the small correction term considering the change in electronic structure when the nuclei move. To make this a little simpler, let us write the electronic integral in the following form

$$\langle \theta_I|\hat{r}_\sigma(R)|\theta_G\rangle = M_{IG}(R). \quad (1.5)$$

Then the expression describing the movement of the nuclei can be expanded in a Taylor series, where the first and largest term $M_{IG}(R_0)$ is calculated at equilibrium intranuclear coordinate R_0. The second and high order terms describe the effect of movement along some particular nuclear coordinate R_ε. Higher order terms are small and will be neglected. So, the first and the second terms are written as M and M':

$$M_{IG}(R) = M_{IG}(R_0) + \left[\frac{\partial M_{IG}}{\partial R_\varepsilon}\right]_{R_0} (R_\varepsilon - R_0) + O((R_\varepsilon - R_0)^2). \quad (1.6)$$

Using these approximations, the KHD expression can be solved. We will not try to do it here, as it can be found in ref [29]. The result (up to numerical constant) is written below.

$$\left(\alpha_{\rho\sigma}^{Raman}\right)_{GF} = \frac{1}{\hbar} M_{IG}^2(R_0) \sum_I \frac{\langle \Phi_{R_F}|\Phi_{R_I}\rangle\langle \Phi_{R_I}|\Phi_{R_G}\rangle}{\omega_{GI} - \omega_1 - i\Gamma_I}$$
$$+ \frac{1}{\hbar} M_{IG}(R_0) M'_{IG}(R_0) \sum_I \frac{\langle \Phi_{R_F}|R_\varepsilon|\Phi_{R_I}\rangle\langle \Phi_{R_I}|\Phi_{R_G}\rangle + \langle \Phi_{R_F}|\Phi_{R_I}\rangle\langle \Phi_{R_I}|R_\varepsilon|\Phi_{R_G}\rangle}{\omega_{GI} - \omega_1 - i\Gamma_I}. \quad (1.7)$$

The two terms in equation 1.7 are called A-term and B-term [21]. The weighting factors $M_{IG}^2(R_0)$ and $M_{IG}(R_0)M'_{IG}(R_0)$ outside the summation signs correspond to the electronic contribution to Raman scattering, and the first factor is much larger than the second because of the small correction factor M'. The summation over all intermediate states I ensures contributes from all excited states to both A- and B-terms.

In A-term, the numerator inside the summation consists of the multiplication of all possible vibrational wave functions. The closure theorem [30] demonstrates that the multiplication of all possible vibrational wave functions is zero. In this case (non-resonance excitation), the A-term do not contribute in Raman scattering. In B-term, the coordinate operator R_ε is present in the numerator. The operator describes the effect of movement along the molecular axis during the vibration and appears because the correction term M' has been multiplied out with the vibrational states. The selection rules of the coordinate operator dictate that the only nonzero matrix elements are those having one quantum of energy difference between the initial and final states. This means that

Raman scattering spectra will consist of the transition where the vibrational quantum is changed by ± 1, and overtones are not observed or very weak. Moreover, the symmetry selection rules also became evident from here: the operators in the numerator are odd in symmetry (u). However, to obtain Raman scattering two integrals must be multiplied out together. This leads to the final result which is even (g), so the symmetric vibrations will give the most intense Raman scattering. Although, the situation changes when the laser photon frequency becomes comparable with electronic excitation energy in the resonance Raman scattering as we will discuss further.

1.3.2. Resonance Raman scattering

The Figure 1-3 shows the energy level diagrams for non-resonance and resonance Raman scattering processes. Let us analyze the KHD expression (Equation 1.3) and its solution (Equation 1.7) and see what happens under the resonance conditions.

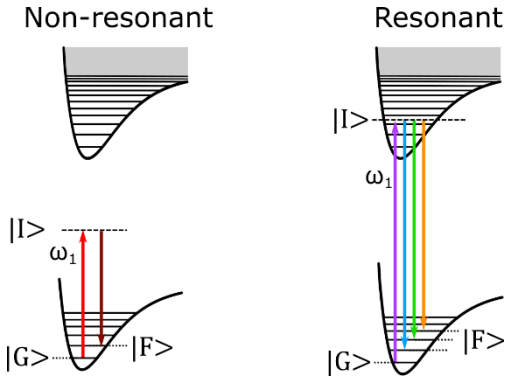

Figure 1-3. Non-resonant and resonant excitation in Raman scattering, where ω_1— laser photon frequency. In the resonant case the overtones can be observed.

The resonance condition is met when the exciting light frequency ω_1 is of the same order as the energy difference between and lowest vibrational state of the ground

electronic state G and the excited vibronic state I (ω_{GI} in KHD expression). As the denominator in the first term in KHD expression includes the difference between these two terms, at the resonance the expression in the denominator will be reduced to $i\Gamma_I$. As mentioned earlier, the value of $i\Gamma_I$ is typically much smaller than values of ω_1 and ω_{GI}, hence the first term will be much larger than in the non-resonance case, giving rise to large values of polarizability and enhancing Raman scattering. The second term in KHD expression, in turn, will have larger detuning because of the summation in the denominator and can be completely neglected.

Another important difference between the resonance and non-resonance Raman scattering can be immediately made from the analysis of the KHD expression. Under the resonance condition, most of the interactions are with the one (resonant) state, so the summation sign can be dropped. Even if the resonance is not matched exactly, the dominant contribution comes from the closest excited electronic levels, so the summation will include only few terms with the energy closest to the incoming photon frequency ω_1. As a result, the closure theorem, which states that the sum of all the vibrational matrix elements of a molecule is zero, is no longer valid. Hence, the A-term in the Equation 1.7 can give resonance Raman scattering as well as B-term. This leads to two different forms of the resonance Raman scattering which have quite different properties.

The B-term in the Equation 1.7 includes the coordinate operator R_ε allowing the transitions where there is only unit change of the vibrational quanta between the ground and the excited states ($\Delta v_{GF} = \pm 1$). Hence, the overtones, or the transitions with $\Delta v_{GF} = \pm 2, 3, \ldots$ are very weak and typically not observed in non-resonance Raman scattering. A-

term, in turn, does not have operators, so the overtones becomes allowed and there is no reason why they cannot be intense. Further, although the operator in the B-term still exists, there is no summation over all states. This fact along with the higher order terms appearing in the analysis of the KHD equation (see, for example reference [18] chapter 7), relaxes the selection rules, so overtones can be obtained even from the B-term.

The interaction of the exciting radiation with the electronic states of the molecules is different in the A- and B-terms enhancements. For instance, the in the A-term the excitation occurring during the scattering couples the ground and excited states as described previously. This type of scattering is called A-term of Franck-Condon scattering, named because of the two pioneering works by James Franck [31] and Edward Condon [32]. The electronic term M is much larger for scattering which arises from the A-term mechanism than from the B-term mechanism since it has M^2 factor as opposed to $M \times M'$. Hence, it might be expected that the A-term gives more intense spectra. However, there is another factor. To obtain the strong scattering, the transition should start from a point where there is considerable electron density in the ground state and go to the state where the save function is such that, once populated, there will also me considerable electron density. Since the transition is vertical it is called a good overlap between the wavefunctions (states) as illustrated in Figure 1-4. In addition, the selection rules must not prohibit the transition, *i.e.* the resonance enhancement will be most intense with allowed electronic transitions.

In the B-term case, two excited states become mixed through the coordinate operator R_ε, so every time the molecule moves and the geometry changes, it is needed to remix the

electronic states to obtain a new one to the molecule. This type of the enhancement is more complicated and is called B-term or Herzberg-Teller enhancement [33]. On the differences between the A-term and the B-term enhancements is that the B-term enhancement is only strong for transitions between the ground and first excited vibronic states in resonance. Although, the B-term enhancement car arise from weak or forbidden transitions.

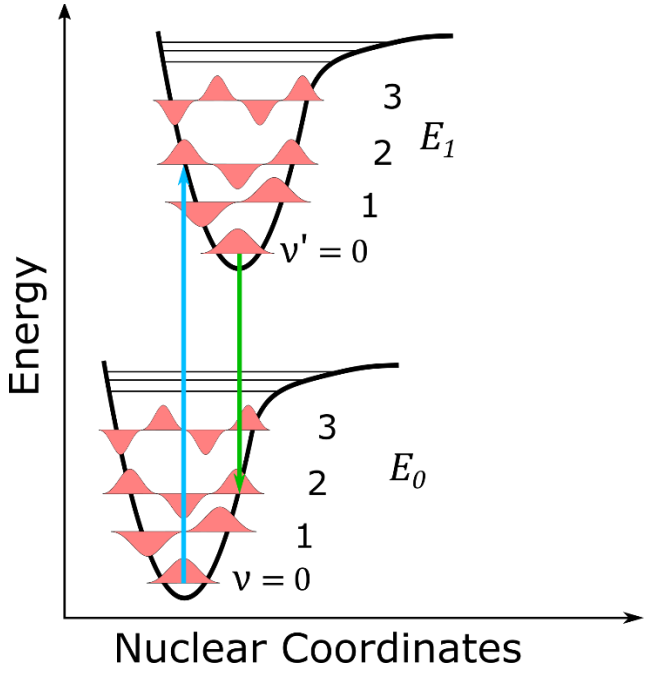

Figure 1-4. Franck-Cordon principle. During the electronic transition, a change from vibrational level to another will more likely to happen if the two vibrational wave functions overlap significantly. The diagram illustrates the overlap favors the transition with $\Delta\nu = \nu' - \nu = \pm 2$.

Since the resonance Raman scattering involves the excitation of electronic levels, the typically obtained spectrum with vibrational overtones becomes similar to the resonance fluorescence spectrum [34] and the two process can obscure each other under some conditions, for example during the studies of low pressure gas mixtures. Although the two processes look similar, they are still quite different in their physical nature. Indeed, even

if there is an excitation of the electronic states during the resonance Raman scattering, it is still an instantaneous process, happening typically 10^4 times faster than the resonance fluorescence. Moreover, the Raman scattering radiation is often polarized, in contrary to always randomly polarized fluorescence. In other words, using some experimental tools and analysis, the two processes can be easily distinguished and separated [35].

As we can see now, the resonance Raman scattering spectroscopy possesses many advantages over non-resonance spontaneous Raman spectroscopy. Namely, it provides higher scattering efficiency, better chemical selectivity due to the existence of resonances and an additional spectroscopic information about electronic molecular structure. By using the excitation light with the frequency close to the electronic resonance it becomes possible to study not only the vibrational (or rotational) spectrum of a molecule, but also its electronic configuration. However, for most of the molecules, the energy separation between the ground and excited electronic state are ≈3-6 eV, so to exploit the resonant enhancements of Raman scattering one needs a laser with the wavelength below 250 nm, or in the deep ultraviolet region. We will discuss further the deep ultraviolet Raman scattering spectroscopy and demonstrate the design of the laser system applicable for it [36].

2. DEEP ULTRAVIOLET RAMAN SPECTROSCOPY WITH HIGLY EFFICIENT TUNABLE PICOSECOND LASER SYSTEM*

2.1. Highly efficient tunable picosecond laser system

Raman spectroscopy is a powerful spectroscopic technique for non-destructive and remote characterization of chemical and structural properties of molecules based on their vibrational spectra [27]. With a huge number of emerging applications ranging from remote sensing to microscopic biomedical imaging, the major limitation of Raman spectroscopy comes from its rather moderate scattering cross section values, which is typically on the order of 10^{-30} cm^2 for the near-infrared (NIR) part of the spectrum. While approaches based on surface-enhanced Raman scattering using interaction length enhancement using specially designed cavities [37–39], plasmonic nanostructures [40], coherent Raman scattering [41,42] or even a combination of abovementioned techniques [43] provide substantial improvement in sensitivity of those measurements, those approaches are typically limited to a certain class of molecules and require special sample handling or experimental arrangements. On the other hand, resonance Raman spectroscopy allows increasing the scattering cross section by several orders of magnitude without any special requirement for sample preparation and handling [44]. By using short-wavelength excitation in the deep ultraviolet (DUV) region, i.e. 190-270 nm, one can take advantage of both the fact that the Raman scattering cross section scales as the fourth

* Part of this chapter is reprinted with permission from "Highly efficient tunable picosecond deep ultraviolet laser system for Raman spectroscopy" by A. D. Shutov, G. V. Petrov, D.-W. Wang, M. O. Scully, and V. V. Yakovlev, Opt. Lett., OL 44, 5760–5763 (2019), Copyright [2019] by Optical Society of America

power of the excitation frequency ω_s^4 and the resonant excitation. In addition to the increased signal, the fluorescence, which typically has a wavelength above 260 nm, becomes suppressed [45], if the excitation wavelength is below 250 nm.

The DUV Raman spectroscopy has proved its value in a variety of research fields, in particular the investigation of proteins structure [46,47]. The resonance enhancement allows to use relatively low excitation energies and prevent the heat damage of the fragile biological systems, while generating strong enough signal for the characterization of the proteins structure. Another field, which benefits from using the UV resonance enhancement in Raman scattering, is the remote sensing [48] and detection of the atmospheric pollution [49]. The enhancement of Raman scattering due to the higher excitation frequency provides overall signal increase and faster detection of the pollutants, while the resonance excitation can further improve the detection of trace molecules [50].

Several approaches to generation of the DUV radiation have been considered. One can use direct excimer laser excitation or the 5-th harmonic of an Nd : $Y_3Al_5O_{12}$ (Nd:YAG) laser to obtain sufficient photon flux in the DUV [51]. However, for many applications, it is desired to have tunability of the excitation wavelength, and lower energy and higher repetition rate to facilitate tight focusing geometry without worrying about saturating Raman transition [52]. Diode pumped lasers with the second harmonic generation (SHG) and fourth harmonic generation (FHG) provide a compact and cheap alternative [53], but they still lack a broad tunability. The intracavity double continuous wave (CW) Ar-ion lasers have been a working horse for DUV Raman spectroscopy [54]. These lasers can produce tens of milliwatts (mW) of power at 229, 238 and 248 nm, but they cannot be

tuned continuously, and the lifetime of those lasers is typically limited to 5,000 hours. Another approach to generate a laser radiation in UV and DUV regions, is a frequency conversion, *i.e*. a generation of the third and fourth harmonics, of a tunable high repetition rate Ti:sapphire laser [55,56]. However, the overall cost and difficulty is in maintaining a narrow bandwidth, while achieving high conversion efficiencies into the DUV. In this work we demonstrate a tunable picosecond DUV laser system capable of generation transform-limited laser pulses with up to 36 mW average power in the 219-236 nm region at a high repetition rate. We use a commercial picosecond Nd:YVO_4 laser as a pump of an optical parametric amplifier (OPA), which is seeded by a tunable continuous wave (CW) narrowband laser diode. This way we achieve transform-limited pulse operation over the whole tunability range [57]. By subsequently doubling and quadrupling the frequency, we generate tunable narrowband DUV pulses. Finally, we demonstrate the applicability of our laser system for DUV Raman spectroscopy by obtaining the high-resolution Raman spectrum of air.

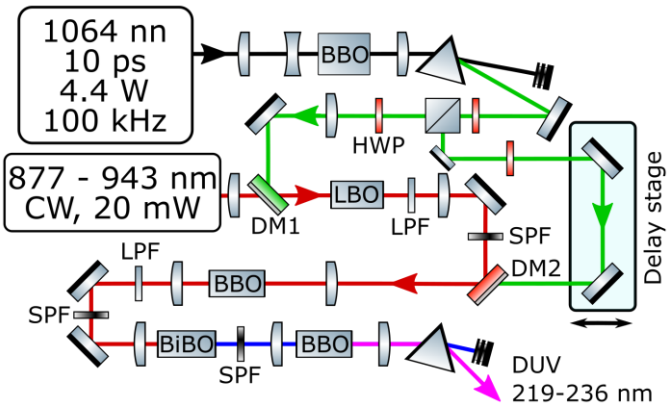

Figure 2-1. Experimental setup. BBO, LBO, BiBO – nonlinear crystals, HWP – half-wave plates, DM1,2 – dichroic mirrors, LPF – long wavelengths pass filters, SPF – short wavelengths pass filters.

The Figure 2-1 shows the experimental setup. We employ a commercial laser source (Attodyne, Inc.) which provides 1064 nm 6-10 ps pulses with the average power 4.4 W at 100 kHz repetition rate. The fundamental 1064 nm radiation after passing through the polarizer and the half waveplate is collimated by a pair of lenses into type-I BBO crystal (β-barium borate (BaB_2O_4), l = 4mm, θ = 22°) to generate the second harmonic (SH). The SH beam is separated from the fundamental by a prism and split into two channels with a half waveplate and a polarizer. We keep the beam diameter on the crystal front surface at 900 μm to prevent the optical damage of the crystal while keeping the conversion efficiency relatively high. The generated SH power is 2.7 W which corresponds to the 61% power conversion efficiency.

Approximately 20% of the generated SH power is loosely focused into the temperature-controlled LBO crystal (Lithium triborate (LiB_3O_5) x-cut crystal for non-critical phase matching, l = 20mm, φ = 0°, θ = 90°). Thus, the 532 nm beam pumps the first stage of the optical parametric amplification (OPA) of the tunable continuous wave (CW) laser diode (TEC-500-0920-030M; Sacher Lasertechnik, Ltd). The laser diode produces ≈20 mW of power, tunable between 877 and 930 nm, facilitating the generation of deep UV by the fourth harmonic (FH) between 219 and 236 nm. We keep the gain at the first stage relatively low to prevent the self-generation of the signal and idler waves in the LBO crystal and keep the amplified pulse narrowband. As a result, we generate up to 76 mW of tunable 877 – 943 nm radiation in the signal wave with the close to Gaussian beam profile (Figure 2-2(a)). At the first OPA stage the power and stability of the output signal pulse is strongly affected by the stability and power of the CW diode used as the

seed. The seed diode laser power significantly decreases in the 877 – 910 nm operating window. However, we partly compensate it by slightly increasing the pump power at the first stage, while monitoring the output spectrum (Figure 2-2(b)) with the spectrometer (InSpectrum 300 mm, Acton Research Co.). We confirm there is no self-generation, and the generated signal pulses remain narrowband. The bandwidth remains close to the 4 cm^{-1} across the whole tuning range. The absence of the self-generation component and the narrow bandwidth are crucial for the amplification at the second OPA stage and consecutive efficient generation of harmonics and UV Raman spectroscopy.

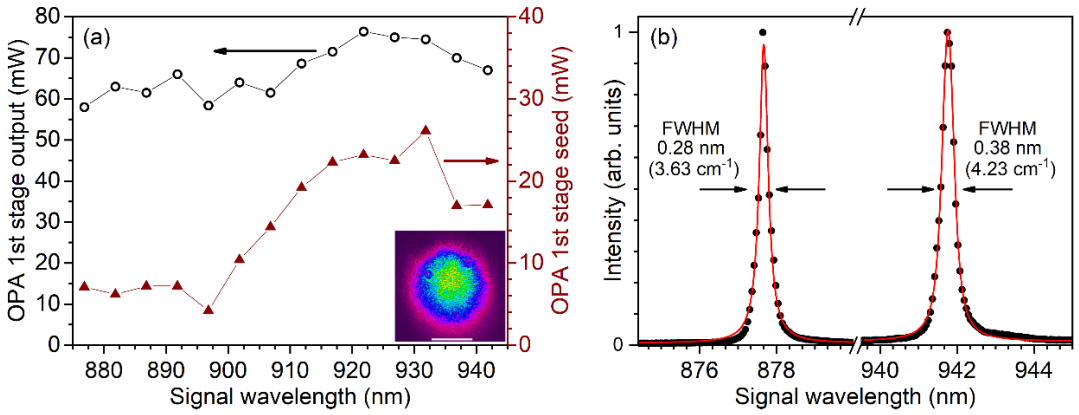

Figure 2-2. The first stage optical parametric amplification (OPA) power and spectrum. (a) OPA signal and seed output powers at various wavelength. Inset shows the signal beam profile after the collimating lens, the scalebar is 1 mm. (b) OPA signal spectra at 877 nm and 942 nm. Dots – experiment, solid line – Voigt fit.

The signal wave from the first OPA stage is filtered from the residual pump and idler waves and seeds the second OPA crystal (type-I β-barium borate, l = 4 mm, θ = 22°). The crystal is pumped by 1.7 W of 532 nm radiation. The 532 nm pulse is appropriately delayed maximizing the gain at the second stage.

Thus, after optimizing the spatial and temporal overlaps of the seed and pump pulses, we achieve 0.5 W in combined signal and idler waves after the second OPA stage (Figure 2-3(a)), and more than 320 mW in the signal beam. The beam profile of the signal beam after amplification remains close to Gaussian as well (Figure 2-3(a), inset), which is important for further efficient generation of UV harmonics. Figure 2-3 (b) shows the idler pulse signal dependence on the time delay of the pump (532 nm) pulse at the second OPA stage. Since the second amplification stage is seeded with only the signal wave, we can use this measurement as the cross correlation to determine the generated pulse duration. The FWHM of the trace is 9.5 ps and assuming the Gaussian pulse waveform, we estimate the pulse duration to be ≈6.7ps, which is slightly less than the fundamental 1064 nm pulse (10 ps).

The signal beam, after collimating and filtering from the residual pump and idler waves, is loosely focused by 20 cm plano-convex lens into BiBO crystal (BiB_3O_6, l = 4 mm, $\varphi = 90°$, $\theta = 162°$). The BiBO crystal has higher effective nonlinear coefficient than BBO and better figure of merit for blue light generation, with comparable damage threshold [58]. Thus, it becomes a great choice for the SHG to convert near-IR signal wave into the visible radiation. In this configuration we achieve 132 mW at 471 nm, i.e. reaching 50% power conversion efficiency for the signal wave into the second harmonic.

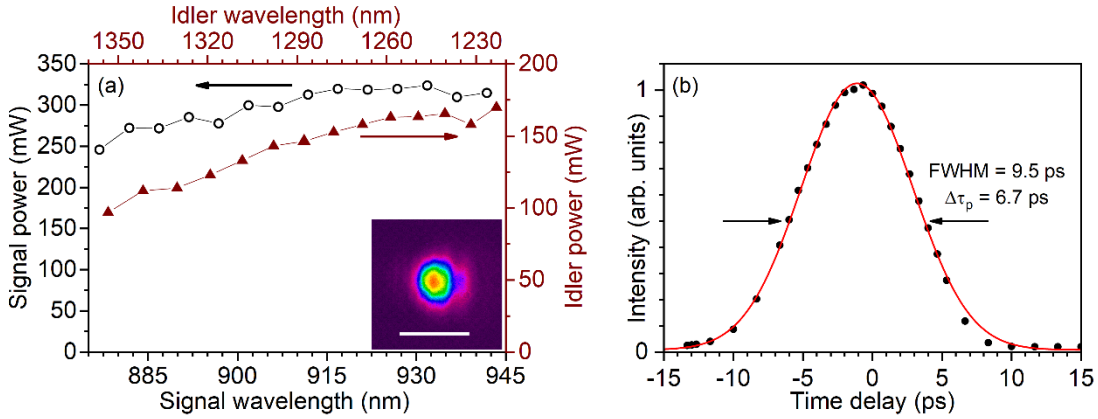

Figure 2-3. The second stage optical parametric amplification (OPA) power and cross correlation. (a) OPA signal and idler output powers at various wavelength. Inset shows the signal beam profile after the collimating lens, the scalebar is 1 mm. (b) The cross correlation of the signal pulse with the 532 nm pump at the second OPA stage. Dots: experiment; solid line: Gaussian fit.

After filtering from the OPA signal beam the blue SHG beam is focused into another type-I BBO crystal (l = 5mm, $\theta = 58^{\circ}$; Crystech, Inc.), where ultraviolet FH of the OPA signal is generated (Figure 2-4). After the crystal, the beams are collimated with the CaF_2 lens and the UV beam is spatially separated from the fundamental with a prism. We achieve more than 36 mW in the UV beam, corresponding to 0.36 μJ energy per pulse and more than 50 kW of peak power (Figure 2-4 (a)). At the same time, we reach maximum 12% power conversion efficiency of the near-infrared OPA signal wave into the UV radiation. The power fluctuations are below 5% and are mainly limited by the stability of CW seed laser on the first of OPA stage. As we avoid tight focusing into the crystals, the beam shape of the generated UV radiation remains close to Gaussian (Figure 2-4(a), inset). The measured bandwidth of the UV pulse is 0.054 nm (9.7 cm^{-1}), which is limited by the spectral resolution of the monochromator (iHR320, 2400 l/mm grating; Horiba, Inc.). Since we used a narrowband CW seed on the first OPA stage and avoided self-generation

of signal and idler waves on both OPA stages, it is expected that the actual UV pulse bandwidth is close to the transform limited and on the order of a typical linewidth of Raman lines. We demonstrate the suitability of our laser source for the high-resolution UV Raman spectroscopy by taking Raman spectra of the ambient air (Figure 2-5).

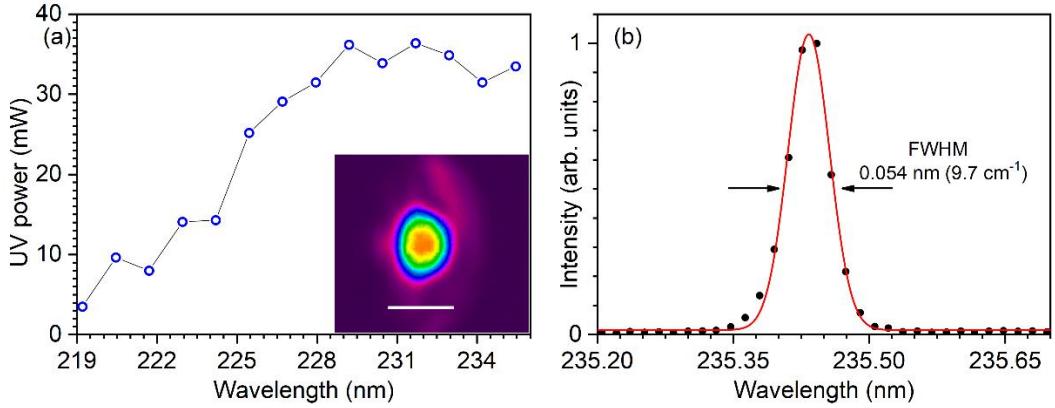

Figure 2-4. Ultraviolet (UV) laser power and spectrum. (a) UV power at various wavelength. The inset shows the beam profile of the UV beam, measured after the collimating lens, the scalebar is 1 mm. (b) UV spectrum at 235.4 nm. Dots – experiment, solid line – Gaussian fit.

We use a 50/50 beamsplitter to collect backscattering Raman signal after focusing with CaF_2 lens (f = 10 cm) the 10 mW of UV radiation in air. After filtering with the Raman edge filter (LP02-244RS-25, Semrock, Inc.), the signal is focused on the slit of the monochromator (iHR320; Horiba, Inc.), which has a liquid nitrogen cooled CCD attached (1LS-2048x512-BU UV enhanced CCD; Horiba, Inc.). Although the filter was initially designed to best perform at 244 nm radiation of Ar-ion laser, after tilting it, we were able to record Raman spectrum as low as 1000 cm^{-1} with the 235.45 nm excitation wavelength and 120 seconds acquisition time (Fig. 5). The collected Raman spectrum clearly demonstrates characteristic lines of O_2, N_2 and water vapor presented in the laboratory air.

The inset shows main rotational and vibrational UV Raman spectrum of oxygen molecule [59]. As one can see, both the main vibrational as well as rotational transitions can be resolved, which indicates the narrowband excitation of rotational and vibrational transitions with the DUV pulse.

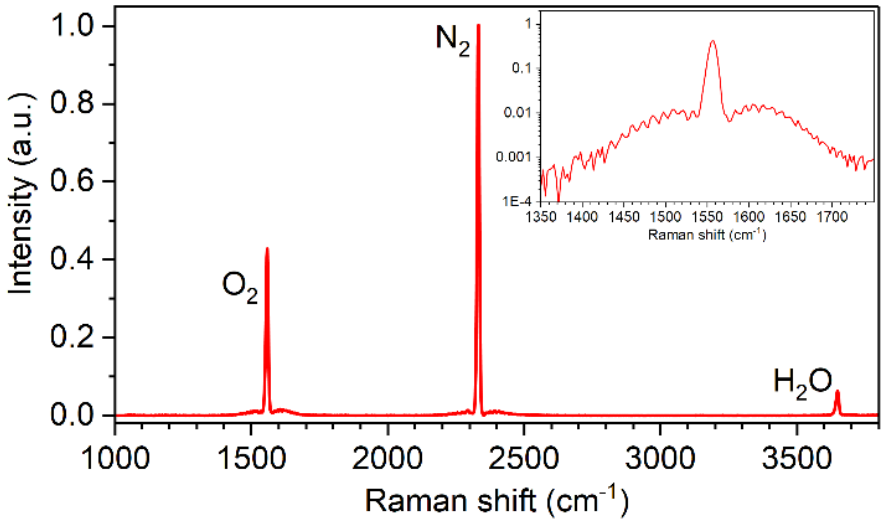

Figure 2-5. UV Raman spectrum of air. Excitation wavelength is 235.45 nm, integration time is 120 seconds. Inset shows enlarged 1350 – 1750 cm^{-1} spectral region.

In summary, we demonstrated an experimental setup for the generation of deep UV picosecond laser radiation tunable from 219 to 236 nm. The system is based on the two-stage optical parametric amplification in LBO and BBO crystals and pumped by a second harmonic of 6-10 ps 1064 nm Nd:YAG laser. The choice of the pump laser is not critical, and any short-pulse fiber laser can be used, since the output bandwidth is defined by the pulse duration of the pump rather than its bandwidth. We use a narrowband CW laser tunable between 877 and 930 nm as the seed on the first OPA stage with low gain to avoid self-generation. The second OPA stage is followed by a fourth harmonic generation using a combination of BiBO and BBO crystals. As a result, we achieve 36 mW of tunable deep

UV radiation, corresponding to 0.36 μJ pulse energy at 100 kHz repetition rate, with the beam profile close to Gaussian. We reach the conversion efficiency of near IR radiation into the DUV pulse up to 12%, while the tunability and stability of our laser system is mainly limited by the CW laser source. Finally, we demonstrate the applicability of our laser source for UV Raman spectroscopy by taking Raman spectrum of air at 235.45 nm excitation wavelength. The developed laser system can be used for material characterization, biomedical spectroscopy and remote gas sensing.

2.2. DUV Raman spectroscopy and identification of chemicals with the tunable picosecond laser system

In this section we demonstrate the applicability of the abovementioned laser system [36] for the DUV Raman spectroscopy. Therefore, the experimental setup is similar to the one described in the previous section. The DUV pulse was focused into the test cell containing the sample with a CaF_2 lens (f/ = 0.25). The backward Raman scattering signal after filtering with the edge filter (LP02-244RS-25, Semrock, Inc.) was focused on the slit of the monochromator (iHR320; Horiba, Inc.), which had a liquid nitrogen cooled CCD attached (1LS-2048x512-BU UV enhanced CCD; Horiba, Inc.). The spectral resolution of the setup is mainly limited by the monochromator to the 9 cm^{-1}. Although, the edge filter was designed to work with 244 nm Ar-ion laser line, we were able to retrieve Raman spectra above ~700 cm^{-1} after carefully tilting it. Unfortunately, it also forced us to use the high wavelength tuning range of our laser system, i.e. perform measurements with laser wavelength fixed at 235.45 nm, except the case when we compared excitation at different wavelengths. The reference spectrum of the cell was subtracted from all obtained spectra. All spectra were collected with 10 s integration time if different is not noted.

2.2.1. Results

2.2.1.1. Diet and regular Coke.

One of the challenges of Raman spectroscopy using visible light is obtaining spectra of highly absorbing and fluorescent substances, for example Coca Cola [60] (CC). As it is well known, the CC is a black opaque substance, i.e. strongly absorbs visible light. In

addition to that, it is highly fluorescent [61] which impedes Raman spectroscopy using visible light and making such a simple task, as, for example, distinguishing diet CC with regular one quite challenging. By employing DUV excitation for Raman spectroscopy we overcome these difficulties. Figure 2-6 shows DUV Raman spectra for dietary and regular CC samples. Both spectra were normalized and background spectrum from the glass cell and air was subtracted. One can see that the spectra have similar intensities of O-H stretching signal above 3000 cm^{-1}. However, as regular CC contains sucrose, there is a strong peak at 2950 cm^{-1} attributed to C-H stretching. At the same time, the narrow peak at 1605 cm^{-1}, indicating the presence of the sweetener in diet CC, is not presented in the spectrum of regular CC. Hence, DUV Raman spectroscopy here allows to distinguish two highly absorptive and fluorescent substances with ease even without deeply involved analysis of the Raman spectrum.

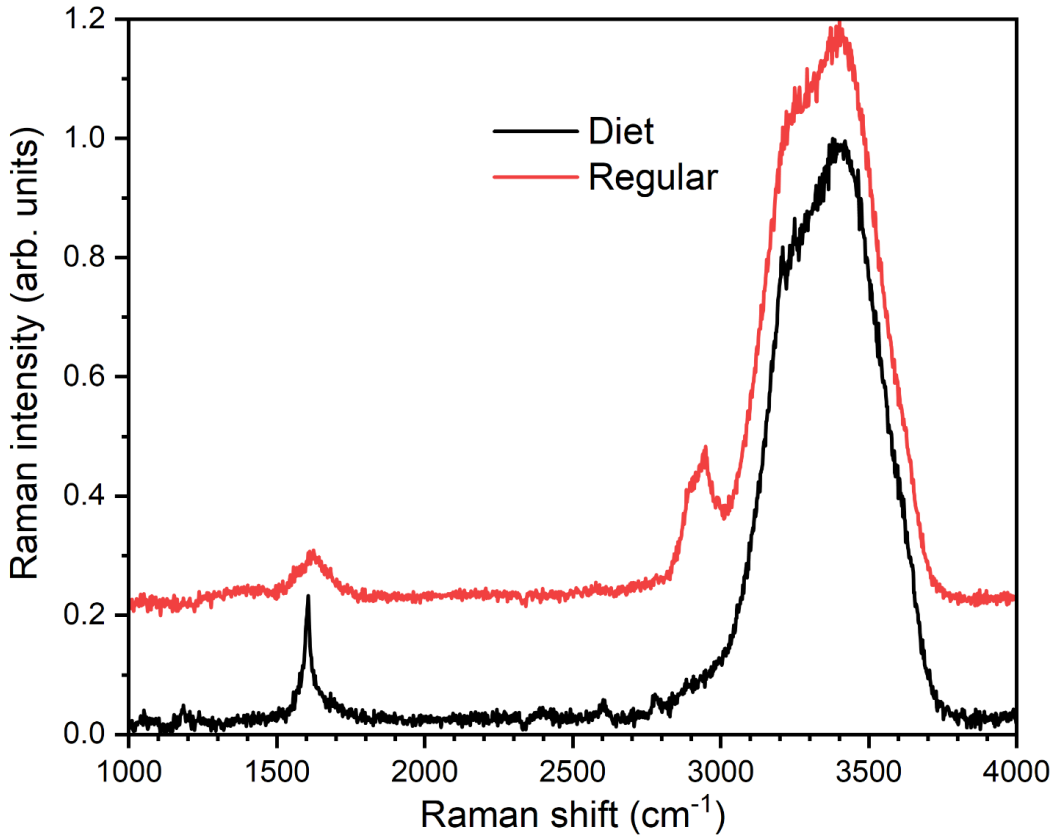

Figure 2-6. Normalized Raman spectra of dietary (diet, black line) and regular (regular, red line) Coca Cola. Acquisition time is 5 seconds. The regular Coca Cola spectrum is offset for clarity.

2.2.1.2. Raman overtones in nitrates and tungstates.

As the excitation photon energy approaches the energy level of electronic states in molecules, the vibronic (i.e. involving both electronic and vibrational dipole moments) transitions can be excited. In a typical Raman spectrum this case can be seen when multiple overtones of the strongest vibrational transitions molecule appear [62]. Hence, the DUV Raman spectrum in addition to vibrational transitions contains information about electronic structure of the molecule of interest. Here we report on observing multiple

overtones for different samples, including barium tungstate ($BaWO_4$), as well as ammonium nitrate (NH_4NO_3).

Barium tungstate has three distinct and narrow Raman lines in the spectral region 650 – 1000 cm^{-1}, where the strongest at ~925 cm^{-1} correspond to internal symmetric vibration of WO_4 group [63]. The Raman cross-section of 925 cm^{-1} mode is almost as high as in diamond [64], making it a good candidate for observing Raman overtones. Figure 2-7 shows Raman spectrum of barium tungstate powder and its water suspension. To prevent an optical damage of the sample, the laser power was limited to 1 mW. As one can see, in both observed spectra the second (at 1849 and 1851 cm^{-1}) and third (2772 and 2770 cm^{-1}) overtones of the main strongest vibration are present. In this case the suspension measurement allows longer interaction length, so the signal to noise ratio is larger as the laser beam is quickly scattered in $BaWO_4$ powder.

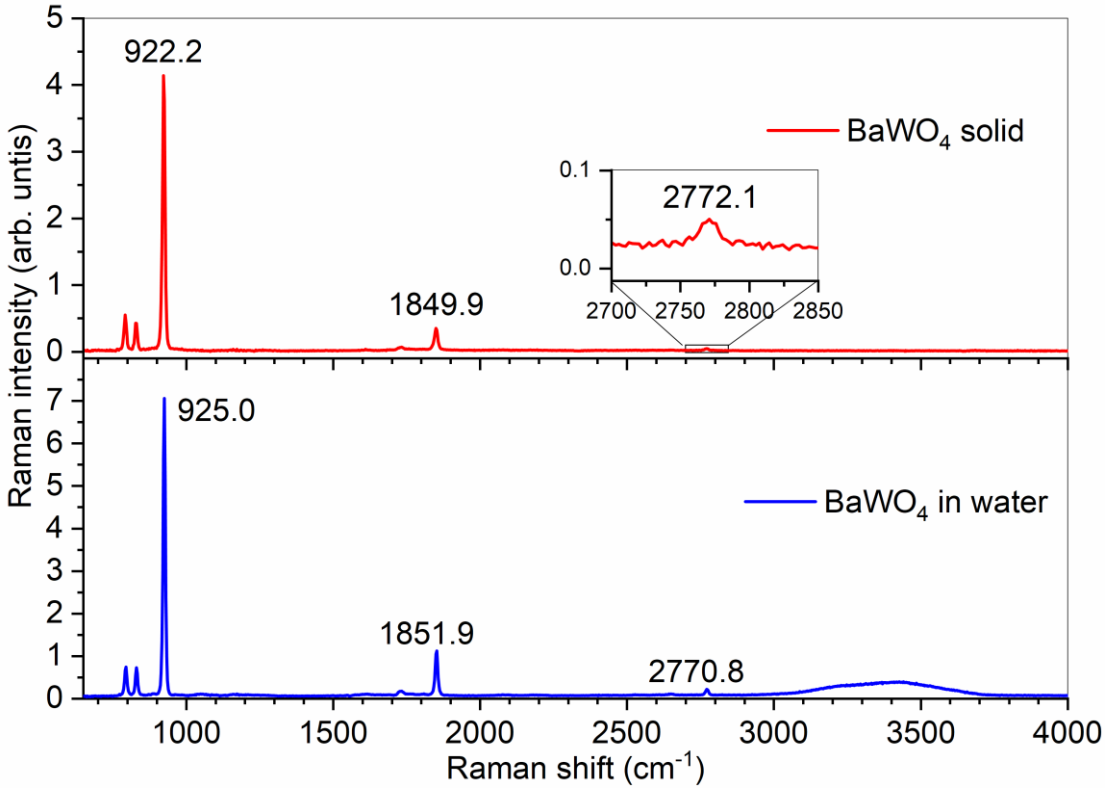

Figure 2-7. Barium tungstate Raman spectrum. Top: barium tungstate powder, bottom: a 7M water suspension. Broad feature around 3500 cm^{-1} is the solvent band.

Figure 2-8 shows Raman spectrum of ammonium nitrate both as crystalline powder at the room temperature and dissolved in water (1.2 mg/mL solution). The water solution provides longer interaction length and therefore better signal-to-noise ratio. One can see that both spectra contain similar structures and closely follow each other. The most intense line in the spectrum at 1044 cm^{-1} (ν_1) is the NO_3^- ion totally symmetric vibration [65,66]. The 1292, 1416 and 1461 cm^{-1} peaks in the solid sample spectrum can be assigned to the asymmetric NO_3^- stretching [67] (ν_3). However, in solution this vibrational mode becomes coupled to the water motion, as a result it appears as a broad feature around ~1350 cm^{-1} in Raman spectrum. The 1662 (1661 in water) cm^{-1} line is the second overtone

of out-of-plane deformation ($2\nu_2$). Other overtones appear at Raman shifts above 2000 cm^{-1}: 2092 ($2\nu_1$), 2400-2600 cm^{-1} ($\nu_1 + \nu_3$), 2696 (2699 in solution) cm^{-1} ($\nu_1 + 2\nu_2$), 2942 cm^{-1} ($2\nu_2 + \nu_3$), 3119 (3129 in solution) cm^{-1} ($3\nu_1$) and small peaks above 3300 cm^{-1} ($2\nu_1 + 2\nu_2$ as well as $\nu_1 + 2\nu_3$).

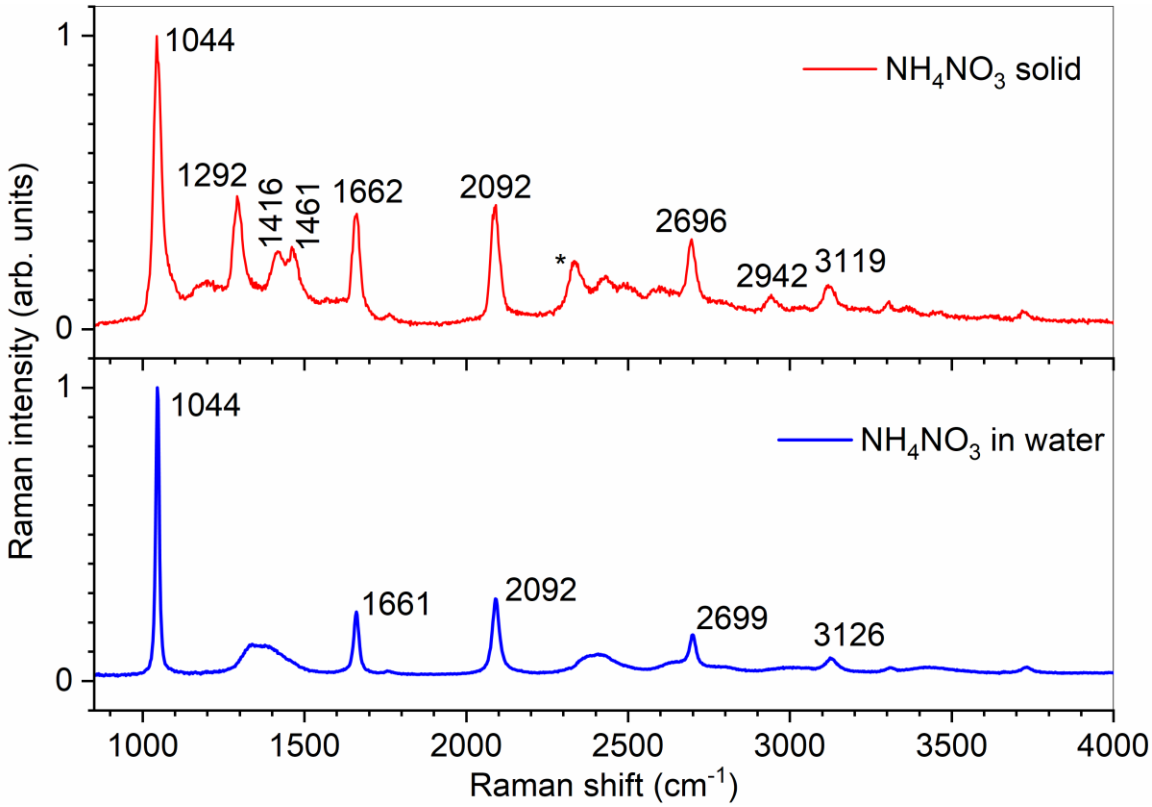

Figure 2-8. Ammonium nitrate Raman spectra. Top ammonia solid powder (acquisition time 30 s), bottom: 1.2 mg/mL solution in water (acquisition time 10 s). The peak marked by asterisk correspond to N_2 presented in the atmosphere.

Figure 2-9. shows Raman spectrum of powdered pyrene ($C_{16}H_{10}$). It is one of the most frequently used fluorescent probes, especially for proteins and biological membranes [68], so determination of its Raman spectrum is quite challenging [69]. The obtained Raman spectrum with its overtones has a good correlation with the previously reported

results [62]. The strongest Raman peak at ~1630 cm^{-1} corresponds to A_g symmetry vibration. Essentially, all other observed peaks above 1630 cm^{-1} are overtones and combinations bands.

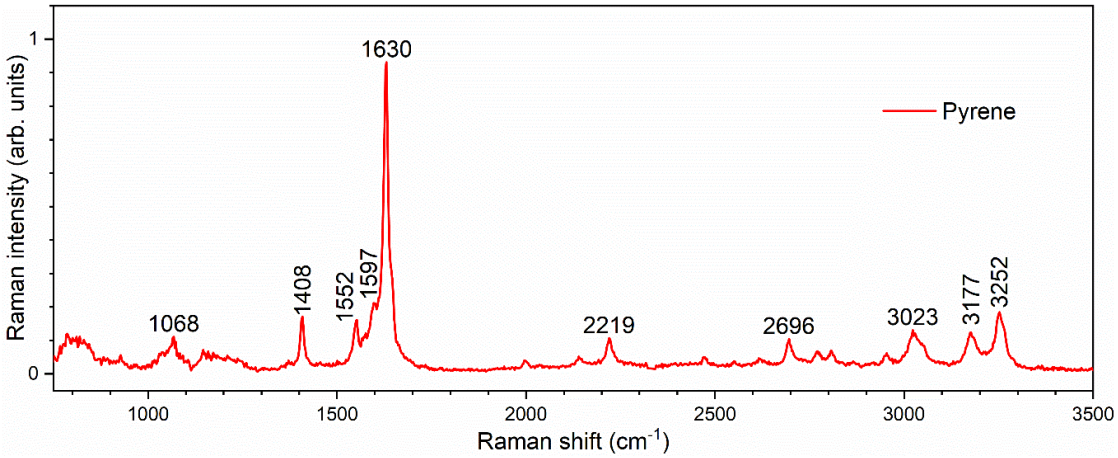

Figure 2-9. Raman spectrum of pyrene. Acquisition time 30 s, laser power on the sample is 2 mW.

2.2.1.3. Gasolines

Figure 2-10 shows Raman spectra of 4 different gasolines and the diesel fuel obtained from a local gas station. Different gasolines brands and types typically have slightly different chemical composition and can contain different concentrations of additives, such as ethanol. Although all of them contain the same peaks, the difference is clearly seen. In addition to the strong broadband features at 1387 cm^{-1} and 1630 cm^{-1}, the diesel fuel lacks the sharp low frequency peaks below 1250 cm^{-1}. Hence, it can be clearly distinguished from the gasolines. The gasolines, itself, contain different amount of ethanol, which has its characteristic three-peaks structure at 2800-3000 cm^{-1}. Interestingly, the lowest grade

gasoline (Shell 87) contains higher amount of ethanol than the gasoline one grade higher (Shell 89).

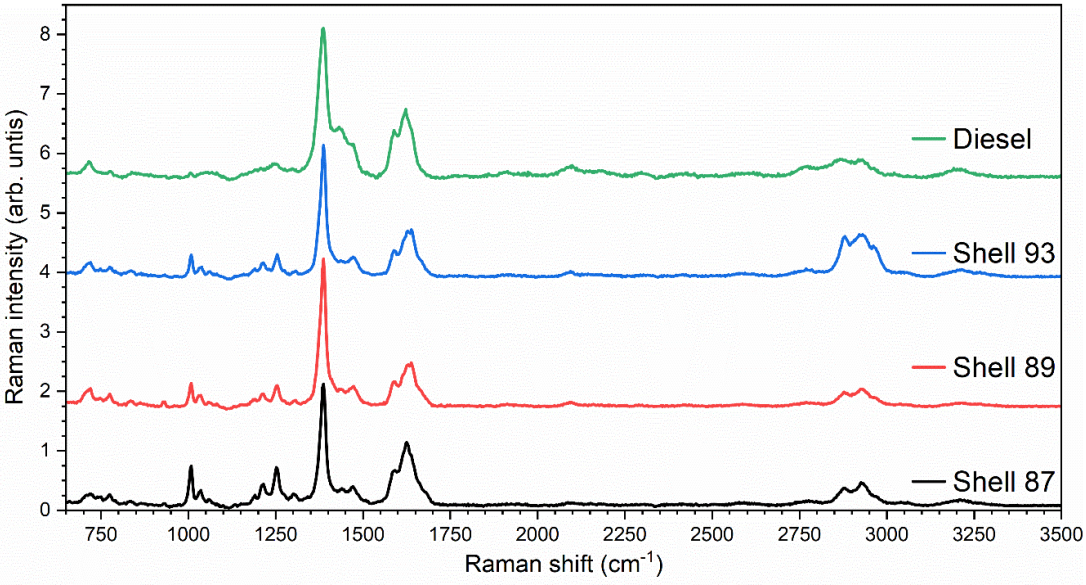

Figure 2-10. UV Raman spectra of different gasolines. The acquisition time is 15 seconds. The same baseline from all spectra was removed.

2.2.1.4. Air

Obtaining Raman spectrum of a gas sample brings another challenge for the researcher. For instance, typically the Raman scattering in gases is much weaker than in liquids and solids, hence, obtaining a reasonable signal-to-noise ratio requires longer acquisition times. Moreover, a complex laser system, especially the one based on parametric amplification and frequency conversions, can drift during the experimental measurements both in terms of power and spectrum. Hence, the instability of the laser system can decrease the spectral resolution of Raman spectroscopy. As we can see from Raman spectrum of air (Figure 2-11) our laser system remains stable for the sufficient time to obtain Raman spectrum (acquisition time 120 s). The top graph shows two

enlarged spectral regions: oxygen (1555 $cm^{-1)}$ and nitrogen (2331 cm^{-1}) molecule vibrations. Clearly, the laser wavelength does not drift significantly, as multiple rotational-vibrational lines can be resolved for both molecules. In additions to the Q-branch ($\Delta J = 0$) transitions, O- ($\Delta J = -2$) and S- ($\Delta J = +2$) branches are clearly resolved in the spectra of both oxygen and nitrogen. The lines correspond to the previously reported [59,70,71], although due to the limited resolution of the spectrograph some rovibrational transitions cannot be resolved.

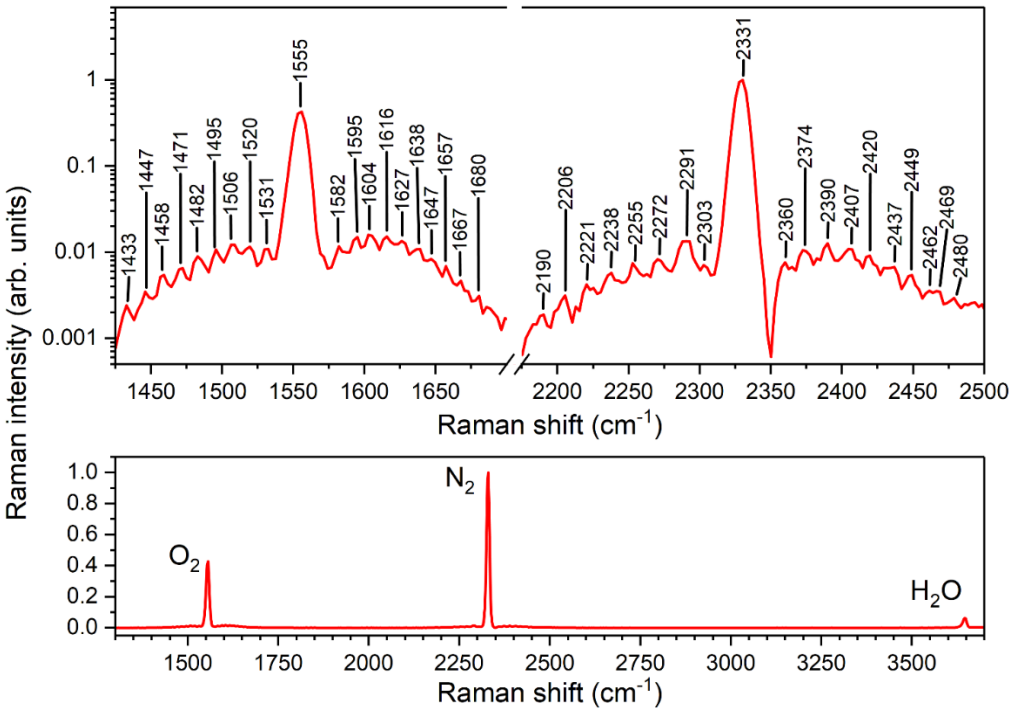

Figure 2-11. Raman spectrum of air. Top: log scale of the 1400-1700 and 2150-2500 cm^{-1} spectral regions, showing rovibrational spectra of oxygen and nitrogen molecules, correspondingly. Bottom: UV Raman spectrum, acquisition time 120 sec.

2.2.1.5. UV enhancement of Raman scattering in gasolines

Figure 2-12 shows Raman spectra of Shell 87 gasoline obtained at two laser wavelengths. The obtained Raman signal (in CCD counts) allows us to compare the intensities at different excitation frequencies, while keeping the power on the sample constant (7 mW). The plot shows the raw data from the CCD detector; hence we can directly compare the intensity of Raman signal. We see about 30% increase of the signal above 1250 cm^{-1} during the blueshift of excitation wavelength. As expected with increasing the photon energy the Raman scattering cross sections increase as well. At the same time, as the overall shape of the Raman spectrum did not change significantly, we can conclude that the photon energy is still well below the energies of the lower electronic levels and the excitation is off any resonances.

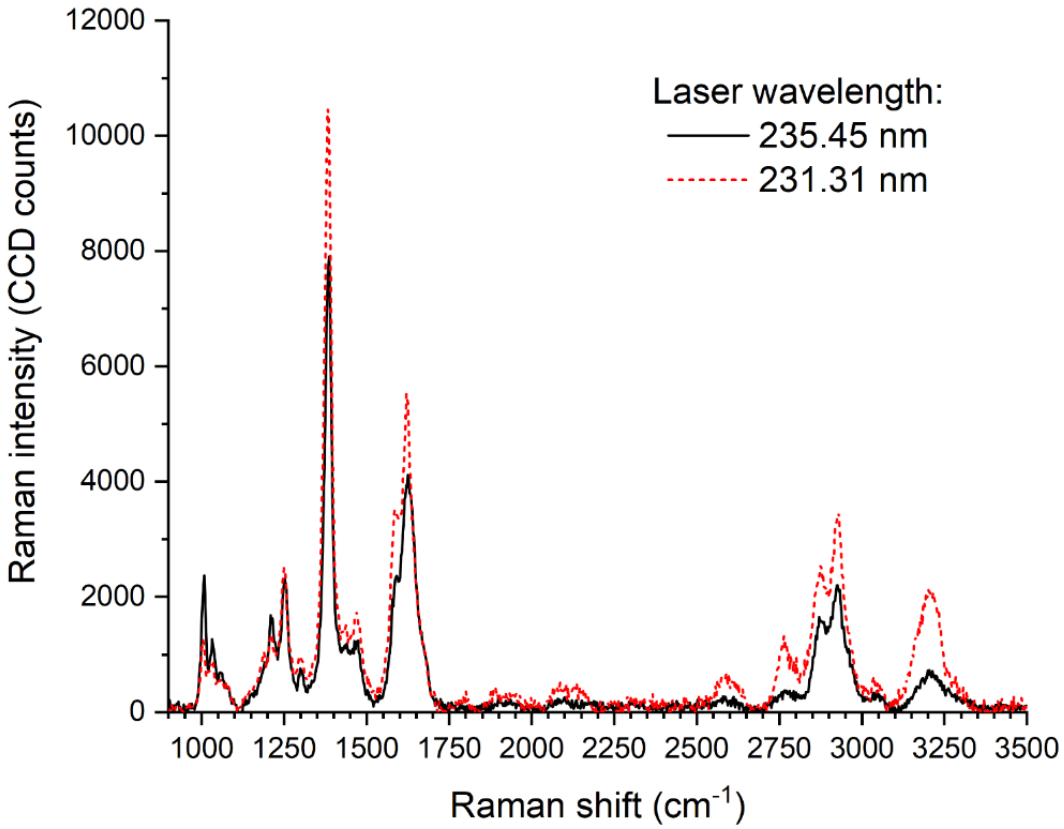

Figure 2-12. Gasoline Raman spectra taken with two different excitation wavelengths. The plot shows raw CCD signal with the baseline removed. The integration time in both cases is 5 seconds.

2.3. Conclusion

Clearly, the DUV and resonance Raman spectroscopy have multiple advantages over spontaneous Raman spectroscopy with visible and NIR lasers. DUV Raman spectroscopy demonstrates higher chemical sensitivity and selectivity, as well as drastically increased scattering signals, but requires a complex laser system. As it was shown, one can exploit nonlinear optics phenomena, such as optical parametric amplification and harmonics generation to design and built a tunable DUV laser source. The demonstrated system

possesses all the properties one can require from the laser source: it is reliable, tunable, narrowband and provides sufficient power to perform DUV Raman spectroscopy.

Although the DUV Raman spectroscopy exploits the resonant enhancement and benefits from the increased Raman scattering cross sections, it remains a technique based on the spontaneous Raman scattering phenomenon. In this sense, it is still incoherent light scattering scaling linear with the concentration of scatters. As we will demonstrate in the following chapter, the scattering efficiency can be significantly improved by introducing a molecular coherence into the system. The experiments on coherent anti-Stokes Raman scattering (CARS) spectroscopy will show that CARS provides much better chemical sensitivity and selectivity than spontaneous Raman scattering, as well as additional spectroscopic information, such as vibrational dephasing rates.

3. COLLINEAR FAST CARS FOR CHEMICAL MAPPING OF GASES*

3.1. Introduction

Both spontaneous and coherent Raman scattering effects have been employed in spectroscopic systems applied to the trace detection and identification of chemicals [40,72] and as a method to measure concentrations of various components in gases [73–75], liquids and solids [76,77]. In spontaneous Raman scattering, the signal is directly proportional to the number of molecules interacting with a single beam of input light. By contrast, coherent anti-Stokes Raman scattering (CARS) is a nonlinear process where the molecules are first put into a state of coherent oscillations, resulting in an increased probability for a probe pulse to scatter and produce Stokes or anti-Stokes shifted photons [78]. Therefore, CARS-based techniques possess an inherent ability to offer higher signal strength and faster collection speed compared to approaches based on spontaneous Raman scattering [42].

With the development of ultrashort pulsed laser sources, CARS imaging opened the possibility to study the dynamics of such rapidly changing systems as gas flows [79]. The great flexibility of the CARS technique makes it a popular instrument for performing thermometry measurements for various gases: nitrogen and oxygen [80–82], carbon dioxide [83], as well as methane and hydrogen [84]. CARS techniques allows concentration and temperature measurements in harsh environments and at high

*Part of this chapter is reprinted with permission from "Collinear FAST CARS for Chemical Mapping of Gases" by A. D. Shutov, D. Pestov, N. Altangerel, Z. Yi, X. Wang, A. V. Sokolov, and M. O. Scully, Applied Sciences 7, 705 (2017). Copyright [2017] by Creative Commons Attribution 4.0 International License.

temperature during the combustion process [85,86]. Moreover, one-dimensional [87,88], as well as two-dimensional [89] single-shot thermometry and mapping of reactants and products in gas flows can be performed by different experimental approaches.

The CARS signal is expected to scale proportionally to the second power of the concentration of target molecules in a sample. However, Raman linewidth changes [90], signal re-absorption [77], as well as nonresonant contribution from background molecules [91,92] may alter the dependence of the CARS signal on the concentration, making it difficult to correlate the signal strength with the distribution of those molecules. Gas flows, in particular, are multi-component systems, usually containing a large number of background molecules contributing to the CARS signal background. Some of the aforementioned problems, i.e., Raman line broadening, can be resolved by taking into account line broadening coefficients [93] as well as dephasing rates for the gas species [94].

Here we show that the femtosecond adaptive spectroscopic technique (FAST) for CARS [95] maintains the proper dependence of the CARS signal on concentration and thereby assures a direct correspondence between CARS intensity image and molecular distribution. FAST CARS is a combination of methods aimed at optimizing the CARS signal and suppress the noise background. In the ‘hybrid’ implementation of FAST CARS, we use two ultrashort pump-Stokes excitation pulses to prepare a coherent oscillation of molecules (Figure 3-1(a)), in combination with a narrowband delayed probe pulse to provide near-perfect non-resonant four-wave mixing background suppression [96,97]. Recently, in addition to gas-phase studies, this scheme was successfully used for

microspectroscopy [98,99], and for spectroscopic molecular sensing aided by plasmonic nanostructures [100–102].

In this work, we experimentally demonstrate that the hybrid CARS signal obtained for molecular oxygen scales as the square of the number of molecules in two scenarios: constant concentration of oxygen (the total pressure varies) and constant pressure (the oxygen concentration varies). We should note that the determination of a molecular concentration based on the quadratic dependence of the CARS signal intensity on the number of molecules has been performed before using ns-CARS [103] and hybrid CARS [104] techniques. However, here we focus on demonstrating that this dependence can be maintained at different experimental conditions without prior calibration of specific gases composition or concentration. In addition, we provide a simple yet clear illustration of how the hybrid CARS technique can be exploited for imaging and sensing of a gas flow escaping from a nozzle by performing multi-shot measurements along with a raster-scanning an area in a collinear configuration. In the future, the same ideas can be applied to remote detection and sensing of trace amounts of gases [105].

3.2. Experimental Setup

Figure 3-1 shows the experimental setup for our oxygen concentration measurements. As a laser source, we employ a Ti:sapphire regenerative amplifier (1 kHz repetition rate, 0.73 mJ/pulse, Legend, Coherent, Santa Clara, CA, USA) with two equally pumped optical parametric amplifiers (OPAs: OPerA-VIS/UV and OPerA-SFG/UV Coherent, Santa Clara, CA, USA). The outputs of the two OPAs are used as the pump and Stokes pulses (<130 fs). A small fraction of the amplifier output passes through a homemade

pulse shaper with an adjustable slit and is used as a probe beam. The adjustable slit width allows us to select a narrow spectral band ($\Delta\nu \approx 11\ cm^{-1}$) at 806 nm, which corresponds to about 2 ps pulse duration. The pump and the probe beams pass through delay stages (DS1,2), so that the probe pulse is time delayed with respect to the pump and Stokes pulses. Choosing time delay for the probe pulse along with its pulse shaping, provide a clear CARS signal with suppressed non-resonant background from the four-wave mixing signal generated by the three beams.

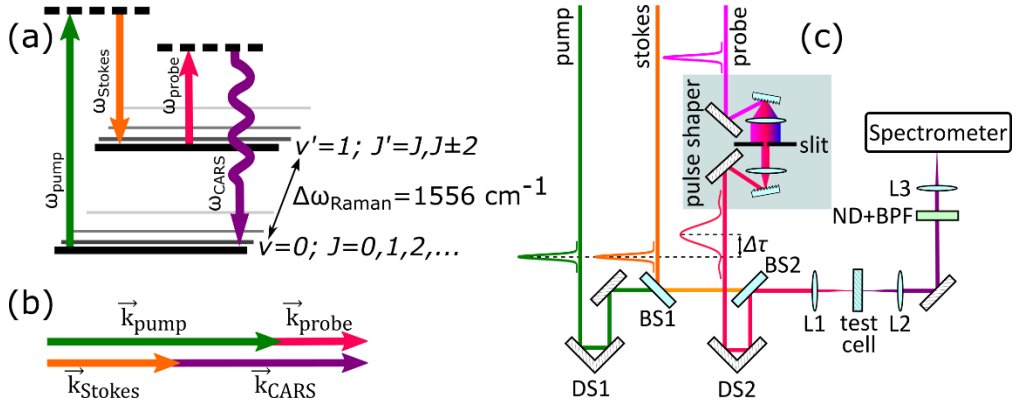

Figure 3-1. (a) CARS (coherent anti-stokes Raman scattering) level diagram. CARS signal is generated from the probe pulse scattering off the molecular vibration, coherently prepared by the pump (ω_{pump}) and Stokes (ω_{Stokes}) pulses, which are resonant with the Raman frequency of the molecule ($\Delta\omega_{Raman}$). v, J, v', J'—initial and final vibrational and rotational states correspondingly; (b) Phase matching CARS scheme for collinear beams configuration; (c) Experimental setup. DS1,2—delay stages. BS1,2—beamsplitters, L1–3—lenses (f = 100 mm), ND+BPF—set of neutral density and bandpass filters.

The collinear geometry configuration for all beams aids to simplify epy optical alignment and signal collection, with automatically satisfied phase-matching conditions in gases (Figure 3-1(b)). The wavelength (FWHM bandwidth) of the pump, Stokes pulses and probe beams are set to 556nm (13.6 nm), 610 nm (14.1 nm) and 806 nm (0.7 nm), with 3.1 μJ, 2.6 μJ and 0.9 μJ pulse energies respectively. When the probe delay is varied,

the full hybrid CARS spectrogram can be observed (for example, see Results section in Chapter 4). In present experiments, the probe delay with respect to the pump/Stokes pulses is fixed at the optimum value of 2.1 ps. The beams are combined by two dichroic beamsplitters (BS1,2) and focused by a convex lens L1 (f = 100 mm) in the homemade gas cell (Borosilicate glass, 1 mm thickness, 25.2 cm^3, 8 cm long) filled with N_2 and air gas mixture. The three beams and the generated CARS signal are collimated by another lens (L2, f = 100 mm) and filtered by a set of neutral density (FW2AND Thorlabs, Newton, NJ, USA) and bandpass filters (FF01-732/68 Semrock, Rochester, NY, USA) (ND+BPF). After passing through the filters, the beam is focused by the lens L3 (f = 100 mm) on the entrance slit of the spectrometer: the spectrograph (Chromex Spectrograph 250is, Albuquerque, NM, USA), which has a liquid-nitrogen-cooled CCD camera (CCD: uncoated Spec-10:400B, Princeton Instruments, Trenton, NJ, USA) attached.

The spectral resolution of the experimental setup is limited by two factors: the spectrometer resolution and the probe pulse spectral width. The spectrometer resolution is determined by its slit size and was set to 0.12 cm^{-1} for all measurements, thus the total spectral resolution during experiments was mainly limited by the width of the probe pulse (≈11 cm^{-1}). The probe pulse duration (≈2 ps) constrains the temporal resolution. The spatial resolution in transverse to the propagation direction of the beams is mainly limited by a beam focal spot diameter (estimated at ≈20 μm). However, the axial spatial resolution, i.e., in the direction of the beams propagation, can be potentially limited by the fact that the CARS signal is generated in the region up to 6 times larger than the Rayleigh range (≈0.4 mm for our beams configuration) [78] in the collinear beams configuration. This

fact does not limit the concentration dependence measurements since the gas cell length is significantly larger than the estimated length of this region (2.4 mm).

3.3. Results and Discussion

In the first set of experiments we study the CARS signal of O_2 molecules by filling the gas cell with air at different pressures. As the first step towards optimizing the beam alignment and time delays for pump/probe pulses, we collect the CARS spectrum showing rotational-vibrational structure of oxygen molecule (Figure 3-2), where several peaks can be clearly distinguished. The signal was collected for 2.2 s at atmospheric pressure at 1 kHz. The main peak of the spectrum (1555.6 cm^{-1}) corresponds to the Q-branch ($\Delta J = 0$) vibrational transition from the vibrational ground level of the oxygen molecule. Smaller peaks on the left and on the right to the Q-branch transition represent O- ($\Delta J = -2$) and S- ($\Delta J = +2$) transitions correspondingly [71].

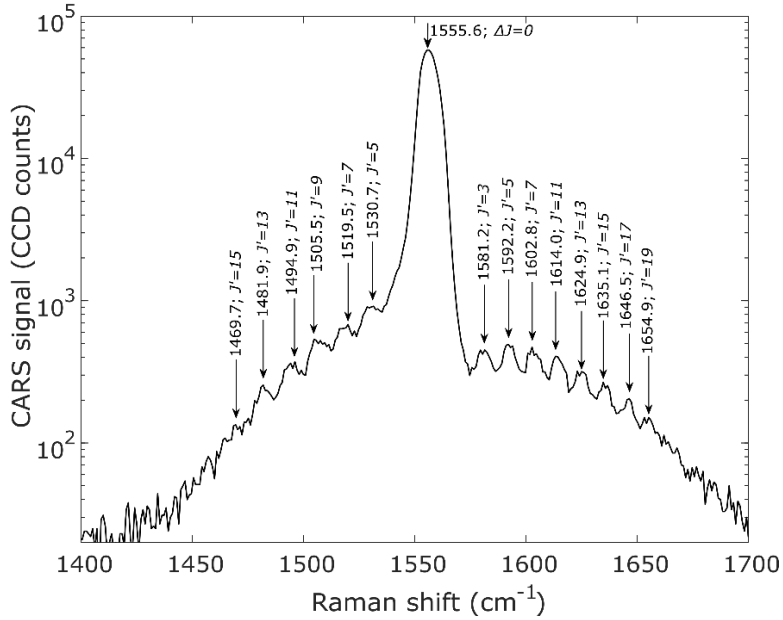

Figure 3-2. CARS spectrum of molecular oxygen in ambient air. Arrows mark the locations with maximum intensities, and corresponding wavenumbers and final quantum rotational numbers are given.

Thereafter, we use the maximum CCD count value from the region of Raman shift 1556 ± 1 cm^{-1}, i.e., the intensity of the Q-branch vibrational line to examine the dependence of the CARS signal on gas concentration and pressure. Before calculating the maximum intensity, the zero-pressure background signal was subtracted from the data. We find using the maximum intensity to be more convenient and yet sufficiently precise for studying the dependence of the CARS signal on molecular concentration, when the absolute concentration of gas species is irrelevant. However, it is worth mentioning, that the fitting curves parameters for integrated intensity data points differ from the peak fittings by less than one standard deviation (4.6%).

During these measurements laser power fluctuations at 1 kHz repetition rate were below 0.5% and the signal was integrated for 5.2 s. The long integration time aids in significantly reducing the signal intensity fluctuations but forces us to use at least ND = 3.0 filter at ambient conditions in order to avoid saturation of the CCD detector.

First, the cell is filled with a gas mixture of ambient air and pure nitrogen (Figure 3-3, solid circles). We assume the oxygen presence in air to be 21% and vary the partial pressures of air and nitrogen while keeping the total pressure in the cell constant. These measurements allow us to study the dependence of CARS signal on the concentration of O_2 with different amounts of background molecules (N_2). In this case, the CARS signal scales as a square of the relative oxygen concentration.

Next, we fill the cell with ambient air at various pressures, keeping the gas composition and ratio of oxygen molecules to background molecules constant. We control the total pressure inside the gas cell by a ball valve and perform measurements for the

range from 0.01 bar to 1.07 bar. The experimental data with the fit curve is shown in Figure 3-3 (hollow diamonds), where the signal is proportional to the square of the gas pressure. Hence, we conclude that in both cases of the constant gas mixture at different pressures and varied gas compositions at constant pressure, the CARS signal is proportional to the square of the number of O_2 molecules.

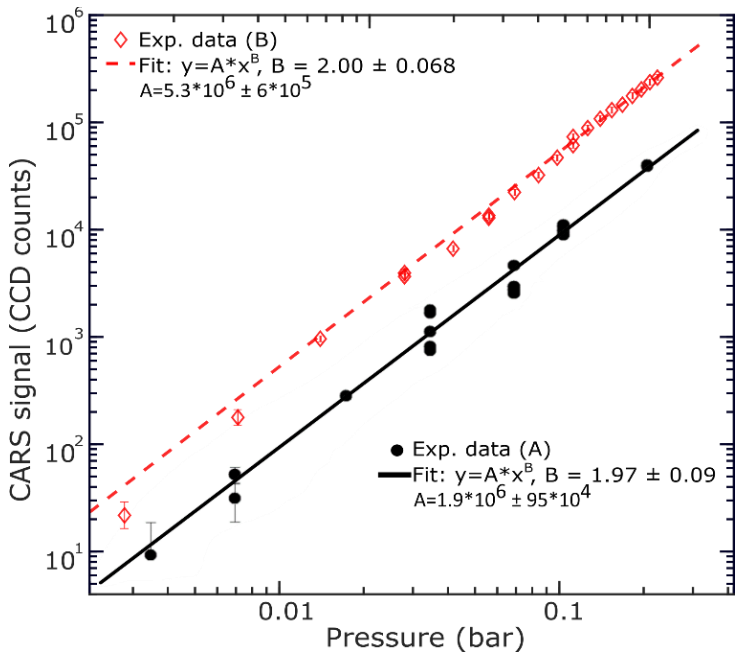

Figure 3-3. CARS signal dependence on O_2 partial pressure at constant total pressure in the cell (black circles, solid line), and at constant gas mixture at different pressures in the cell (red diamonds, dashed line). Both fittings are performed using "power1" fit in MATLAB R2016b (MathWorks, Natick, MA, USA). 95% confidence bounds are provided for each fitting parameter.

In the next set of experiments, we replace the gas cell with a 1 mm round nozzle connected to a cylinder with N_2 gas and pointed in the direction perpendicular to the beams propagation. Hereafter, we obtain the CARS signal for O_2 molecules in ambient air in front of the nozzle in the vicinity of the focal plane of the beam (Figure 3-4), where zero of the X-axis corresponds to the nozzle surface and zero of the Y-axis to the center of the

nozzle. After we set the gas pressure such that the gas flow from the nozzle remains constant (estimated at ≈4.5 m/s), we move the nozzle in a direction transverse to the axis of the beam propagation direction (Y and X axes in the figure). Hence, by obtaining the CARS signal for O_2 at various nozzle positions it becomes possible to visualize the flow of nitrogen from the nozzle. One can see that the nitrogen flow stays almost symmetric about the zero of the Y-axis as it propagates away from the nozzle, where the slight slope can be due to a tilt of the nozzle. The CARS signal from oxygen in the central part of the flow increases very slowly as the nitrogen diffuses into the surrounding air.

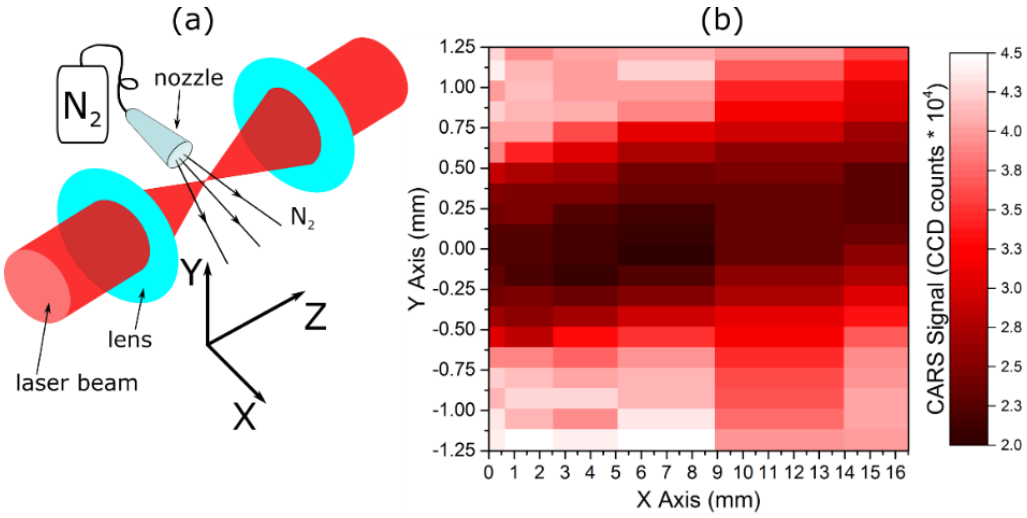

Figure 3-4. N_2 flow as it displaces air: (a) Setup schematics; (b) the CARS signal from O_2 in front of the nozzle. Darker regions correspond to higher concentrations of nitrogen.

Next, we add a thin metal plate (50 × 20 × 0.5 mm) in front of the nozzle to examine the resulting flow disturbance (Figure 3-5). The plate is placed at a distance 5.9 mm away from the nozzle surface in such a manner that the top half of the nozzle is blocked by the plate. The thin plate acts as an impenetrable barrier/obstacle for the gas and laser beams. The flow is disturbed and no longer symmetric; points with zero CARS signal mark the

plate location. Moreover, the signal decreases in front of the plate as the nitrogen flow is partially redirected along the surface, while another portion of the flow is deflected by the plate downward. Right behind the barrier, the signal is restored to its value in ambient air since the nitrogen flow cannot penetrate through the plate; i.e., the air in this region stays undisturbed.

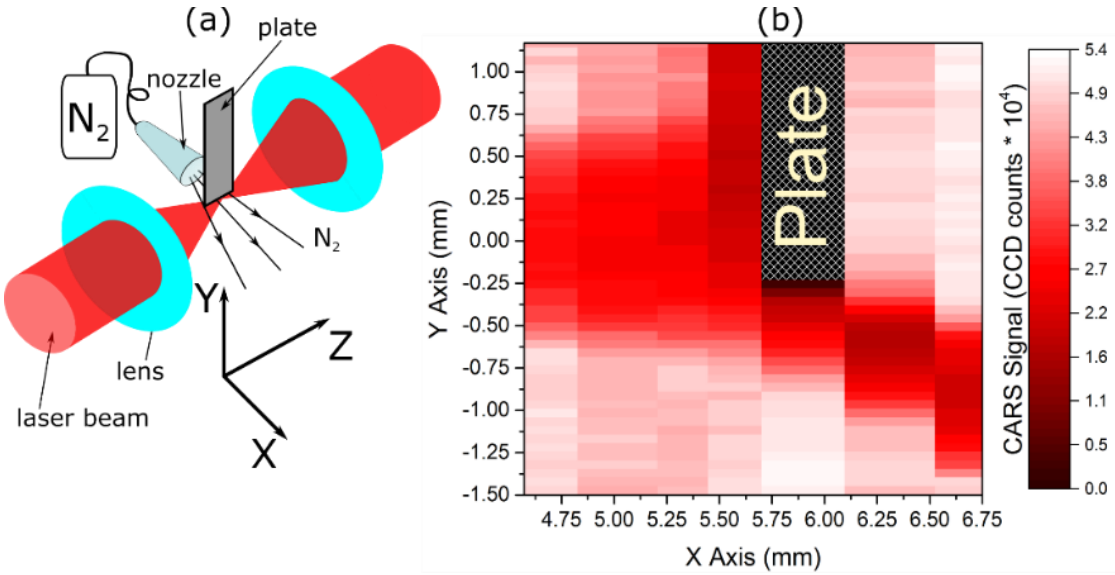

Figure 3-5. N_2 flow as it displaces air with a flat barrier plate placed in front of the nozzle. (a) Setup schematic; (b) O_2 CARS signal from air in front of the nozzle. Darker regions correspond to higher concentrations of nitrogen.

3.4. Conclusion

We have experimentally demonstrated the quadratic dependence of the CARS signal of the Q-branch vibrational transition of molecular oxygen on the number of O_2 molecules in a gas mixture. We examined two cases. In the first, the mixture was prepared with various amount of background molecules but at constant total pressure. In the second case, the mixture composition remained unchanged while the pressure was varied. No significant difference between these cases was found as both signals showed quadratic

dependence on the number of molecules. Furthermore, we have illustrated how CARS can be used for the visualization of gas flow in a simple, free-space configuration, both with a plate barrier and without it. We believe this method is applicable for performing gas flow images for any molecules with any Raman-active modes, as long as the CARS signal can be retrieved with a suppressed non-resonant background.

Clearly, the imaging of the gas flow demonstrated in Figure 3-5 could not be achieved without the N^2 enhancement provided by CARS. Spontaneous Raman spectroscopy even with the DUV excitation (Figure 2-5 and Figure 2-11) still requires tens of seconds acquisition times to obtain signals with a reasonable signal-to-noise ratio. While in CARS spectroscopy the similar levels of signals can be achieved in a fraction of second. Additionally, CARS can be combined with the electronic resonant enhancement to yield even stronger signals [106]. However, the enhancements for Raman scattering are not limited by the electronic resonance and vibrational coherence. As we will see from the following chapter, the nanoparticles significantly alter both spontaneous and coherent Raman spectroscopy and provide even higher enhancements than CARS.

4. SURFACE-ENHACED RAMAN SCATTERING AND SURFACE-ENHANCED COHERENT RAMAN SCATTERING*

Raman spectroscopy is a powerful tool for molecular chemical analysis and bio-imaging, which shows an astonishing sensitivity when combined with a huge enhancement by the coherence and surface effects. Noble metal nanoparticles have been commonly used for the spontaneous surface-enhanced Raman scattering (SERS) and for the surface-enhanced coherent anti-Stokes Raman scattering (SECARS) spectroscopies, as they provide large enhancement factors via the electromagnetic and chemical mechanisms. Recently, two-dimensional (2D) semiconductors, such as monolayer molybdenum disulfide (MoS_2), were used for the potential SERS applications as cheaper substrates compared to the noble metal nanoparticles. However, the coherent enhancement of SECARS on 2D materials has not been previously explored. Here we present the experimental SECARS measurements of pyridine-ethanol solutions containing 2D MoS_2 nanocrystals with the giant chemical enhancement factor of 10^9 over coherent anti-Stokes Raman scattering (CARS), which is attributed to the charge transfer states and resonant MoS_2 excitation. As a comparison, the SERS signals on MoS_2 using incoherent nonresonant excitation show at least two orders of magnitude smaller enhancement. Time-resolved SECARS measurements directly reveal the increased vibrational dephasing rates

* Part of this chapter is reprinted with permission from "Giant chemical surface enhancement of coherent Raman scattering on MoS2." by Shutov, A.D., Yi, Z., Wang, J., Sinyukov, A.M., He, Z., Tang, C., Chen, J., Ocola, E.J., Laane, J., Sokolov, A.V. and Voronine, D.V., 2018. ACS Photonics, 5(12), pp.4960-4968., Copyright [2018] by American Chemical Society.

which provide strong evidence for the charge transfer in the pyridine-ethanol-MoS_2 system.

4.1. Giant chemical surface enhancement of coherent anti-Stokes Raman scattering on MoS_2

4.1.1. Introduction

Surface-enhanced Raman scattering (SERS) has developed into a powerful spectroscopic technique [15,107–109] with the astonishing sensitivity probing even single molecules [110–112]. The SERS enhancement factor (EF) has contributions of two surface effects, namely, the electromagnetic mechanism (EM) and the chemical mechanism (CM). The EM contribution is due to the enhanced local fields of surface plasmons in metallic nanostructures. The corresponding EF varies strongly with the shape [113–115], nanoparticles distribution [116,117], and laser excitation energy [118–121], and can reach up to 10 orders of magnitude. On the other hand, the CM enhancement is due to the chemical interaction between the investigated molecules and the SERS substrate or the colloidal SERS nanoparticles. The CM contribution to the EF is typically much smaller than the EM contribution and can reach up to 2 orders of magnitude for noble metals [122–124].

Noble (gold, silver) metallic nanoparticles and substrates are the most commonly used materials for SERS as they provide high EFs. However, SERS can be implemented with semiconductors as well [125–127], demonstrating the predominant CM enhancement. Although the first studies did not demonstrate large EFs by CM, some recent studies suggest that semiconductors [128,129] or even hybrid semiconductor/metal

structures [130,131] may be competitive with metals for some SERS applications. The semiconductor materials have a large variety of control parameters, such as a band gap, strain, doping, and nanostructure geometry which can be realized using various techniques, such as chemical vapor deposition, nanolithography, molecular beam epitaxy, and others.

Two-dimensional layered materials such as graphene [132–134] and transition metal dichalcogenides (TMD) [135,136] demonstrate a great potential for SERS applications. Recently, ultrahigh enhancement ($\sim 10^5$) of Raman scattering was demonstrated for TMD monolayer molybdenum disulfide [137] (MoS_2), which was explained by the laser excitation being resonant to the charge transfer and exciton transitions in the molecular-MoS_2 system. Monolayer MoS_2 is a direct bandgap semiconductor, with a large exciton oscillatory strength and strong photoluminescence (PL) [138–140].

Combining surface effects of SERS with the coherence effects of the coherent anti-Stokes Raman scattering (CARS) may result in surface-enhanced coherent anti-Stokes Raman scattering (SECARS) with even higher enhancement of SECARS over CARS (theoretically 10^8 – 10^{24} and practically $\sim 10^7$) [141]. The CARS signal depends on the square number of molecules [42], and $\sim 10^6$ enhancement of CARS over the spontaneous Raman signal may be achieved [142]. Typically, SERS measurements involve a small number of molecules. Nevertheless, SECARS measurements have been successfully demonstrated mostly on the metallic and hybrid substrates [100,102,143–146]. However, in the coherent nonlinear optical process such as SECARS, the phases of the electric fields play an important role, especially for the EM enhancement. The destructive interference

between the local electric fields of the nanostructures and the incident laser electric field can significantly decrease the EF and the resultant CARS signal [102,147]. On the other hand, the semiconductor substrates do not have this shortcoming as they show mainly the CM enhancement. In this work, we investigate how the MoS_2 nanoparticles (NPs) affect the CARS signal of pyridine (C_5H_5N). We perform time resolved SECARS measurements on the solution containing pyridine, ethanol (C_2H_5OH), and MoS_2 NPs.

Pyridine is a commonly used molecular analyte for SERS and SECARS studies due to its well-known Raman spectrum and strong Raman scattering signals. However, a mixture of pyridine and other molecules with OH groups is no longer a binary system [148], as pyridine tends to form hydrogen-bonded complexes. Both theoretical and experimental studies of pyridine mixtures with water [100,149], methanol [150] and ethanol [151] demonstrate the appearance of a new Raman signal around 997 cm^{-1} due to hydrogen-bonded pyridine complexes. Hydrogen bonding also affects the vibrational dephasing rates [152,153].

The nonresonant four-wave mixing (NR FWM) background suppression becomes crucial for performing CARS measurements on the samples containing multiple molecular species [97]. To address this issue we employ the femtosecond adaptive spectroscopic technique for CARS (FAST CARS) [95]. This technique combines the broadband excitation of the vibrational coherence by the femtosecond (fs) pump/Stokes pulses with the delayed probing by the shaped picosecond (ps) probe pulse (Figure 4-1). By optimizing the time delay as well as the spectral bandwidth of the probe pulse we can achieve suppression of the NR FWM background. Moreover, a great flexibility in selecting the

spectral width and the duration of the probe pulse allows studying vibrational signals in both spectral and temporal domains, i.e. obtaining dephasing rates for vibrational modes.

In this work, we use the FAST CARS technique to study the solutions of pyridine (Py) and ethanol (EtOH) with and without MoS_2 NPs. Performing experiments on MoS_2 NPs in solution allowed to achieve significantly higher signals because of the increased interaction volume in comparison with the exfoliated or CVD-grown MoS_2 samples. The number of MoS_2-Py-EtOH complexes that contribute to the SECARS signal is larger in the bulk solution than on the surface, and the SECARS signal scales as the square of the number of molecular complexes, which provides large chemical enhancement factors reported in this work. Moreover, performing the measurements in the liquid media minimizes the potential heat damage. Additionally, it gives the direct comparison between the signals with and without MoS_2 NPs under identical experimental conditions. Although similar experiments on solid substrates are, in principle, possible, they are more challenging in terms of the experimental arrangement. We observe the appearance of the blueshifted ring breathing mode of pyridine and the decrease of the vibrational dephasing times in the presence of MoS_2. We show that nanomolar concentration of MoS_2 NPs decreases the dephasing time and significantly alters the Raman spectrum of pyridine. Finally, we demonstrate SECARS on MoS_2 due to the giant CM enhancement.

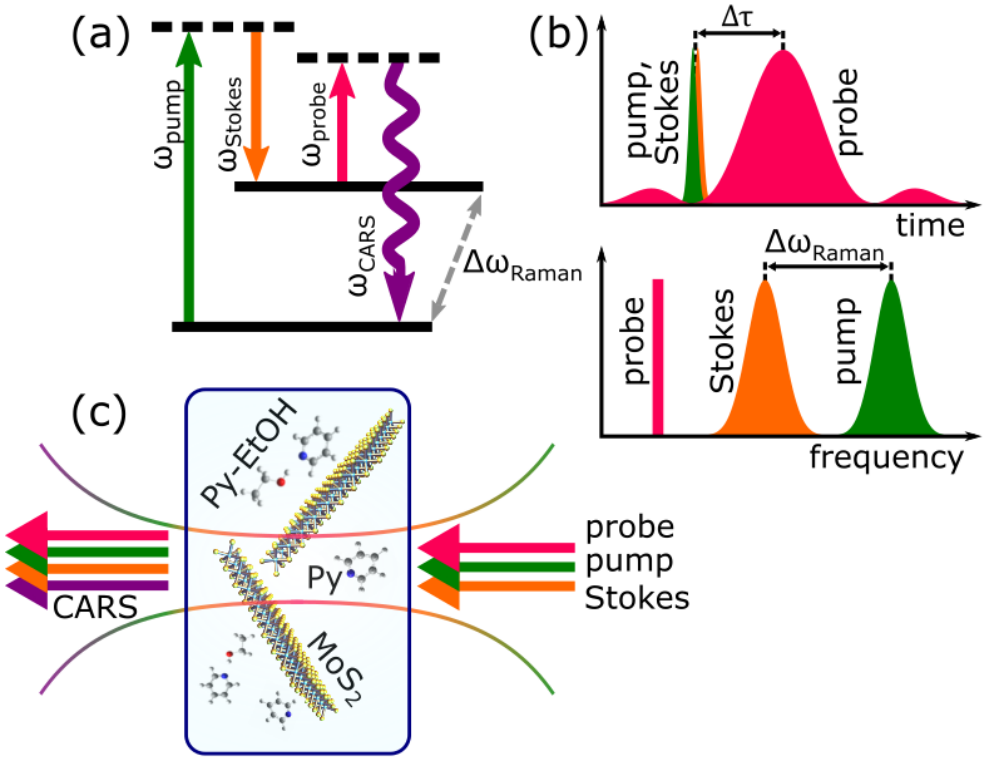

Figure 4-1. Schematics of the time resolved SECARS experimental setup: (a) Energy level diagram of the CARS process. The molecular vibrational coherence is prepared by the pump (ω_{pump}) and Stokes (ω_{Stokes}) pulses. The CARS signal (ω_{CARS}) is generated by the probe pulse (ω_{probe}) scattering off the molecular vibration. (b) Time and frequency domain representations of the incident laser pulses. The narrowband (5 – 13 cm^{-1}) probe pulse has a duration of several ps, sinc-shape and is delayed ($\Delta\tau$) with respect to the broadband fs pump/Stokes pulses, which are two-photon resonant with the molecular vibrational modes ($\Delta\omega_{Raman}$). (c) Schematic of the (SE)CARS signal generation. The collinearly propagating pump, Stokes and probe beams are focused into the sample cell containing a mixture of pyridine (Py) and ethanol (EtOH) molecules, as well as MoS_2 nanoparticles and their complexes. The CARS signal is generated in the focal spot of the lasers and is collected in the same direction as the propagating laser beams.

4.1.2. Experimental details

4.1.2.1. Sample preparation

The CARS experiments were performed with the sample containing 200 µl of pure pyridine, and then 10 µl of the ethanol solution containing MoS_2 NPs (2D Semiconductors,

SOL-MOS2) was added. The concentration of MoS_2 NPs in ethanol solution was 92 µg/cm^3. The control measurements were performed for the solution containing 200 µl pyridine and 10 µl of ethanol without MoS_2.

4.1.2.2. Experimental setup

The experimental arrangement was previously reported [59] and its layout is presented in the section 3.2 (Figure 3-1(c)). As a laser source, we employ a Ti:sapphire regenerative amplifier (1 kHz repetition rate, 0.7 mJ/pulse, Legend, Coherent, Santa Clara, CA, USA) with two equally pumped optical parametric amplifiers (OPAs: OPerA-VIS/UV and OPerA-SFG/UV Coherent, Santa Clara, CA, USA). The outputs of the two OPAs are used as pump and Stokes pulses (<130 fs). The central wavelengths (spectral FWHM) of the pump and Stokes pulses were 555 nm (10.9 nm, ≈354 cm^{-1}) and 589 nm (11.2 nm, ≈323 cm^{-1}), respectively. Therefore, they generated the vibrational coherence at $\Delta\omega_{Raman}\approx$1000 cm^{-1}. The spectral width and duration of the ps probe pulse were controlled by the slit width in the pulse shaper. We performed measurements for 2 different slit sizes: 10 µm and 180 µm, which correspond to the spectral FWHM of approximately 5 cm^{-1} and 13 cm^{-1}, respectively. We used low pulse energies for the pump, Stokes and probe beams (1.1 µJ, 0.07 µJ, and 0.16/0.98 µJ for 10/180 µm slit size) at 1 kHz repetition rate to prevent optical damage of the sample. All three collinearly propagating beams were focused into the test cell (Spectrosil® Quartz, 2 mm optical path, Starna Cells, Inc, Atascadero, CA, USA) containing the liquid sample. The generated CARS signal after passing through a set of filters (FW2AND Thorlabs, Newton, NJ, USA; FF01-732/68 Semrock, Rochester, NY, USA) was sent to the spectrograph (Chromex Spectrograph 250is, Albuquerque, NM,

USA), with a liquid-nitrogen-cooled CCD camera (CCD: uncoated Spec-10:400B, Princeton Instruments, Trenton, NJ, USA). The CCD camera exposure time was set to 1 s for all CARS measurements. The spectrograph was calibrated with Hg (Ar) spectral calibration lamp (6035, Newport, Irvine, CA, USA).

4.1.3. Results

4.1.3.1. 2D spectrograms

We collect the CARS spectra for multiple time delays of the probe pulse with respect to the pump/Stokes pulses and plot them as 2D spectrograms (Figure 4-2). The maximum signal intensity (log) is normalized for each measurement independently and the constant offset background is subtracted. The CARS signal is a function of the probe pulse delay $\Delta\tau$ (x-axis) and Raman shift (y-axis). The mole fraction of ethanol remains the same (6.5×10^{-2}) for the cases with and without MoS_2 NPs (Figure 4-2(c) – (f)), while MoS_2 concentration is 4.4 μg/cm^3 (Figure 4-2(c) – (d)).

The Raman 2D spectrogram for pure pyridine (Figure 4-2(a)) demonstrates two Raman lines at 989 cm^{-1} and 1029 cm^{-1}, corresponding to the ring breathing and the second totally symmetric ring stretching mode of pyridine, respectively. The narrowband probe pulse (≈5 cm^{-1}) in the 10 μm slit size case provides a better spectral resolution at the cost of the background suppression since the probe pulse is stretched in the temporal domain. Moreover, the investigation of the vibrational dephasing dynamics becomes complicated, as the signal becomes convoluted with the temporal profiles of the laser pulses. To overcome these difficulties, we also perform measurements for the larger slit size (180 μm), i.e. a shorter probe pulse.

Similar to the case with the narrowband probe pulse, the 2D spectrogram with the broadband probe (Figure 4-2(b)) contains two vibrational lines. However, both signals are broadened in the y-axis due to the spectrally broader probe pulse (≈13 cm^{-1}). As the signals decay with longer probe pulse delays, the single Raman lines split into several lines due to the interference between the resonant signal from the molecular vibrations and the NR FWM background. The background is strong around the zero probe pulse time delay, as it temporally overlaps with the pump and Stokes pulses, and its temporal profile along the x-axis follows the sinc-shape of the probe pulse. As the probe pulse node overlaps with the pump/Stokes pulses, the NR background becomes almost completely suppressed. Consequently, from this spectrogram we can determine the ideal probe time delay for the background suppression at approximately 2.6 ps. At the same time, the vibrational coherence generated by the pump and Stokes pulses decays on a longer time scale.

After adding the solution of MoS_2 NPs in ethanol to pyridine we observed the appearance of a new strong signal at 999 cm^{-1} in the 2D spectrograms (Figure 4-2(c) and (d)). Because of the long (≈7 ps) probe pulse duration, the NR background is not completely suppressed (Figure 4-2(c)). Moreover, the pump and Stokes pulses excite a strong PL signal in MoS_2. The vibrational signals for the sample with MoS_2 have more complicated beat patterns (Figure 4-2(d)) at longer probe pulse time delays, especially for the ring breathing mode in the region of 985-1000 cm^{-1}.

Finally, we perform control measurements for the mixture of pyridine and ethanol without MoS_2. The mole fraction of ethanol (0.065) remained the same as for the sample with MoS_2. The 2D spectrograms (Figure 4-2(e) and (f)) show the increased NR

background due to the presence of ethanol molecules, but do not reveal the presence of a new vibrational mode around 999 cm^{-1}. Therefore, to perform a more detailed analysis we investigate the line profiles as the traces obtained from the 2D spectrograms along the x- and y-axes at the maxima of the Raman signals for the 3.5 (2.6) ps probe pulse delay for 10 (180) μm slit size, respectively (Figure 4-3).

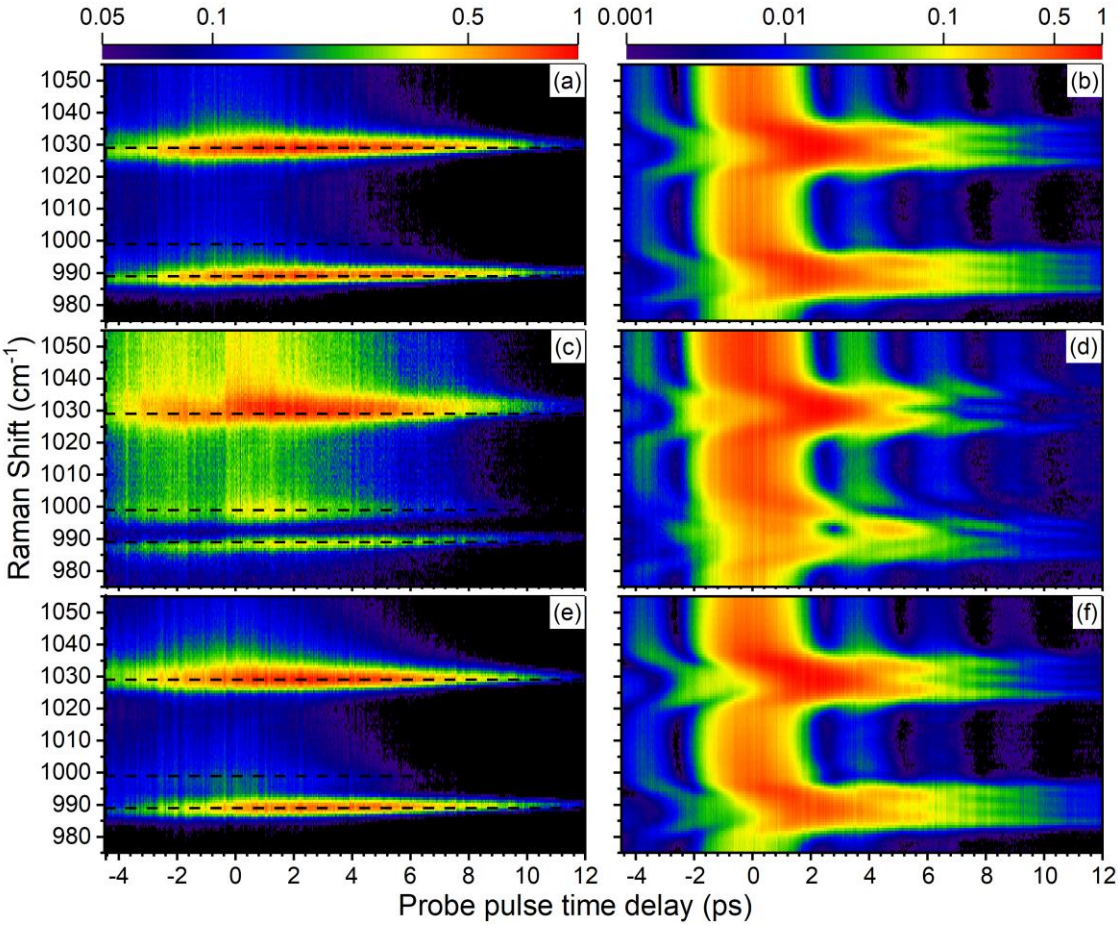

Figure 4-2. CARS 2D spectrograms show the normalized intensity (log) of the CARS signal as a function of the Raman shift and probe pulse time delay for two slit sizes (10 μm for a, c, e and 180 μm for b, d, f) of pure pyridine (a, b), pyridine-MoS_2-ethanol solution (c, d), and pyridine-ethanol solution (e, f). The mole fraction of ethanol for all cases in (c) – (f) is the same. Horizontal dashed lines mark the vibrational modes at 989, 999 and 1029 cm^{-1}. The slit size determines the spectral bandwidth of the probe pulse: 10 μm and 180 μm slit sizes correspond to the probe bandwidth of ≈5 and ≈13 cm^{-1}, respectively.

4.1.3.2. Line profiles

Figure 4-3(a) shows the line profiles of the CARS spectra of pure pyridine (black) and pyridine-ethanol solutions with (red) and without (blue) MoS_2 for the 10 μm slit size. The spectra were vertically offset for clarity and the additional baseline subtraction was performed.

We observe a weak blueshifted ring breathing mode signal in the spectrum of the pyridine-ethanol solution without MoS_2 (Figure 4-3(a) inset), that is caused by the formation of the pyridine and hydroxyl group complexes. Figure 4-3(a) shows that the presence of MoS_2 significantly enhances the signal of this vibrational mode, as the ethanol concentration remains the same. Additionally, we observe the broadening of the 999 and 1029 cm^{-1} signals compared to the 989 cm^{-1} signal, which is the indication of the modified dephasing dynamics. The CARS signals for 180 μm slit demonstrate similar behavior (Figure 4-3(b)). The signal of the blueshifted ring breathing mode at 999 cm^{-1} for the sample containing MoS_2 is at least 15 times larger than for the sample without it.

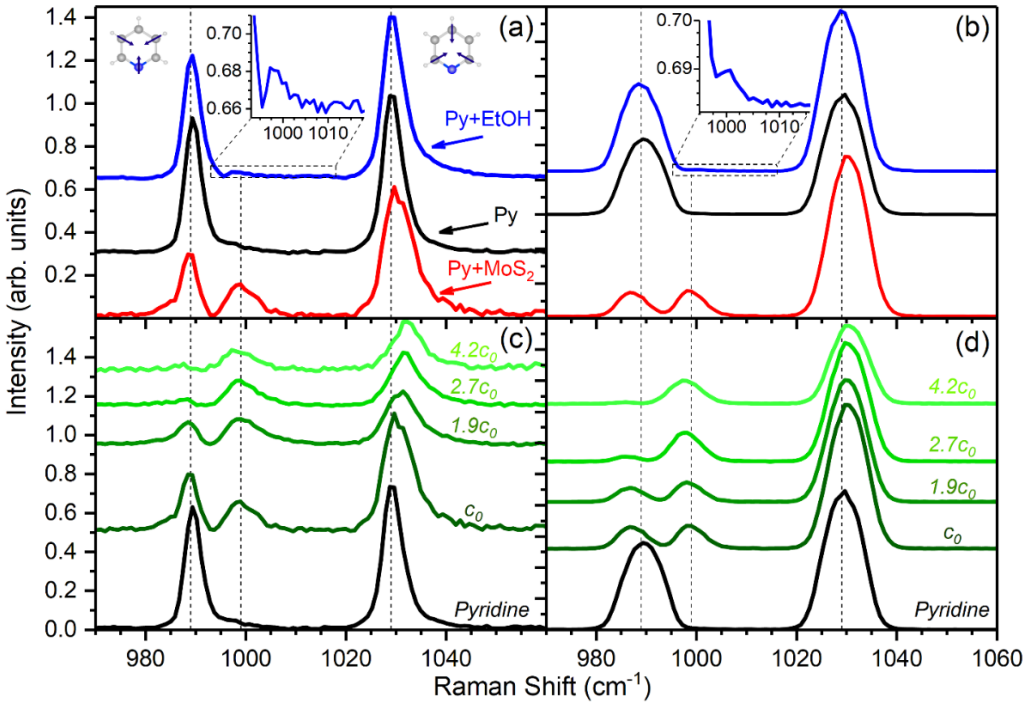

Figure 4-3. Spectral line profiles obtained from the 2D CARS spectrograms for various MoS_2 and ethanol concentrations. (a) 10 µm slit size: pyridine (Py, black), pyridine-ethanol solution with MoS_2 (Py+MoS_2, red), pyridine-ethanol solution without MoS_2 (Py+EtOH, blue). Vertical dashed lines indicate the positions of 989 cm^{-1} and 999 cm^{-1} (ring breathing) and 1029 cm^{-1} (ring stretching) modes. The inset shows the zoomed spectral region of 990-1020 cm^{-1}. (b) Same as (a), but for the 180 µm slit size. (c) Spectral line profiles for different MoS_2 concentrations $N \times c_0$, where c_0 is 4.38 µg/cm^3 and N varies from 0 to 4.2, where $N = 0$ corresponds to pure pyridine (black). (d) Same as (c), but for the 180 µm slit size. All spectra are offset for clarity with the baseline removed.

Figure 4-3(c) and (d) show the normalized spectral line profile concentration dependence for 10 µm and 180 µm slit sizes, respectively, with several similar features. The intensity of the new ring breathing mode at 999 cm^{-1} gradually increases with the increasing concentration of MoS_2. In contrast, the pure pyridine signal at 989 cm^{-1} decreases and shows a small redshift of approximately 1 cm^{-1} for the 10 µm slit size. This shift is greater (4 cm^{-1}) for the 180 µm slit, as the probe pulse spectrum is broader for this

slit size. The ring stretching mode (1029 cm^{-1}) blueshifts for both slit sizes with the increase of the MoS_2 concentration.

Both spectral lines of the ring breathing and ring stretching modes of pyridine blueshift and broaden with higher concentrations of MoS_2 and ethanol. Since the spectral resolution of our system is limited by the relatively broad probe pulse width, as an alternative to studying the linewidth we investigate the dephasing dynamics of the vibrations.

4.1.3.3. Dephasing dynamics

Figure 4-4(a) shows the maximum intensity of the CARS signal in the 983 – 1003 cm^{-1} range, i.e. the ring breathing mode of pyridine, at different time delays of the probe pulse for the 180 μm slit. The vibrational dephasing of the ring breathing mode in pure pyridine and pyridine-ethanol solution takes place on similar timescales of 5.62 ± 0.03 and 5.25 ± 0.03 ps, respectively, in agreement with previous reports [100,152,153]. Here, the beating between the ring breathing modes of the pyridine-ethanol complex (999 cm^{-1}) and the free pyridine (989 cm^{-1}) cannot be detected because the intensity of the 999 cm^{-1} signal is more than 500 times smaller than that of 989 cm^{-1}.

In contrast, for the pyridine-ethanol mixture with MoS_2 the blueshifted ring breathing mode is strongly enhanced, and the beating between the two ring breathing modes is clearly seen in Figure 4-4(a). Moreover, the 989 cm^{-1} mode dephasing time constant decreases to 4.93 ± 0.09 ps in the presence of MoS_2.

In addition to the oscillatory beating signal of the ring breathing mode, there is a low amplitude oscillation of the NR background in all the measurements due to the sinc probe

pulse shape [154] that can be seen in 2D spectrograms (Figs. 2(b), 2(d) and 2(f)). As a result, the signals of the ring stretching vibrational mode of pyridine (Figure 4-4(b)) show weak oscillation behavior. For the sample containing MoS_2 the effect is stronger, because of the higher background level due to the contribution of the MoS_2 PL signal. We note that taking into account the probe pulse shape (Figure 4-4(b), the dashed line) for the fitting procedure did not affect the derived dephasing time constant, as it remained the same.

The dephasing time constants of the ring stretching vibrational mode for pyridine and pyridine-ethanol solution without MoS_2 are similar (3.89 ± 0.02 ps and 3.58 ± 0.02 ps, respectively), while the addition of MoS_2 further decreases the dephasing time (2.86 ± 0.01 ps). Further increasing MoS_2 and ethanol concentrations does not significantly change the dephasing time (Table 4-1). Similar behavior was demonstrated for the dephasing of the vibrational bands of pyridine-water complexes at higher water concentrations [152].

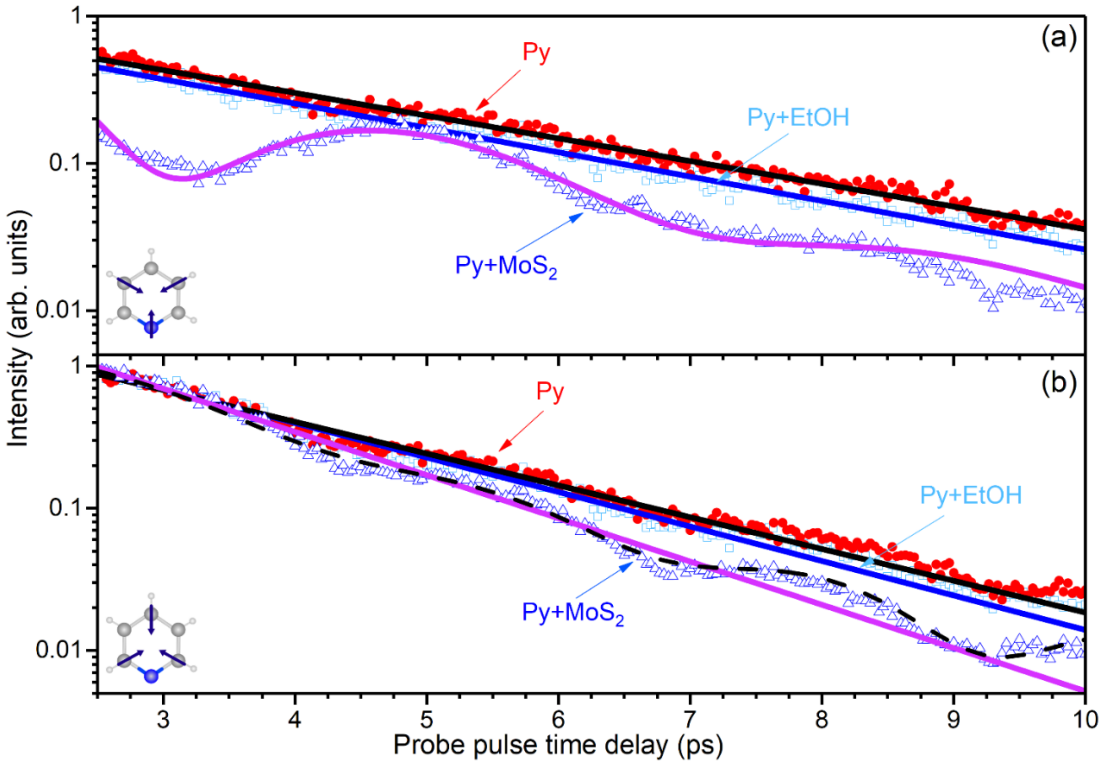

Figure 4-4. Temporal line profiles obtained from the 2D spectrograms show dephasing dynamics of pyridine vibrational modes for the 180 μm slit size for the maximum signal intensity from (a) the 983 - 1003 cm^{-1} range (ring breathing mode) and (b) the 1023 – 1037 cm^{-1} range (ring stretching mode) along with the fitting curves. Symbols represent experimental data, and curves represent the fitting: red circles, black curves (Py) – pure pyridine; light blue squares, blue curves (Py+EtOH) – pyridine and ethanol solution without MoS_2; blue triangles, purple curves (Py+MoS_2) – pyridine-ethanol solution with MoS_2. The dashed black line shows the fit to the Py+MoS_2 experimental data, taking into account the sinc probe pulse shape (see section 4.1.3.4 for fitting details).

Table 4-1 Fitting parameters for the temporal CARS maximum intensity profiles which correspond to the data shown in Figure 4-4 and Figure 4-5. The amplitudes A_i in each fit were normalized to the maximum intensity.

Parameter (std. dev.)	**MoS_2 concentration, µg/cm^3** ***(mole fraction of ethanol)***					
	0 *(0)*	0 *(0.017)*	4.4 *(0.017)*	8.4 *(0.034)*	12.0 *(0.050)*	15.3 *(0.080)*
A_1, a.u.	1.78 (0.01)	1.08 (0.01)	2.38 (0.01)	2.43 (0.01)	2.22 (0.01)	2.11 (0.01)
t_1, ps	3.89 (0.02)	3.58 (0.02)	2.86 (0.01)	2.69 (0.01)	2.68 (0.01)	2.56 (0.01)
A_2, a.u.	1.12 (0.01)	1.93 (0.01)	0.88 (0.02)	0.92 (0.02)	1.04 (0.05)	0.08 (0.02)
t_2, ps	5.62 (0.03)	5.25 (0.03)	4.93 (0.09)	4.13 (0.08)	3.15 (0.12)	5.12 (2.00)
A_3, a.u.	–	–	0.82 (0.08)	0.75 (0.07)	0.29 (0.05)	1.25 (0.12)
t_3, ps	–	–	2.11 (0.10)	2.11 (0.11)	2.44 (0.23)	2.45 (0.11)
$\tilde{\nu}_{23}$, cm^{-1}	–	–	8.07 (0.10)	8.35 (0.11)	9.18 (0.23)	10.45 (0.49)

4.1.3.4. Fitting procedure

To fit the experimental data, we used the following general equations for the CARS signal intensity:

$$I_{CARS} = A_1^2 \exp\left(-\frac{2t}{t_1}\right), \quad (4.1)$$

and

$$I_{CARS} = A_2^2 \exp\left(-\frac{2t}{t_2}\right) + A_3^2 \exp\left(-\frac{2t}{t_3}\right) + 2A_2A_3 \exp\left(-\frac{t}{t_2} - \frac{t}{t_3}\right)\cos(2\pi c\tilde{\nu}_{23}t - \phi_{23}), \quad (4.2)$$

where A_1, t_1 correspond to the intensity and dephasing time in the case of a single oscillation mode, e.g. ring stretching mode or ring breathing mode without MoS_2. In turn, A_2, t_2; A_3, t_3 correspond to the intensities and dephasing times when the beating between the ring breathing modes (989 and 999 cm^{-1}) with and without MoS_2, respectively, is present. The fitting parameter $\tilde{\nu}_{23}$ corresponds to the energy difference between the two ring breathing modes, while ϕ_{23} is a phase factor. All fittings were performed using Mathworks MATLAB 2016b *fit* function.

The experimental data in Figure 4-2(c) and (f) shows the maximum intensity of the CARS signal corresponding to the two vibrational modes: ring breathing (983-1003 cm^{-1}) and ring stretching (1023-1037 cm^{-1}). The width of the regions corresponds to the approximate spectral width of the probe pulse. As the ring breathing mode signals without added MoS_2 do not show any beating behavior, we used the Equation 4.1 to fit the data for both the pyridine and pyridine-ethanol samples (Figure 4-4). To fit the data with added MoS_2, we used Equation (4.2) since the signal exhibited a beating pattern in this case. For

the ring stretching mode (Figure 4-4(b)) we performed fitting using the Equation (4.1) for all the cases, as no beating was detected.

Table 4-1 shows fitting parameters for all cases examined in this work. We observed the decrease of the dephasing time constants t_1 and t_2 for the pyridine vibrational modes at 989 cm^{-1} and 1029 cm^{-1} with the increase of the MoS_2 concentration. On the contrary, the dephasing time t_3 for the ring breathing mode of the Py-EtOH MoS_2 complex at 999 cm^{-1} was lower than t_1 and did not change significantly with the increase of MoS_2.

Figure 4-5 shows experimental data and fitted curves for various MoS_2 concentrations. The ring stretching mode signal (Figure 4-5(b)) showed weak modulations of all the experimental signals due to the effect of the sinc-shaped probe pulse.

To take into account the probe pulse shape we fit the experimental data for 4.4 $\mu g/cm^3$ MoS_2 concentration (Fig. 4b, the dashed line) with the following equation:

$$I_{CARS} = \left(A_1 \exp\left(-\frac{t}{t_1}\right)\right)^2 + \left(A_2 \frac{\sin(\pi \Delta \nu t + \phi)}{t}\right)^2 + c_1, \qquad (4.3)$$

where the second term represents the intensity profile of the probe pulse, while c_1 is a constant background noise. Keeping the dephasing time $t_1 = 2.86\, ps$ fixed and assuming the bandwidth of the probe pulse $\Delta\nu = 0.39\, THz$, for the fitting parameters A_1, A_2, ϕ, c_1 we obtain following values (std. dev.): 2.18 (0.01), 0.93 (0.02), 2.01 (0.05), 0.0014 (0.0003). Thus, we conclude that the NR background oscillations do not affect the value for the derived dephasing time constant.

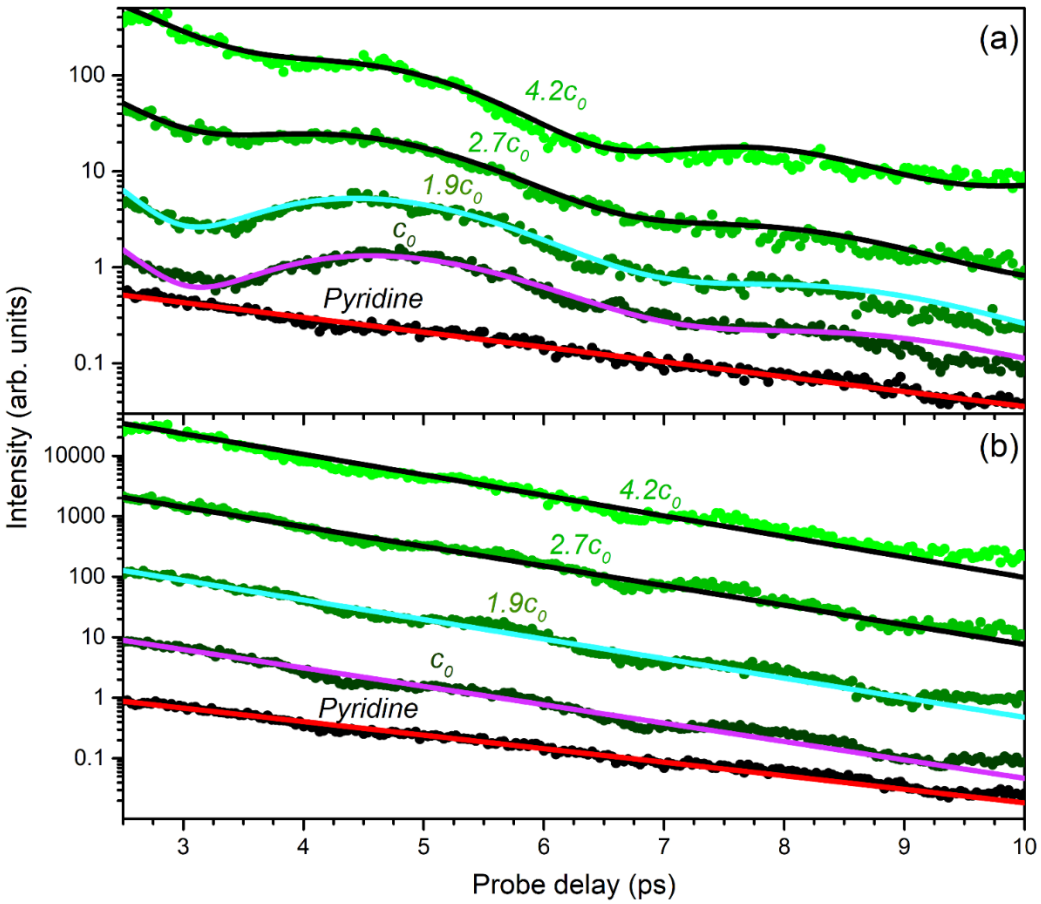

Figure 4-5. Temporal CARS intensity profiles for (a) ring breathing and (b) ring stretching vibrational modes for various MoS_2 concentrations $N \times c_0$, where c_0 is 4.38 µg/cm^3. The curves were offset for clarity.

4.1.3.5. Enhancement Factor (EF)

The calculation of the EF values is challenging for solutions. However, we can obtain the low estimate by comparing the CARS and SECARS signals [141].Therefore, for calculating the EF of SECARS over CARS we assume that the CARS signal at 999 cm^{-1} is mainly due to the pyridine-ethanol complexes and is enhanced by the presence of MoS_2. In this case, we can obtain the low estimate of the EF assuming that all ethanol-pyridine complexes within the laser focus contribute to the CARS/SECARS signals. Then we

compare the peak intensities at 999 cm^{-1} (Figure 4-3(a) and (b)) for the samples with and without MoS_2, taking into account concentrations of ethanol and MoS_2 NPs. The estimated EF is 4.87×10^9 for the 180 μm slit size and 1.95×10^9 for the 10 μm slit size. The details of the EF calculations are provided in the section 4.1.3.6.

4.1.3.6. Enhancement factor for SECARS vs CARS

The effect of MoS_2 is most obvious at 999 cm^{-1} (Figure 4-3). We calculated the enhancement factor (EF) for SECARS compared to CARS using the following relation:

$$EF = \frac{I_{SECARS}}{I_{CARS}} \times \left(\frac{N_{CARS}}{N_{SECARS}}\right)^2, \qquad (4.4)$$

where I_{SECARS} is the maximum SECARS signal in CCD counts for the blueshifted ring breathing mode at 999±2 cm^{-1} for the sample with pyridine, ethanol and MoS_2, while I_{CARS} is the maximum CARS signal for the sample containing only pyridine and ethanol. N_{SECARS} is the total number of (MoS_2) unit cells in the 2D MoS_2 nanoparticles which we assume to be monolayers for the EF calculations for simplicity (partial aggregation of these monolayers is also possible). Moreover, we assume that pyridine-ethanol complexes interact with S atoms on the surface of MoS_2. N_{CARS} is the number of ethanol molecules. We consider that all molecules are equally distributed within the laser focal region, and that all ethanol molecules form complexes with pyridine molecules in the focal volume and contribute to the generation of the CARS signal. This gives a low estimate of EF. The actual EF value may be larger, because of the possibly smaller number of molecules and MoS_2 NPs contributing to the enhancement due to the possible aggregation of the nanoparticles.

The MoS_2 concentration in the sample was 4.38, 8.36, 12, 18.4 μg/cm^3 while the sample total volume was 0.21, 0.22, 0.23, 0.25 cm^3. Pyridine and ethanol mole fractions were 0.94, 0.88, 0.83, 0.74 and 0.065, 0.12, 017, 0.26, respectively. The initial volume of pyridine was 0.2 cm^3, i.e. 2.48*10^{-3} mol. Hence, the concentration of MoS_2 was at least 5 orders of magnitude smaller than the concentration of ethanol and pyridine.

The estimated laser focal spot diameter was 40 μm and the Rayleigh length was 0.4 mm. We assume that the CARS signal is generated in the cylinder which height is twice the Rayleigh length and diameter equals to the laser spot size. Then we estimate the focal volume of $\pi \times (20\,\mu m)^2 \times 2 \times 400\,\mu m \approx 1000000\,\mu m^3 = 10^{-6} cm^3$.

For the 180 μm slit size, 4.38 μg/cm^3 concentration of MoS_2, 0.065 mole fraction of ethanol and 0.21 cm^3 total sample volume we have $I_{SECARS} = 995$ CCD counts, $N_{SECARS} = 1.64 \times 10^9$, $I_{CARS} = 176$ CCD counts, and $N_{CARS} = 4.90 \times 10^{13}$. Then using Eq. (3) we obtain EF = 4.87×10^9. Similar calculations for the 10 μm slit size give EF = 1.95×10^9.

4.1.3.7. Spontaneous surface-enhanced Raman spectroscopy (SERS)

We measured spontaneous Raman spectra by blocking the pump and Stokes beams and collecting the signal co-propagating with the probe pulse (806.9 nm) for the 180 μm slit (Figure 4-6). Because of the low pulse energy, broad bandwidth and low efficiency of Raman scattering, the two vibrational modes of pyridine are not well resolved. However, the maximum signal intensities measured for pure pyridine and pyridine-ethanol mixture with MoS_2 are similar (1787 and 1751 CCD counts). The integration times used for SERS

and SECARS were 120 s and 1 s, respectively. This gives a low estimate of $EF = 10^2$ for SECARS vs SERS.

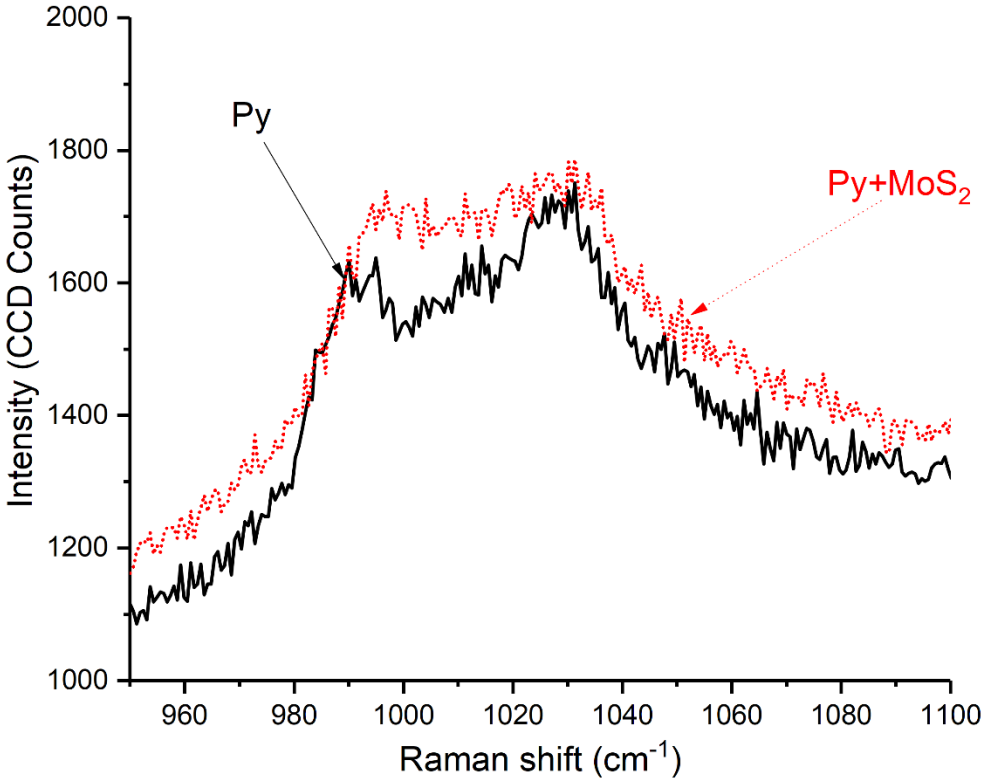

Figure 4-6. Comparison of spontaneous Raman spectra of pure pyridine (Py, black solid) and pyridine-ethanol mixture with MoS_2 (Py+MoS_2, red dotted). The integration time is 120 seconds.

4.2. Discussion

Using the time-resolved surface-enhanced CARS technique we obtained both spectral and temporal information for various mixtures of pyridine: containing pure pyridine, pyridine-ethanol complexes and pyridine-ethanol complexes with MoS_2 nanoparticles. Both the spectral and temporal profiles demonstrate a strong influence of MoS_2 on both ring breathing and ring stretching vibrational modes of pyridine. The increase of

vibrational dephasing rate, line shifts and CARS signal significantly differ from the effects of the ethanol solvent without MoS_2.

Previously it was shown that the OH group is likely to form a hydrogen bond with the N atom in pyridine [151]. Therefore, the effect of bonding is more distinctive in the Raman signal of the mode involving the movement of the N atom, i.e. the ring breathing mode at 989 cm^{-1} shifts to 999 cm^{-1}. We demonstrate that the presence of MoS_2 provides enhancement to the generated CARS signal. Due to the chemical nature of the enhancement mechanism, only the 999 cm^{-1} shifted Raman signal of the pyridine, ethanol and MoS_2 complex is enhanced. In addition, the unshifted 989 cm^{-1} signal of the unbonded free pyridine decreases with the increase of the MoS_2 NP concentration. Note that under the ideal experimental conditions the 989 cm^{-1} signal of the free pyridine should not change due to the absence of the chemical interaction between the free pyridine and MoS_2 NPs. However, the presence of MoS_2 NPs decreases the total Raman signal because of the scattering and absorption by MoS_2 NPs, which increases with the increase in NP concentration. Moreover, the number of free pyridine molecules decreases with the increased concentration of ethanol and MoS_2. These factors lead to the observed decrease of the 989 cm^{-1} signal. Here, we discuss several factors contributing to the enhancement.

A recently developed theory predicts a strong enhancement of the charge transfer (CT) transitions in semiconductors [155]. For a molecule coupled to a semiconductor, the CT transitions can borrow intensity from both the molecular and exciton transitions. They can be increased even more by choosing the laser frequency close to the molecular and exciton resonances. However, pyridine and ethanol molecular transitions occur in the ultraviolet

part of the electromagnetic spectrum [156,157] for the photon energies ≈4-5 eV, which are significantly larger than the frequencies of the lasers used in the experiment.

On the other hand, both the pump (555 nm) and Stokes (589 nm) pulses can excite excitons in MoS_2. The Stokes pulse is close to the B-exciton transition of MoS_2 [158]. The exciton enhancement mechanism is further supported by the comparison of the spontaneous Raman signals using only the probe pulse for excitation (Figure 4-6). The spontaneous Raman signal intensities of the pure pyridine and pyridine-ethanol mixture with MoS_2 are similar. The near-infrared probe pulse at 806.9 nm is far from the exciton resonances of MoS_2 and does not contribute to the enhancement. Therefore, we believe that the main contribution to the enhancement of the Raman signal arises from the CT transitions borrowing the intensity from the exciton resonances in MoS_2. The 10-20% decrease in dephasing times of both studied pyridine vibrational modes suggests the formation of CT states in the vicinity of MoS_2 [159], as well as the generation of excitons [160].

Note, that the increase of the CARS signal at 999 cm^{-1} from the pyridine-ethanol complexes can also be attributed to other mechanisms in addition to the surface enhancement by MoS_2. For example, a direct pyridine bond with MoS_2 may result in a similar blueshift of the ring breathing mode as in the case of the pyridine-ethanol complexes. Theoretical calculations predict the π- and σ- adsorption of the pyridine on MoS_2 [161]. However, recent experimental and density functional theory studies showed no direct pyridine adsorption on MoS_2 at room temperature [162]. There is currently no clear conclusive evidence of the adsorption and, therefore, this remains an open question.

Although, the potential defects (e. g. missing sulfur atoms in the lattice) in MoS_2 or hydrogen bonds formed between pyridine and ethanol can drastically modify the adsorption behavior. Therefore, we believe that ethanol plays a significant role in the enhancement mechanism, making it more complicated.

As MoS_2 is a well-known catalyst, widely used in hydrogen evolution reactions [163], we also consider the possibility of the enhancement of the formation of pyridine-ethanol complexes by MoS_2. The increased number of complexes would result in the larger Raman signal at 999 cm^{-1}. However, we discard this scenario for several reasons. In our experiments, the pyridine-ethanol complex formation always reaches the equilibrium as the measurements were performed after mixing the components at constant temperature [148]. Additionally, the mole fraction of ethanol in our experiments was kept low (0.065 – 0.26). Therefore, even if all ethanol molecules participate in the complex formation, the total number of the formed complexes would still be 2-10 times lower than in the previous studies [149,151,152]. Thus, all the formed complexes would not be able to generate such strong CARS signals as observed in the experiments.

In this study, we investigated the chemical surface-enhancement effects on the CARS spectra of the vibrational modes of pyridine in the presence of ethanol and MoS_2. The addition of ethanol and the formation of pyridine-ethanol complexes decrease the dephasing times by approximately 10% for pyridine ring breathing and ring stretching vibrational modes and cause the ring breathing mode to blueshift by ≈10 cm^{-1}. In the presence of MoS_2 these two vibrational modes of pyridine dephase approximately 20% faster because of the formation of CT states. Moreover, the CARS signal of the blueshifted

vibrational mode is significantly enhanced by MoS_2 because of the excitons generated by the pump and Stokes pulses. The small addition of MoS_2 (mole fraction in the solution ~10^{-6}) results in the EF of SECARS over CARS signal of more than 10^9. The strong excitation of charge transfer transitions borrowing intensity from the exciton transition in MoS_2 is the major contributor to the enhancement of the CARS signal.

However, the detailed mechanism of the Raman enhancement on semiconductors has not yet been completely understood. Previous studies also considered the dipole-dipole interaction mechanism as an additional contributor to SERS on MoS_2 [135]. We note that our estimated 10^9 enhancement factor could be explained by using either charge transfer alone or using both mechanisms. The reason for this unusually large enhancement factor is based on the coherent and nonlinear nature of our SECARS signal. Due to the coherent nature, the signal scales as the square of the number of molecules. Therefore, the measured ratio of the signal intensities I_{SECARS}/I_{CARS} is multiplied by the square of the surface scaling factor: $EF_{SECARS} = I_{SECARS}/I_{CARS} \times (N_{CARS}/N_{SECARS})^2$. However, the conventional SERS is an incoherent technique with the signal that scales linearly with the number of molecules: $EF_{SERS} = I_{SERS}/I_{SR} \times (N_{SR}/N_{SERS})$, where I_{SR} is the spontaneous Raman signal. Using our experimental parameters, we estimated the N_{CARS}/N_{SECARS} factor to be ~3×10^4, which gives the extra four orders of magnitude enhancement due to coherence. This provides an estimate of the conventional incoherent enhancement factor of SERS of $EF_{SERS} \sim 10^5$, which is in agreement with the previous SERS measurements on MoS_2 [137]. The additional coherent factor of 10^4 makes the estimated overall EF ~10^9, which is in agreement with the theoretical expectations [42,141,142]. In addition, there is

another important advantage of the nonlinear SECARS technique in comparison with the conventional SERS on MoS_2. It is the suppression of the strong MoS_2 photoluminescence (PL) background by using a different spectral range for signal detection. This is a well-known advantage of CARS that is very useful in this work because of the resonant excitation of MoS_2 and the inevitable contribution of the PL to the spontaneous resonant Raman signals but not to the CARS signals. This allows for obtaining larger signal-to-noise ratios, which increase the experimental EF values.

5. CONCLUSION AND FUTURE OUTLOOK

In this work, we focused on the various experimental pathways to increase efficiency of Raman scattering and, therefore, Raman spectroscopy. We demonstrated how its sensitivity and chemical selectivity can be increased and what additional spectroscopic information can be obtained using resonant, coherent and surface enhancements. Some of these techniques, such as DUV Raman spectroscopy, are still based on the spontaneous Raman scattering phenomenon, while others, such as CARS and SECARS, involve different physical principles. Nonetheless, these techniques can be efficiently combined to yield even greater improvements over spontaneous Raman spectroscopy. Moreover, some additional experimental procedures, such as wavefront shaping [164,165] can further improve the efficiency of Raman scattering and, therefore, Raman spectroscopy. At the same time the twisted light, namely the vortex beams, can be implemented to detect chirality of the molecules in addition to obtaining molecular Raman spectrum [166], thus opening a path towards the ultimate goal of achieving single-molecule sensitivity in Raman spectroscopy and potentially atomic-level resolution in imaging techniques based on it [167].

REFERENCES

1. Lord Rayleigh F.R.S, "XXXIV. On the transmission of light through an atmosphere containing small particles in suspension, and on the origin of the blue of the sky," The London, Edinburgh, and Dublin Philosophical Magazine and Journal of Science **47**, 375–384 (1899).
2. C. V. Raman, "The Colour of the Sea," Nature **108**, 367–367 (1921).
3. A. H. Compton, "A Quantum Theory of the Scattering of X-rays by Light Elements," Phys. Rev. **21**, 483–502 (1923).
4. C. V. Raman, "A new radiation," Indian Journal of Physics **2**, 387–398 (1928).
5. C. V. Raman and K. S. Krishnan, "The Optical Analogue of the Compton Effect," Nature **121**, 711–711 (1928).
6. C. V. Raman and K. S. Krishnan, "A New Type of Secondary Radiation," Nature **121**, 501–502 (1928).
7. Grigory Landsberg and Leonid Mandelstam, "Eine neue Erscheinung bei der Lichtzerstreuung in Krystallen," Naturwissenschaften **16**, 557–558 (1928).
8. I. L. Fabelinskiĭ, "The discovery of combination scattering of light in Russia and India," Phys.-Usp. **46**, 1105 (2003).
9. R. Singh and F. Riess, "The 1930 Nobel Prize for Physics: A close decision?," Notes and Records of the Royal Society of London **55**, 267–283 (2001).
10. S. P. S. Porto and D. L. Wood, "Ruby Optical Maser as a Raman Source," J. Opt. Soc. Am., JOSA **52**, 251–252 (1962).
11. F. Adar, M. Delhaye, and E. DaSilva, "Evolution of Instrumentation for Detection of the Raman Effect as Driven by Available Technologies and by Developing Applications," J. Chem. Educ. **84**, 50 (2007).
12. B. Chase, "Fourier Transform Raman Spectroscopy," Anal. Chem. **59**, 881A-889A (1987).
13. D. P. Strommen and K. Nakamoto, "Resonance raman spectroscopy," J. Chem. Educ. **54**, 474 (1977).
14. D. L. Jeanmaire and R. P. Van Duyne, "Surface raman spectroelectrochemistry: Part I. Heterocyclic, aromatic, and aliphatic amines adsorbed on the anodized silver electrode," Journal of Electroanalytical Chemistry and Interfacial Electrochemistry **84**, 1–20 (1977).
15. M. Fleischmann, P. J. Hendra, and A. J. McQuillan, "Raman spectra of pyridine adsorbed at a silver electrode," Chemical Physics Letters **26**, 163–166 (1974).
16. P. D. Maker and R. W. Terhune, "Study of Optical Effects Due to an Induced Polarization Third Order in the Electric Field Strength," Phys. Rev. **137**, A801–A818 (1965).
17. R. F. Begley, A. B. Harvey, and R. L. Byer, "Coherent anti-Stokes Raman spectroscopy," Appl. Phys. Lett. **25**, 387–390 (1974).
18. Derek A. Long, *The Raman Effect: A Unified Treatment of the Theory of Raman Scattering by Molecules* (John Wiley & Sons, Ltd, 2002).
19. D. J. Griffiths, *Introduction to Electrodynamics* (Cambridge University Press, 2017).

20. A. C. Albrecht and M. C. Hutley, "On the Dependence of Vibrational Raman Intensity on the Wavelength of Incident Light," J. Chem. Phys. **55**, 4438–4443 (1971).
21. J. Tang and A. C. Albrecht, "Developments in the Theories of Vibrational Raman Intensities," in *Raman Spectroscopy: Theory and Practice*, H. A. Szymanski, ed. (Springer US, 1970), pp. 33–68.
22. H. Inaba, "Detection of atoms and molecules by Raman scattering and resonance fluorescence," in *Laser Monitoring of the Atmosphere*, E. D. Hinkley, ed., Topics in Applied Physics (Springer, 1976), pp. 153–236.
23. A. Weber, ed., *Raman Spectroscopy of Gases and Liquids*, Topics in Current Physics (Springer Berlin Heidelberg, 1979), Vol. 11.
24. W. Heitler, *The Quantum Theory of Radiation* (Dover Publications, 1954).
25. H. Szymanski, *Raman Spectroscopy: Theory and Practice* (Springer Science & Business Media, 2013).
26. T. N. Olney, N. M. Cann, G. Cooper, and C. E. Brion, "Absolute scale determination for photoabsorption spectra and the calculation of molecular properties using dipole sum-rules," Chemical Physics **223**, 59–98 (1997).
27. E. Smith and G. Dent, *Modern Raman Spectroscopy: A Practical Approach* (John Wiley & Sons, 2019).
28. G. A. Worth and L. S. Cederbaum, "BEYOND BORN-OPPENHEIMER: Molecular Dynamics Through a Conical Intersection," Annual Review of Physical Chemistry **55**, 127–158 (2004).
29. D. L. Rousseau, J. M. Friedman, and P. F. Williams, "The Resonance Raman Effect," in *Raman Spectroscopy of Gases and Liquids*, A. Weber, ed., Topics in Current Physics (Springer, 1979), pp. 203–252.
30. J. A. Koningstein, "Theory of Raman scattering for overtone and combination bands in the vibrational Raman effect," Journal of Molecular Spectroscopy **28**, 309–315 (1968).
31. J. Franck and E. G. Dymond, "Elementary processes of photochemical reactions," Trans. Faraday Soc. **21**, 536–542 (1926).
32. E. Condon, "A Theory of Intensity Distribution in Band Systems," Phys. Rev. **28**, 1182–1201 (1926).
33. A. C. Albrecht, "On the Theory of Raman Intensities," J. Chem. Phys. **34**, 1476–1484 (1961).
34. P. Meystre and M. Sargent, "Resonance Fluorescence," in *Elements of Quantum Optics*, P. Meystre and M. Sargent, eds. (Springer, 1990), pp. 395–424.
35. C. F. Shaw, "Resonance fluorescence and resonance Raman spectroscopy of bromine and iodine vapor," J. Chem. Educ. **58**, 343 (1981).
36. A. D. Shutov, G. V. Petrov, D.-W. Wang, M. O. Scully, and V. V. Yakovlev, "Highly efficient tunable picosecond deep ultraviolet laser system for Raman spectroscopy," Optics letters **44**, 5760–5763 (2019).
37. J. N. Bixler, M. T. Cone, B. H. Hokr, J. D. Mason, E. Figueroa, E. S. Fry, V. V. Yakovlev, and M. O. Scully, "Ultrasensitive detection of waste products in water

using fluorescence emission cavity-enhanced spectroscopy," PNAS **111**, 7208–7211 (2014).
38. J. V. Thompson, B. H. Hokr, W. Kim, C. W. Ballmann, B. E. Applegate, J. Jo, A. Yamilov, H. Cao, M. O. Scully, and V. V. Yakovlev, "Enhanced coupling of light into a turbid medium through microscopic interface engineering," PNAS **114**, 7941–7946 (2017).
39. J. V. Thompson, B. H. Hokr, W. Kim, C. W. Ballmann, B. E. Applegate, J. A. Jo, A. Yamilov, H. Cao, M. O. Scully, and V. V. Yakovlev, "Enhanced optical coupling and Raman scattering via microscopic interface engineering," Appl. Phys. Lett. **111**, 201105 (2017).
40. K. Kneipp, H. Kneipp, I. Itzkan, R. R. Dasari, and M. S. Feld, "Ultrasensitive Chemical Analysis by Raman Spectroscopy," Chemical Reviews **99**, 2957–2976 (1999).
41. C. W. Freudiger, W. Min, B. G. Saar, S. Lu, G. R. Holtom, C. He, J. C. Tsai, J. X. Kang, and X. S. Xie, "Label-Free Biomedical Imaging with High Sensitivity by Stimulated Raman Scattering Microscopy," Science **322**, 1857–1861 (2008).
42. G. I. Petrov, R. Arora, V. V. Yakovlev, X. Wang, A. V. Sokolov, and M. O. Scully, "Comparison of coherent and spontaneous Raman microspectroscopies for noninvasive detection of single bacterial endospores," PNAS **104**, 7776–7779 (2007).
43. A. D. Shutov, Z. Yi, J. Wang, A. M. Sinyukov, Z. He, C. Tang, J. Chen, E. J. Ocola, J. Laane, A. V. Sokolov, D. V. Voronine, and M. O. Scully, "Giant Chemical Surface Enhancement of Coherent Raman Scattering on MoS2," ACS Photonics **5**, 4960–4968 (2018).
44. W. F. Howard, W. H. Nelson, and J. F. Sperry, "A Resonance Raman Method for the Rapid Detection and Identification of Bacteria in Water," Appl. Spectrosc., AS **34**, 72–75 (1980).
45. S. A. Asher and C. R. Johnson, "Raman spectroscopy of a coal liquid shows that fluorescence interference is minimized with ultraviolet excitation," Science **225**, 311–313 (1984).
46. S. A. Oladepo, K. Xiong, Z. Hong, S. A. Asher, J. Handen, and I. K. Lednev, "UV Resonance Raman Investigations of Peptide and Protein Structure and Dynamics," Chem. Rev. **112**, 2604–2628 (2012).
47. I. K. Lednev, V. V. Ermolenkov, W. He, and M. Xu, "Deep-UV Raman spectrometer tunable between 193 and 205 nm for structural characterization of proteins," Anal Bioanal Chem **381**, 431–437 (2005).
48. M. Wu, M. Ray, K. H. Fung, M. W. Ruckman, D. Harder, and A. J. Sedlacek, "Stand-off Detection of Chemicals by UV Raman Spectroscopy," Appl. Spectrosc., AS **54**, 800–806 (2000).
49. C. R. Philbrick and K. R. Mulik, "Application of Raman lidar to air quality measurements," in *Laser Radar Technology and Applications V* (International Society for Optics and Photonics, 2000), Vol. 4035, pp. 22–34.
50. A. Willitsford, C. T. Chadwick, H. Hallen, and C. R. Philbrick, "Resonance Raman measurements utilizing a deep UV source," in *Laser Radar Technology and*

Applications XIII (International Society for Optics and Photonics, 2008), Vol. 6950, p. 69500A.
51. C. M. Jones, V. L. Devito, P. A. Harmon, and S. A. Asher, "High-Repetition-Rate Excimer-Based UV Laser Excitation Source Avoids Saturation in Resonance Raman Measurements of Tyrosinate and Pyrene," Appl. Spectrosc., AS **41**, 1268–1275 (1987).
52. G. Balakrishnan, Y. Hu, S. B. Nielsen, and T. G. Spiro, "Tunable kHz Deep Ultraviolet (193–210 nm) Laser for Raman Applications," Appl Spectrosc **59**, 776–781 (2005).
53. M. A. Troyanova-Wood, G. I. Petrov, and V. V. Yakovlev, "Simple and inexpensive instrument for deep-UV Raman spectroscopy," Journal of Raman Spectroscopy **44**, 1789–1791 (2013).
54. S. A. Asher, R. W. Bormett, X. G. Chen, D. H. Lemmon, N. Cho, P. Peterson, M. Arrigoni, L. Spinelli, and J. Cannon, "UV Resonance Raman Spectroscopy Using a New cw Laser Source: Convenience and Experimental Simplicity," Appl. Spectrosc., AS **47**, 628–633 (1993).
55. S. Bykov, I. Lednev, A. Ianoul, A. Mikhonin, C. Munro, and S. A. Asher, "Steady-State and Transient Ultraviolet Resonance Raman Spectrometer for the 193–270 nm Spectral Region," Appl. Spectrosc., AS **59**, 1541–1552 (2005).
56. A. T. Case, D. Tan, R. E. Stickel, and J. Mastromarino, "Narrow-linewidth, tunable ultraviolet, Ti:sapphire laser for environmental sensing," Appl. Opt., AO **45**, 2306–2309 (2006).
57. C. W. Ballmann, G. I. Petrov, and V. V. Yakovlev, "Simple approach to high-fidelity tunable narrow-band pulse generation," Opt. Lett., OL **42**, 89–92 (2017).
58. Z. Sun, M. Ghotbi, and M. Ebrahim-Zadeh, "Widely tunable picosecond optical parametric generation and amplification in BiB_3O_6," Opt. Express, OE **15**, 4139–4148 (2007).
59. A. D. Shutov, D. Pestov, N. Altangerel, Z. Yi, X. Wang, A. V. Sokolov, and M. O. Scully, "Collinear FAST CARS for Chemical Mapping of Gases," Applied Sciences **7**, 705 (2017).
60. M. D. Hargreaves and P. Matousek, "Threat detection of liquid explosive precursor mixtures by Spatially Offset Raman Spectroscopy (SORS)," in *Optics and Photonics for Counterterrorism and Crime Fighting V* (International Society for Optics and Photonics, 2009), Vol. 7486, p. 74860B.
61. S. Li, C. Jiang, H. Wang, S. Cong, and M. Tan, "Fluorescent nanoparticles present in Coca-Cola and Pepsi-Cola: physiochemical properties, cytotoxicity, biodistribution and digestion studies," Nanotoxicology **12**, 49–62 (2018).
62. E. V. Efremov, F. Ariese, A. J. G. Mank, and C. Gooijer, "Strong Overtones and Combination Bands in Ultraviolet Resonance Raman Spectroscopy," Anal. Chem. **78**, 3152–3157 (2006).
63. P. G. Zverev, T. T. Basiev, A. A. Sobol, V. V. Skornyakov, L. I. Ivleva, N. M. Polozkov, and V. V. Osiko, "Stimulated Raman scattering in alkaline-earth tungstate crystals," Quantum Electron. **30**, 55 (2000).

64. M. Frank, S. N. Smetanin, M. Jelínek, D. Vyhlídal, V. E. Shukshin, L. I. Ivleva, E. E. Dunaeva, I. S. Voronina, P. G. Zverev, and V. Kubeček, "Stimulated Raman Scattering in Alkali-Earth Tungstate and Molybdate Crystals at Both Stretching and Bending Raman Modes under Synchronous Picosecond Pumping with Multiple Pulse Shortening Down to 1 ps," Crystals **9**, 167 (2019).
65. D. D. Tuschel, A. V. Mikhonin, B. E. Lemoff, and S. A. Asher, "Deep Ultraviolet Resonance Raman Excitation Enables Explosives Detection," Appl Spectrosc **64**, 425–432 (2010).
66. M. Ghosh, L. Wang, and S. A. Asher, "Deep-Ultraviolet Resonance Raman Excitation Profiles of NH_4NO_3, PETN, TNT, HMX, and RDX," Appl Spectrosc **66**, 1013–1021 (2012).
67. Z. Iqbal, "Raman scattering study of the low temperature phase transitions in ammonium nitrate," Chemical Physics Letters **40**, 41–44 (1976).
68. P. Somerharju, "Pyrene-labeled lipids as tools in membrane biophysics and cell biology," Chemistry and Physics of Lipids **116**, 57–74 (2002).
69. H. Shinohara, Y. Yamakita, and K. Ohno, "Raman spectra of polycyclic aromatic hydrocarbons. Comparison of calculated Raman intensity distributions with observed spectra for naphthalene, anthracene, pyrene, and perylene," Journal of Molecular Structure **442**, 221–234 (1998).
70. J. Bendtsen, "The rotational and rotation-vibrational Raman spectra of 14N2, 14N15N and 15N2," Journal of Raman Spectroscopy **2**, 133–145 (1974).
71. W. H. Fletcher and J. S. Rayside, "High resolution vibrational Raman spectrum of oxygen," J. Raman Spectrosc. **2**, 3–14 (1974).
72. A. Dogariu, A. Goltsov, D. Pestov, A. V. Sokolov, and M. O. Scully, "Real-time detection of bacterial spores using coherent anti-Stokes Raman spectroscopy," Journal of Applied Physics **103**, 036103 (2008).
73. B. F. Webber, M. B. Long, and R. K. Chang, "Two-dimensional average concentration measurements in a jet flow by Raman scattering," Applied Physics Letters **35**, 119–121 (1979).
74. P. R. Regnier, F. Moya, and J. P. E. Taran, "Gas Concentration Measurement by Coherent Raman Anti-Stokes Scattering," AIAA Journal **12**, 826–831 (1974).
75. D. R. Richardson, R. P. Lucht, W. D. Kulatilaka, S. Roy, and J. R. Gord, "Chirped-probe-pulse femtosecond coherent anti-Stokes Raman scattering concentration measurements," JOSA B **30**, 188–196 (2013).
76. A. Dogariu, A. Goltsov, H. Xia, and M. O. Scully, "Concentration dependence in coherent Raman scattering," Journal of Modern Optics **55**, 3255–3261 (2008).
77. M. Zhi, D. Pestov, X. Wang, R. K. Murawski, Y. V. Rostovtsev, Z. E. Sariyanni, V. A. Sautenkov, N. G. Kalugin, and A. V. Sokolov, "Concentration dependence of femtosecond coherent anti-Stokes Raman scattering in the presence of strong absorption," JOSA B **24**, 1181–1186 (2007).
78. J. W. Nibler and G. V. Knighten, "Coherent Anti-Stokes Raman Spectroscopy," in *Raman Spectroscopy of Gases and Liquids*, P. D. A. Weber, ed., Topics in Current Physics No. 11 (Springer Berlin Heidelberg, 1979), pp. 253–299.

79. S. Roy, J. R. Gord, and A. K. Patnaik, "Recent advances in coherent anti-Stokes Raman scattering spectroscopy: Fundamental developments and applications in reacting flows," Progress in Energy and Combustion Science **36**, 280–306 (2010).
80. S. Roy, W. D. Kulatilaka, D. R. Richardson, R. P. Lucht, and J. R. Gord, "Gas-phase single-shot thermometry at 1 kHz using fs-CARS spectroscopy," Optics letters **34**, 3857–3859 (2009).
81. T. A. Reichardt, P. E. Schrader, and R. L. Farrow, "Comparison of gas temperatures measured by coherent anti-Stokes Raman spectroscopy (CARS) of O_2 and N_2," Appl. Opt., AO **40**, 741–747 (2001).
82. G. Matthäus, S. Demmler, M. Lebugle, F. Küster, J. Limpert, A. Tünnermann, S. Nolte, and R. Ackermann, "Ultra-broadband two beam CARS using femtosecond laser pulses," Vibrational Spectroscopy **85**, 128–133 (2016).
83. M. Kerstan, I. Makos, S. Nolte, A. Tünnermann, and R. Ackermann, "Two-beam femtosecond coherent anti-Stokes Raman scattering for thermometry on CO2," Applied Physics Letters **110**, 021116 (2017).
84. C. E. Dedic, J. D. Miller, and T. R. Meyer, "Dual-pump vibrational/rotational femtosecond/picosecond coherent anti-Stokes Raman scattering temperature and species measurements," Opt. Lett., OL **39**, 6608–6611 (2014).
85. A. Braeuer, F. Beyrau, M. C. Weikl, T. Seeger, J. Kiefer, A. Leipertz, A. Holzwarth, and A. Soika, "Investigation of the combustion process in an auxiliary heating system using dual-pump CARS," Journal of Raman Spectroscopy **37**, 633–640 (2006).
86. J. W. Tröger, C. Meißner, and T. Seeger, "High temperature O2 vibrational CARS thermometry applied to a turbulent oxy-fuel combustion process: O2 vibrational CARS thermometry for oxy-fuel combustion process," Journal of Raman Spectroscopy **47**, 1149–1156 (2016).
87. W. D. Kulatilaka, H. U. Stauffer, J. R. Gord, and S. Roy, "One-dimensional single-shot thermometry in flames using femtosecond-CARS line imaging," Optics letters **36**, 4182–4184 (2011).
88. A. Bohlin and C. J. Kliewer, "Direct Coherent Raman Temperature Imaging and Wideband Chemical Detection in a Hydrocarbon Flat Flame," J. Phys. Chem. Lett. **6**, 643–649 (2015).
89. A. Bohlin and C. J. Kliewer, "Single-shot hyperspectral coherent Raman planar imaging in the range 0–4200 cm^{-1}," Applied Physics Letters **105**, 161111 (2014).
90. W. B. Roh and P. W. Schreiber, "Pressure dependence of integrated CARS power," Appl. Opt., AO **17**, 1418–1424 (1978).
91. S. Roy, T. R. Meyer, and J. R. Gord, "Time-resolved dynamics of resonant and nonresonant broadband picosecond coherent anti-Stokes Raman scattering signals," Appl. Phys. Lett. **87**, 264103 (2005).
92. X. Wang, A. Zhang, M. Zhi, A. V. Sokolov, and G. R. Welch, "Glucose concentration measured by the hybrid coherent anti-Stokes Raman-scattering technique," Phys. Rev. A **81**, 013813 (2010).

93. G. Millot, R. Saint-Loup, J. Santos, R. Chaux, H. Berger, and J. Bonamy, "Collisional effects in the stimulated Raman Q branch of O2 and O2–N2," The Journal of Chemical Physics **96**, 961–971 (1992).
94. J. D. Miller, S. Roy, J. R. Gord, and T. R. Meyer, "Communication: Time-domain measurement of high-pressure N2 and O2 self-broadened linewidths using hybrid femtosecond/picosecond coherent anti-Stokes Raman scattering," The Journal of Chemical Physics **135**, 201104 (2011).
95. M. O. Scully, G. W. Kattawar, R. P. Lucht, T. Opatrný, H. Pilloff, A. Rebane, A. V. Sokolov, and M. S. Zubairy, "FAST CARS: Engineering a laser spectroscopic technique for rapid identification of bacterial spores," PNAS **99**, 10994–11001 (2002).
96. B. D. Prince, A. Chakraborty, B. M. Prince, and H. U. Stauffer, "Development of simultaneous frequency- and time-resolved coherent anti-Stokes Raman scattering for ultrafast detection of molecular Raman spectra," J Chem Phys **125**, 44502 (2006).
97. D. Pestov, R. K. Murawski, G. O. Ariunbold, X. Wang, M. Zhi, A. V. Sokolov, V. A. Sautenkov, Y. V. Rostovtsev, A. Dogariu, Y. Huang, and M. O. Scully, "Optimizing the Laser-Pulse Configuration for Coherent Raman Spectroscopy," Science **316**, 265–268 (2007).
98. Y. Shen, D. V. Voronine, A. V. Sokolov, and M. O. Scully, "A versatile setup using femtosecond adaptive spectroscopic techniques for coherent anti-Stokes Raman scattering," Rev Sci Instrum **86**, 083107 (2015).
99. Y. Shen, D. V. Voronine, A. V. Sokolov, and M. O. Scully, "Single-beam heterodyne FAST CARS microscopy," Opt. Express, OE **24**, 21652–21662 (2016).
100. D. V. Voronine, A. M. Sinyukov, X. Hua, K. Wang, P. K. Jha, E. Munusamy, S. E. Wheeler, G. Welch, A. V. Sokolov, and M. O. Scully, "Time-Resolved Surface-Enhanced Coherent Sensing of Nanoscale Molecular Complexes," Scientific Reports **2**, 891 (2012).
101. C. W. Ballmann, B. Cao, A. M. Sinyukov, A. V. Sokolov, and D. V. Voronine, "Dual-tip-enhanced ultrafast CARS nanoscopy," New Journal of Physics **16**, 083004 (2014).
102. X. Hua, D. V. Voronine, C. W. Ballmann, A. M. Sinyukov, A. V. Sokolov, and M. O. Scully, "Nature of surface-enhanced coherent Raman scattering," Phys. Rev. A **89**, 043841 (2014).
103. F. Beyrau, T. Seeger, A. Malarski, and A. Leipertz, "Determination of temperatures and fuel/air ratios in an ethene–air flame by dual-pump CARS," J. Raman Spectrosc. **34**, 946–951 (2003).
104. S. R. Engel, J. D. Miller, C. E. Dedic, T. Seeger, A. Leipertz, and T. R. Meyer, "Hybrid femtosecond/picosecond coherent anti-Stokes Raman scattering for high-speed CH4/N2 measurements in binary gas mixtures: Hybrid fs/ps CARS for high-speed CH4/N2 measurements," Journal of Raman Spectroscopy **44**, 1336–1343 (2013).

105. P. R. Hemmer, R. B. Miles, P. Polynkin, T. Siebert, A. V. Sokolov, P. Sprangle, and M. O. Scully, "Standoff spectroscopy via remote generation of a backward-propagating laser beam," PNAS **108**, 3130–3134 (2011).
106. J. Nestor, T. G. Spiro, and G. Klauminzer, "Coherent anti-Stokes Raman scattering (CARS) spectra, with resonance enhancement, of cytochrome c and vitamin B12 in dilute aqueous solution.," Proc Natl Acad Sci U S A **73**, 3329–3332 (1976).
107. K. Kneipp, M. Moskovits, and H. Kneipp, *Surface-Enhanced Raman Scattering: Physics and Applications* (Springer Science & Business Media, 2006).
108. B. Sharma, R. R. Frontiera, A.-I. Henry, E. Ringe, and R. P. Van Duyne, "SERS: Materials, applications, and the future," Materials Today **15**, 16–25 (2012).
109. J. Langer, D. Jimenez de Aberasturi, J. Aizpurua, R. A. Alvarez-Puebla, B. Auguié, J. J. Baumberg, G. C. Bazan, S. E. J. Bell, A. Boisen, A. G. Brolo, J. Choo, D. Cialla-May, V. Deckert, L. Fabris, K. Faulds, F. J. García de Abajo, R. Goodacre, D. Graham, A. J. Haes, C. L. Haynes, C. Huck, T. Itoh, M. Käll, J. Kneipp, N. A. Kotov, H. Kuang, E. C. Le Ru, H. K. Lee, J.-F. Li, X. Y. Ling, S. A. Maier, T. Mayerhöfer, M. Moskovits, K. Murakoshi, J.-M. Nam, S. Nie, Y. Ozaki, I. Pastoriza-Santos, J. Perez-Juste, J. Popp, A. Pucci, S. Reich, B. Ren, G. C. Schatz, T. Shegai, S. Schlücker, L.-L. Tay, K. G. Thomas, Z.-Q. Tian, R. P. Van Duyne, T. Vo-Dinh, Y. Wang, K. A. Willets, C. Xu, H. Xu, Y. Xu, Y. S. Yamamoto, B. Zhao, and L. M. Liz-Marzán, "Present and Future of Surface-Enhanced Raman Scattering," ACS Nano **14**, 28–117 (2020).
110. K. Kneipp, Y. Wang, H. Kneipp, L. T. Perelman, I. Itzkan, R. R. Dasari, and M. S. Feld, "Single Molecule Detection Using Surface-Enhanced Raman Scattering (SERS)," Phys. Rev. Lett. **78**, 1667–1670 (1997).
111. E. C. Le Ru and P. G. Etchegoin, "Single-molecule surface-enhanced Raman spectroscopy," Annu Rev Phys Chem **63**, 65–87 (2012).
112. Jiang, K. Bosnick, M. Maillard, and L. Brus, "Single Molecule Raman Spectroscopy at the Junctions of Large Ag Nanocrystals," J. Phys. Chem. B **107**, 9964–9972 (2003).
113. J. Grand, M. L. de la Chapelle, J.-L. Bijeon, P.-M. Adam, A. Vial, and P. Royer, "Role of localized surface plasmons in surface-enhanced Raman scattering of shape-controlled metallic particles in regular arrays," Phys. Rev. B **72**, 033407 (2005).
114. S.-Y. Ding, E.-M. You, Z.-Q. Tian, and M. Moskovits, "Electromagnetic theories of surface-enhanced Raman spectroscopy," Chemical Society Reviews **46**, 4042–4076 (2017).
115. M. Moskovits, "Surface roughness and the enhanced intensity of Raman scattering by molecules adsorbed on metals," The Journal of Chemical Physics **69**, 4159–4161 (1978).
116. D. A. Clayton, T. E. McPherson, S. Pan, M. Chen, D. A. Dixon, and D. Hu, "Spatial and temporal variation of surface-enhanced Raman scattering at Ag nanowires in aqueous solution," Phys Chem Phys **15**, 850–859 (2013).

117. E. C. Le Ru, P. G. Etchegoin, and M. Meyer, "Enhancement factor distribution around a single surface-enhanced Raman scattering hot spot and its relation to single molecule detection," The Journal of Chemical Physics **125**, 204701 (2006).
118. S. L. Kleinman, B. Sharma, M. G. Blaber, A.-I. Henry, N. Valley, R. G. Freeman, M. J. Natan, G. C. Schatz, and R. P. Van Duyne, "Structure Enhancement Factor Relationships in Single Gold Nanoantennas by Surface-Enhanced Raman Excitation Spectroscopy," J. Am. Chem. Soc. **135**, 301–308 (2013).
119. M. Sinwani, M. Muallem, and Y. R. Tischler, "The effect of excitation wavelength and metallic nanostructure on SERS spectra of C60," J. Raman Spectrosc. **48**, 829–836 (2017).
120. J. Ye, J. A. Hutchison, H. Uji-i, J. Hofkens, L. Lagae, G. Maes, G. Borghs, and P. Van Dorpe, "Excitation wavelength dependent surface enhanced Raman scattering of 4-aminothiophenol on gold nanorings," Nanoscale **4**, 1606–1611 (2012).
121. A. D. McFarland, M. A. Young, J. A. Dieringer, and R. P. Van Duyne, "Wavelength-Scanned Surface-Enhanced Raman Excitation Spectroscopy," J. Phys. Chem. B **109**, 11279–11285 (2005).
122. F. J. Adrian, "Charge transfer effects in surface-enhanced Raman scattering," The Journal of Chemical Physics **77**, 5302–5314 (1982).
123. A. Otto, "The 'chemical' (electronic) contribution to surface-enhanced Raman scattering," J. Raman Spectrosc. **36**, 497–509 (2005).
124. J. A. Parkhill, D. Rappoport, and A. Aspuru-Guzik, "Modeling Coherent Anti-Stokes Raman Scattering with Time-Dependent Density Functional Theory: Vacuum and Surface Enhancement.," J. Phys. Chem. Lett. **2**, 1849–1854 (2011).
125. H. Yamada and Y. Yamamoto, "Surface enhanced Raman scattering (SERS) of chemisorbed species on various kinds of metals and semiconductors," Surface Science **134**, 71–90 (1983).
126. I. Alessandri and J. R. Lombardi, "Enhanced Raman Scattering with Dielectrics," Chem. Rev. **116**, 14921–14981 (2016).
127. Z. Zheng, S. Cong, W. Gong, J. Xuan, G. Li, W. Lu, F. Geng, and Z. Zhao, "Semiconductor SERS enhancement enabled by oxygen incorporation," Nature Communications **8**, 1993 (2017).
128. R. Livingstone, X. Zhou, M. C. Tamargo, J. R. Lombardi, L. G. Quagliano, and F. Jean-Mary, "Surface Enhanced Raman Spectroscopy of Pyridine on CdSe/ZnBeSe Quantum Dots Grown by Molecular Beam Epitaxy," J. Phys. Chem. C **114**, 17460–17464 (2010).
129. D. Maznichenko, K. Venkatakrishnan, and B. Tan, "Stimulating Multiple SERS Mechanisms by a Nanofibrous Three-Dimensional Network Structure of Titanium Dioxide (TiO2)," J. Phys. Chem. C **117**, 578–583 (2013).
130. W. Xu, X. Ling, J. Xiao, M. S. Dresselhaus, J. Kong, H. Xu, Z. Liu, and J. Zhang, "Surface enhanced Raman spectroscopy on a flat graphene surface," PNAS **109**, 9281–9286 (2012).
131. D. Zhang, Y.-C. Wu, M. Yang, X. Liu, C. Ó. Coileáin, M. Abid, M. Abid, J.-J. Wang, I. Shvets, H. Xu, B. S. Chun, H. Liu, and H.-C. Wu, "Surface enhanced

Raman scattering of monolayer MX_2 with metallic nano particles," Scientific Reports **6**, 30320 (2016).
132. X. Ling, L. Xie, Y. Fang, H. Xu, H. Zhang, J. Kong, M. S. Dresselhaus, J. Zhang, and Z. Liu, "Can Graphene be used as a Substrate for Raman Enhancement?," Nano Lett. **10**, 553–561 (2010).
133. S. Huang, X. Ling, L. Liang, Y. Song, W. Fang, J. Zhang, J. Kong, V. Meunier, and M. S. Dresselhaus, "Molecular Selectivity of Graphene-Enhanced Raman Scattering," Nano Lett. **15**, 2892–2901 (2015).
134. N. Zhang, L. Tong, and J. Zhang, "Graphene-Based Enhanced Raman Scattering toward Analytical Applications," Chem. Mater. **28**, 6426–6435 (2016).
135. X. Ling, W. Fang, Y.-H. Lee, P. T. Araujo, X. Zhang, J. F. Rodriguez-Nieva, Y. Lin, J. Zhang, J. Kong, and M. S. Dresselhaus, "Raman Enhancement Effect on Two-Dimensional Layered Materials: Graphene, h-BN and MoS2," Nano Lett. **14**, 3033–3040 (2014).
136. Y. Lee, H. Kim, J. Lee, S. H. Yu, E. Hwang, C. Lee, J.-H. Ahn, and J. H. Cho, "Enhanced Raman Scattering of Rhodamine 6G Films on Two-Dimensional Transition Metal Dichalcogenides Correlated to Photoinduced Charge Transfer," Chem. Mater. **28**, 180–187 (2016).
137. C. Muehlethaler, C. R. Considine, V. Menon, W.-C. Lin, Y.-H. Lee, and J. R. Lombardi, "Ultrahigh Raman Enhancement on Monolayer MoS2," ACS Photonics **3**, 1164–1169 (2016).
138. K. F. Mak, C. Lee, J. Hone, J. Shan, and T. F. Heinz, "Atomically Thin MoS2: A New Direct-Gap Semiconductor," Phys. Rev. Lett. **105**, 136805 (2010).
139. M. Bernardi, M. Palummo, and J. C. Grossman, "Extraordinary Sunlight Absorption and One Nanometer Thick Photovoltaics Using Two-Dimensional Monolayer Materials," Nano Lett. **13**, 3664–3670 (2013).
140. A. Splendiani, L. Sun, Y. Zhang, T. Li, J. Kim, C.-Y. Chim, G. Galli, and F. Wang, "Emerging Photoluminescence in Monolayer MoS2," Nano Lett. **10**, 1271–1275 (2010).
141. D. V. Voronine, Z. Zhang, A. V. Sokolov, and M. O. Scully, "Surface-enhanced FAST CARS: en route to quantum nano-biophotonics," Nanophotonics **7**, 523–548 (2018).
142. D. Pestov, G. O. Ariunbold, X. Wang, R. K. Murawski, V. A. Sautenkov, A. V. Sokolov, and M. O. Scully, "Coherent versus incoherent Raman scattering: molecular coherence excitation and measurement," Opt. Lett., OL **32**, 1725–1727 (2007).
143. C. Steuwe, C. F. Kaminski, J. J. Baumberg, and S. Mahajan, "Surface Enhanced Coherent Anti-Stokes Raman Scattering on Nanostructured Gold Surfaces," Nano Lett. **11**, 5339–5343 (2011).
144. Y. Zhang, Y.-R. Zhen, O. Neumann, J. K. Day, P. Nordlander, and N. J. Halas, "Coherent anti-Stokes Raman scattering with single-molecule sensitivity using a plasmonic Fano resonance," Nature Communications **5**, 4424 (2014).

145. S. Yampolsky, D. A. Fishman, S. Dey, E. Hulkko, M. Banik, E. O. Potma, and V. A. Apkarian, "Seeing a single molecule vibrate through time-resolved coherent anti-Stokes Raman scattering," Nature Photonics **8**, 650–656 (2014).
146. Z. Yan, Z. Liu, M. Xia, A. Efimov, and Y.-H. Xie, "Broadband surface-enhanced coherent anti-Stokes Raman spectroscopy with high spectral resolution," Journal of Raman Spectroscopy **48**, 935–942 (2017).
147. D. V. Voronine, A. M. Sinyukov, X. Hua, E. Munusamy, G. Ariunbold, A. V. Sokolov, and M. O. Scully, "Complex line shapes in surface-enhanced coherent Raman spectroscopy," Journal of Modern Optics **62**, 90–96 (2015).
148. M. I. Cabaço, M. Besnard, and J. Yarwood, "Raman spectroscopic studies of vibrational relaxation and chemical exchange broadening in hydrogen bonded systems," Molecular Physics **75**, 157–172 (1992).
149. S. Schlücker, R. K. Singh, B. P. Asthana, J. Popp, and W. Kiefer, "Hydrogen-Bonded Pyridine−Water Complexes Studied by Density Functional Theory and Raman Spectroscopy," J. Phys. Chem. A **105**, 9983–9989 (2001).
150. M. Kreyenschmidt, H. H. Eysel, and B. P. Asthana, "Study of the pyridine–methanol system using four-channel Raman spectroscopy: Concentration dependence of frequencies, line widths and integrated intensities," J. Raman Spectrosc. **24**, 645–652 (1993).
151. V. Deckert, B. P. Asthana, P. C. Mishra, and W. Kiefer, "Dimer and Trimer in Pyridine–Ethanol Mixture Reinvestigated Applying the Scanning Multi-Channel Raman Difference Technique and AM1 Molecular Orbital Calculations," J. Raman Spectrosc. **27**, 907–913 (1996).
152. S. Schlücker, M. Heid, R. K. Singh, B. P. Asthana, J. Popp, and W. Kiefer, "Vibrational Dynamics in Hydrogen-Bonded (Pyridine + Water) Complexes Studied by Spectrally Resolved Femtosecond CARS," Zeitschrift für Physikalische Chemie **216**, 267 (2002).
153. A. G. Kalampounias, G. Tsilomelekis, and S. Boghosian, "Vibrational dephasing and frequency shifts of hydrogen-bonded pyridine–water complexes," Spectrochimica Acta Part A: Molecular and Biomolecular Spectroscopy **135**, 31–38 (2015).
154. H. U. Stauffer, J. D. Miller, M. N. Slipchenko, T. R. Meyer, B. D. Prince, S. Roy, and J. R. Gord, "Time- and frequency-dependent model of time-resolved coherent anti-Stokes Raman scattering (CARS) with a picosecond-duration probe pulse," The Journal of Chemical Physics **140**, 024316 (2014).
155. J. R. Lombardi, "The theory of surface-enhanced Raman scattering on semiconductor nanoparticles; toward the optimization of SERS sensors," Faraday Discussions **205**, 105–120 (2017).
156. P. Boopalachandran and J. Laane, "Ultraviolet absorption spectra of pyridine-d0 and -d5 and their ring-bending potential energy function in the S1(n,π∗) state," Chemical Physics Letters **462**, 178–182 (2008).
157. W. A. Schroeder, P. E. Wilcox, K. N. Trueblood, and A. O. Dekker, "Ultraviolet and Visible Absorption Spectra in Ethyl Alcohol," Anal. Chem. **23**, 1740–1747 (1951).

158. A. Castellanos-Gomez, J. Quereda, H. P. van der Meulen, N. Agraït, and G. Rubio-Bollinger, "Spatially resolved optical absorption spectroscopy of single- and few-layer MoS 2 by hyperspectral imaging," Nanotechnology **27**, 115705 (2016).
159. D. C. Arnett, P. Voehringer, and N. F. Scherer, "Excitation Dephasing, Product Formation, and Vibrational Coherence in an Intervalence Charge-Transfer Reaction," J. Am. Chem. Soc. **117**, 12262–12272 (1995).
160. M. I. Mallus, M. Schallwig, and U. Kleinekathöfer, "Relation between Vibrational Dephasing Time and Energy Gap Fluctuations," J. Phys. Chem. B **121**, 6471–6478 (2017).
161. A. E. Gainza, E. N. Rodríguez-Arias, and F. Ruette, "Pyridine adsorption on a MoS2 modelled surface (Mo3S8). A CNDO molecular orbital study," Journal of Molecular Catalysis **85**, 345–359 (1993).
162. B. Temel, A. K. Tuxen, J. Kibsgaard, N.-Y. Topsøe, B. Hinnemann, K. G. Knudsen, H. Topsøe, J. V. Lauritsen, and F. Besenbacher, "Atomic-scale insight into the origin of pyridine inhibition of MoS2-based hydrotreating catalysts," Journal of Catalysis **271**, 280–289 (2010).
163. D. Wang, Z. Wang, C. Wang, P. Zhou, Z. Wu, and Z. Liu, "Distorted MoS2 nanostructures: An efficient catalyst for the electrochemical hydrogen evolution reaction," Electrochemistry Communications **34**, 219–222 (2013).
164. M. Shutova, A. A. Zhdanova, and A. V. Sokolov, "Detection of mixed OAM states via vortex breakup," Physics Letters A **381**, 408–412 (2017).
165. M. Shutova, A. D. Shutov, A. A. Zhdanova, J. V. Thompson, and A. V. Sokolov, "Coherent Raman Generation Controlled by Wavefront Shaping," Scientific Reports (Nature Publisher Group) **9**, 1–8 (2019).
166. M. Shutova, A. D. Shutov, and A. V. Sokolov, "Spectroscopic sensing enhanced by quantum molecular coherence and by plasmonic nanoantennas," in *Optical, Opto-Atomic, and Entanglement-Enhanced Precision Metrology II* (International Society for Optics and Photonics, 2020), Vol. 11296, p. 1129605.
167. Y. Zhang, H. Hong, and W. Cai, "Imaging with Raman Spectroscopy," Curr Pharm Biotechnol **11**, 654–661 (2010).

APPENDIX A

DIPOLE RADIATION

As the dipole radiation plays a key role in description of the scattering phenomena, we will describe it here in more details. For instance, it will become clear why Raman (and Rayleigh) scattering depend on the fourth power of radiation frequency.

We start by following Griffiths [19] p. 443. Let us consider the dipole consisting of two equal and opposite charges fixed in position at $z = \pm d/2$, but with a time-dependent charge:

$$q(t) = q_0 \cos \omega t \, .$$

Then the dipole moment is

$$\vec{p}(t) = q_0 d\hat{z} \cos \omega t = \vec{p}_0 \cos \omega t \, ,$$

where $\hat{z}$ is the unit vector in the z-direction.

Now we are making following assumptions:

1. $d \ll r$. The source dimension is much less than the distance to the source.
2. $\omega d/c \ll 1$ or $d \ll \lambda$. The dipole length is much smaller that the wavelength, (the dipole oscillates slowly)
3. $\omega r/c \gg 1$ or $r \gg \lambda$. The distance from the source to the observed is much greater than the wavelength.

Then using expression for the retarded potential:

$$V(\vec{r}, t) = \frac{1}{4\pi\varepsilon_0} \int \frac{\rho(\vec{r}, t - R/c)}{R} d\tau' = \frac{q_0}{4\pi\varepsilon_0} \left(\frac{\cos \omega \, (t - R_+/c)}{R_+} - \frac{\cos \omega \, (t - R_-/c)}{R_-} \right),$$

where, using approximation 1, we have

$$R_{\pm} = \sqrt{r^2 + \frac{d^2}{4} \mp rd\cos\theta} \cong r\left(1 \mp \frac{d}{2r}\cos\theta\right)$$

$$V(\vec{r},t) = \frac{q_0}{4\pi\varepsilon_0 r}\left(\frac{\cos\omega\left[\omega t - \omega\frac{r}{c}\left(1 - \frac{d}{2r}\cos\theta\right)\right]}{1 - \frac{d}{2r}\cos\theta} - \frac{\cos\omega\left[\omega t - \omega\frac{r}{c}\left(1 + \frac{d}{2r}\cos\theta\right)\right]}{1 + \frac{d}{2r}\cos\theta}\right).$$

After that we apply the second approximation and expand the cosine to the first term in $\omega d/c$

$$\cos\omega\,(t - R_+/c) = \cos\omega\left(t - \frac{r}{c}\right)\cos\left(\frac{\omega d}{2c}\cos\theta\right) - \sin\omega\left(t - \frac{r}{c}\right)\sin\left(\frac{\omega d}{2c}\cos\theta\right)$$
$$\cong \cos\omega\left(t - \frac{r}{c}\right) - \frac{\omega d}{2c}\cos\theta\sin\omega\left(t - \frac{r}{c}\right).$$

Then

$$V(\vec{r},t) = \frac{q_0}{4\pi\varepsilon_0 r}\left(\frac{\cos\omega\left(t - \frac{r}{c}\right) - \frac{\omega d}{2c}\cos\theta\sin\omega\left(t - \frac{r}{c}\right)}{1 - \frac{d}{2r}\cos\theta} - \frac{\cos\omega\left(t - \frac{r}{c}\right) + \frac{\omega d}{2c}\cos\theta\sin\omega\left(t - \frac{r}{c}\right)}{1 + \frac{d}{2r}\cos\theta}\right)$$

$$= \frac{q_0}{4\pi\varepsilon_0 r}\left(\frac{\frac{d}{r}\cos\theta\sin\omega\left(t - \frac{r}{c}\right) - \frac{\omega d}{c}\cos\theta\sin\omega\left(t - \frac{r}{c}\right)}{1 - \left(\frac{d}{2r}\cos\theta\right)^2}\right)$$

$$= \frac{p_0}{4\pi\varepsilon_0 r}\left(\frac{1}{r}\cos\theta\sin\omega\left(t - \frac{r}{c}\right) - \frac{\omega}{c}\cos\theta\sin\omega\left(t - \frac{r}{c}\right)\right).$$

Finally, using approximation 3, we clearly see that the second term dominates, hence

$$V \simeq -\frac{p_0}{4\pi\varepsilon_0 r}\frac{\omega}{c}\cos\theta \sin\omega\left(t-\frac{r}{c}\right). \qquad (A.1)$$

The vector potential is then due to the current existing everywhere along the line between two charges

$$I(t) = \frac{dq}{dt} = -\omega q_0 \sin\omega t$$

Then, using the distance:

$$R(z') = \sqrt{r^2 + (z')^2 - 2rz'\cos\theta} \simeq r\left(1 - \frac{z'}{r}\cos\theta\right)$$

We find the vector potential:

$$\vec{A} = \frac{\mu_0}{4\pi}\int_{-\frac{d}{2}}^{+\frac{d}{2}} \frac{I(t_{ret})}{R}\,dz'$$

$$= -\frac{q_0}{4\pi}\int_{-\frac{d}{2}}^{+\frac{d}{2}} \frac{\omega \sin\omega\left(t-\frac{R}{c}\right)}{R}\,dz'$$

$$= -\frac{q_0}{4\pi}\frac{\omega}{r}\int_{-\frac{d}{2}}^{+\frac{d}{2}} \frac{\sin\omega\left(t-\frac{r}{c}+\frac{r'}{c}\cos\theta\right)}{1-\frac{r'}{c}\cos\theta}\,dz'$$

$$= -\frac{q_0}{4\pi}\frac{\omega}{r}\hat{z}\int_{-\frac{d}{2}}^{+\frac{d}{2}} \left[\sin\omega\left(t-\frac{r}{c}\right) + \omega\frac{z'}{c}\cos\theta\cos\omega\left(t-\frac{r}{c}\right)\right]\left(1+\frac{z'}{r}\cos\theta\right)dz'$$

$$= -\frac{q_0}{4\pi}\frac{\omega}{r}\hat{z}\int_{-\frac{d}{2}}^{+\frac{d}{2}} \left\{\sin\omega\left(t-\frac{r}{c}\right) + \frac{z'}{c}\cos\theta\left[\frac{\omega r}{c}\cos\omega\left(t-\frac{r}{c}\right)+1\right]\right\}dz'.$$

Which now can be easily integrated, while only the first term is nonzero:

$$\vec{A} \simeq -\frac{q_0}{4\pi}\frac{\omega d}{r}\hat{z}\sin\omega\left(t-\frac{r}{c}\right) = -\frac{q_0}{4\pi}\frac{\omega d}{r}\hat{z}\sin\omega\left(t-\frac{r}{c}\right). \qquad (A.2)$$

Now, using potentials from equations A.1 and A.2 we calculate fields:

$$\vec{E} = -\vec{\nabla}V - \frac{\partial\vec{A}}{\partial t}$$

$$= \vec{\nabla}\left[\frac{p_0}{r}\left(\frac{1}{r}\cos\theta\sin\omega\left(t-\frac{r}{c}\right) - \frac{\omega}{c}\cos\theta\sin\omega\left(t-\frac{r}{c}\right)\right)\right].$$

The first term in spherical coordinates:

$$\vec{\nabla}V = \frac{\partial V}{\partial r}\hat{r} + \frac{1}{r}\frac{\partial V}{\partial\theta}\hat{\theta}$$

$$\vec{\nabla}V = \frac{p_0}{4\pi\varepsilon_0}\frac{\omega}{c}\left\{\left[\frac{\cos\theta}{r^2}\sin\omega\left(t-\frac{r}{c}\right) + \frac{\omega}{c}\frac{\cos\theta}{r}\cos\omega\left(t-\frac{r}{c}\right)\right]\hat{r} + \frac{\hat{\theta}\sin\theta}{r^2}\omega\left(t-\frac{r}{c}\right)\right\}$$

$$\vec{\nabla}V \simeq \frac{p_0}{4\pi\varepsilon_0}\frac{\omega^2}{c^2}\frac{cos\theta}{r}\ cos\omega\left(t-\frac{r}{c}\right)\hat{r},$$

where high order terms in $c/\omega r$ were dropped.

$$\frac{\partial\vec{A}}{\partial t} = -\frac{\mu_0 p_0\omega^2}{4\pi}\hat{z}\cos\omega\left(t-\frac{r}{c}\right)$$

$$= -\frac{p_0\omega^2}{4\pi\varepsilon_0 rc^2}z.$$

Hence, the total electric field is

$$\vec{E} = -\frac{p_0}{4\pi\varepsilon_0 r}\frac{\omega^2}{c^2}\cos\omega\left(t-\frac{r}{c}\right)(\hat{r}\cos\theta - \hat{z}),$$

but

$$\hat{z} = \hat{r}\cos\theta - \hat{\theta}\sin\theta.$$

Thus,

$$\vec{E} = -\hat{\theta}\frac{p_0}{4\pi\varepsilon_0 r}\frac{\omega^2}{c^2} sin\theta \cos\omega\left(t - \frac{r}{c}\right). \qquad (A.3)$$

Then the magnetic field is

$$\vec{B} = \vec{\nabla} \times \vec{A} = -\vec{\nabla} \times \left(-\frac{q_0}{4\pi}\frac{\omega d}{r}\hat{z}\sin\omega\left(t - \frac{r}{c}\right)\right).$$

$\vec{A}$ has only r and θcomponents and each of them depends only on r and θ, so $\vec{B}$ has only a ϕ component:

$$\vec{B} = \frac{\hat{\phi}}{r}\left[\frac{\partial}{\partial r}(rA_\theta) - \frac{\partial A_r}{\partial\theta}\right]$$

$$= \frac{\mu_0 p_0 \omega}{4\pi r}\hat{\phi}\left[\frac{\partial}{\partial r}\left(sin\theta \sin\ \omega\left(t - \frac{r}{c}\right)\right) + \frac{1}{r}\frac{\partial \cos\theta \sin\omega\left(t - \frac{r}{c}\right)}{\partial\theta}\right]$$

$$= -\frac{\mu_0 p_0 \omega}{4\pi r}\hat{\phi}\left[\frac{\omega}{c} sin\theta \sin\ \omega\left(t - \frac{r}{c}\right) + \frac{1}{r} sin\theta \sin\ \omega\left(t - \frac{r}{c}\right)\right].$$

Again, the second term is much smaller than the first one, so we have

$$\vec{B} = -\frac{\mu_0 p_0 \omega^2}{4\pi r c}\hat{\phi}\sin\theta\cos\omega\left(t - \frac{r}{c}\right). \qquad (A.4)$$

Comparing expressions A.3 and A.4 we see that

$$\vec{B} = \frac{1}{c}\hat{r} \times \vec{E}.$$

as we expected for an EM wave.

From here we can calculate the Poynting vector:

$$\vec{S} = \frac{1}{\mu_0}\vec{E} \times \vec{B} = \frac{1}{\mu_0}\vec{E} \times \left(\frac{1}{c}\hat{r} \times \vec{E}\right)$$

$$= \frac{1}{\mu_0 c}\hat{r}E^2 = \frac{1}{\mu_0 c}\hat{r}\left(\frac{p_0}{4\pi\varepsilon_0 r}\right)^2 \frac{\omega^4}{c^4}\sin^2\theta\cos^2\omega\left(t - \frac{r}{c}\right).$$

Now, to get intensity we average over time and obtain:

$$\langle\vec{S}\rangle = I_{rad} = \hat{r}\frac{p_0^2}{32\pi^2\varepsilon_0 r^2}\frac{\omega^4}{c^3}\sin^2\theta\,. \qquad (A.5)$$

From here, it can be seen than the radiating intensity is proportional to the fourth power of the radiation frequency. Indeed, both Rayleigh and Raman scatterings are the processes involving the radiation of the induced dipole. While the magnitude of the induced dipole moment $\boldsymbol{p} = \boldsymbol{p_0}$ equals to the multiplication of molecular polarizability $\boldsymbol{\alpha}$ and the incident electric field $\boldsymbol{E}$. Hence, the intensity of scattered (*i.e.* radiated as in Equation A.5) light is proportional to the fourth power of the induced dipole frequency ω^4 as in equations 1.1 and 1.2. As we will from Appendix B, the more vigorous quantum mechanical description predicts although similar but slightly different result.

APPENDIX B

A THEORETICAL ESTIMATION OF RAMAN SCATTERING CROSS SECTION USING QUANTUM MECHANICS

As it was mentioned earlier, the classical theory of electromagnetic radiation cannot predict the intensities of Raman scattering. Hence, here we briefly analyze the Raman scattering by using quantum mechanical approach. We will apply the second order perturbation theory [25] to get a theoretical order of magnitude estimation for Raman scattering cross section values.

We study the system which is defined as following: light of photon with frequency $\omega_0 = 2\pi\nu_0$ incident on an isolated, freely rotating, molecule. The molecule undergoes a transition from the molecular eigenstate Ψ_n of energy E_n to eigenstate Ψ_m of energy E_m. The incident light is scattered to frequency ω_f (for elastic scattering $m = n$ and $\omega_f = \omega_0$). Then by the energy conservation we have:

$$E_m - E_n = \hbar(\omega_0 - \omega_f).(\omega_0 - \omega_f)\,.$$

We continue by writing the nonrelativistic Hamiltonian for a molecule interacting with an external radiation field:

$$H = H^0 + H'$$

Where the zeroth order Hamiltonian H^0 describes the unperturbed system of molecule plus radiation field:

$$H^0 = H_{mol} + H_{rad},$$

and H' describes the interaction of the two.

The molecular Hamiltonian is written in the usual form

$$H_{mol} = T_E + T_N + V, \qquad (B.1)$$

where T_E and T_N represent the electronic and nuclear kinetic energies, respectively, while V describes the potential energy for electron-electron, electron-nuclear, nuclear-nuclear interactions. The coordinate space is described by the coordinates $\boldsymbol{r}$ and $\boldsymbol{Q}$, where $\boldsymbol{r} = \boldsymbol{r_1}, \boldsymbol{r_2}, \ldots, \boldsymbol{r_N}$ describes the coordinate vectors of the N electrons relative to a molecule-fixed coordinate system, and $\boldsymbol{Q} = \boldsymbol{Q_1}, \ldots, \boldsymbol{Q_M}$ represents the normal coordinates for the M nuclei, excluding rotation and translation. As we separate the nuclear and electrons coordinates we assume the Born-Oppenheimer (adiabatic) approximation. Hence, the Schrödinger equation for the state n:

$$H_{mol}\Psi_n(\boldsymbol{r}, \boldsymbol{Q}) = E_n(\boldsymbol{Q})\Psi_n(\boldsymbol{r}, \boldsymbol{Q}). (\boldsymbol{Q})\Psi_n(\boldsymbol{r}, \boldsymbol{Q}) .$$

The electric field is treated as an ensemble of noninteracting harmonic oscillator modes; the μth mode containing n_μ photons, all having energy $\hbar\omega_\mu$, polarization $\hat{\boldsymbol{e}}_{\boldsymbol{\mu}}$, and propagation $\pm\boldsymbol{k}_{\boldsymbol{\mu}}$. The propagation vector has a magnitude ω_μ/c, where c is the velocity of light. The propagation vector is also orthogonal to the polarization vector, hence:

$$\hat{\boldsymbol{e}}_{\boldsymbol{\mu}} \cdot \boldsymbol{k}_{\boldsymbol{\mu}} = 0.$$

The Hamiltonian for this ensemble is

$$H_{rad} = \sum_{\mu} H_\mu,$$

where

$$H_\mu = \hbar\omega_\mu q_\mu q_\mu^*,$$

and q_μ, q_μ^* are the time-dependent, complex oscillator amplitudes. The unperturbed field eigenfunction is written as a product:

$$\Psi_{rad}(q_1, q_2, \dots) = u_{n_1}(q_1)u_{n_2}(q_2)\dots,$$

where there are n_1 photons of frequency ω_1, polarization $\hat{\boldsymbol{e}}_{\boldsymbol{1}}$, propagation $\pm\boldsymbol{k}_{\boldsymbol{1}}$, etc. The individual oscillator functions satisfy

$$H_\mu u_{n_\mu}(q_\mu) = n_\mu h\omega_\mu u_{n_\mu}(q_\mu),$$

while the total energy of the field is

$$E_{rad} = \sum_\mu n_\mu \hbar\omega_\mu,$$

where the summation is taken over all modes in the ensemble. In general, since photons obey Bose-Einstein statistics the field eigenfunction should be symmetric to exchange of any two coordinated q_μ, q_λ. However, in the following derivation we will consider only two oscillator modes: incident and scattered. The functions $u_n(q)$ are the well-known harmonic oscillator eigenfunctions having the properties

$$\langle u_n | u_m \rangle = \delta_{nm},$$

$$qu_n = \left[\frac{n\hbar}{2\omega}\right]^{\frac{1}{2}} u_{n-1}$$

$$q^* u_n = \left[\frac{(n+1)\hbar}{2\omega}\right]^{\frac{1}{2}} u_{n+1},$$

where q and q^* may be thought as operators that describe photon annihilation and creation, respectively.

The electromagnetic field is described in terms of a vector potential $\boldsymbol{A}$ that satisfies equations:

$$\nabla^2 \boldsymbol{A} - \frac{1}{c^2}\frac{\partial^2 \boldsymbol{A}}{\partial t^2} = 0,$$

$$\text{div}\, \boldsymbol{A} = 0.$$

With the normalization condition

$$\langle \boldsymbol{A_\lambda} | \boldsymbol{A_\mu} \rangle = 4\pi c^2 \delta_{\lambda\mu}$$

we have

$$\boldsymbol{A_\lambda} = [4\pi c^2]^{\frac{1}{2}} \hat{\boldsymbol{e}}_{\boldsymbol{\lambda}} e^{i\boldsymbol{k_\lambda}\cdot\boldsymbol{r}}$$

and

$$\boldsymbol{A} = \sum_{\lambda} \{q_\lambda \boldsymbol{A_\lambda} + q_\lambda^* \boldsymbol{A}^*\}$$

where the sum is taken over all modes if the fields. In our case, for two frequencies ω_0 and ω_f, we can write:

$$A = (4\pi c^2)^{\frac{1}{2}} \left[\hat{\boldsymbol{e}}_{\boldsymbol{0}} \left(q_0 e^{ik_0\cdot r} + q_0^* e^{-ik_0\cdot r}\right) + \hat{\boldsymbol{e}}_{\boldsymbol{f}} \left(q_f e^{ik_f\cdot r} + q_f^* e^{-ik_f\cdot r}\right)\right]. \qquad (B.2)$$

Also, for the derivation we will use the density of photon states ρ_λ per unit energy $d(\hbar\omega_\lambda)$ in the interval $\hbar\omega_\lambda$ to $\hbar\omega_\lambda + d(\hbar\omega_\lambda)$:

$$\rho_\lambda = \frac{\omega_\lambda^2 d\Omega_\lambda}{(2\pi c)^3 \hbar},$$

where we again assume the photon propagation vector $\pm\boldsymbol{k_\lambda}$, solid angle $d\Omega_\lambda$ and periodic boundary conditions.

The interaction between the molecule and the external field is due to the coupling vector potential $\boldsymbol{A}$ with the moving charged particles – electrons of charge – e and mass m_e, nuclei of charge eZ_a and mass M_a. Thus, the momentum operators in the kinetic energy terms in the interaction Hamiltonian (Equation B.1):

$$T_E = \frac{1}{2m_e}\sum_{i=1}^{N} \boldsymbol{p_i^2}$$

and

$$T_A = \sum_{a=1}^{M} \frac{1}{2M_a} \boldsymbol{P_a^2}$$

transform as

$$\boldsymbol{p_i} \rightarrow \left[\boldsymbol{p_i} - \frac{e}{c}\boldsymbol{A}(\boldsymbol{r_i})\right]$$

and

$$\boldsymbol{P_a} \rightarrow \left[\boldsymbol{P_a} + \frac{eZ_a}{c}\boldsymbol{A}(\boldsymbol{Q_a})\right].$$

Accordingly, the additional terms in the Hamiltonian describing the interaction:

$$H' = H'_E + H'_N$$

are the electronic term

$$H'_E = \sum_{i=1}^{N}\left[-\frac{e}{m_e c}\boldsymbol{p_i}\cdot\boldsymbol{A}(\boldsymbol{r_i}) + \frac{e^2}{m_e c^2}\boldsymbol{A^2}(\boldsymbol{r_i})\right]$$

and the nuclear term

$$H'_N = \sum_{a=1}^{M}\left[\frac{eZ_a}{M_a c}\boldsymbol{P_a}\cdot\boldsymbol{A}(\boldsymbol{Q_A}) + \frac{e^2 Z_a^2}{M_a c^2}\boldsymbol{A^2}(\boldsymbol{Q_A})\right]$$

In practice the interaction operator is usually simplified by making the following assumptions: the nuclear term is generally neglected altogether, and the electric dipole approximation is made. The electric dipole approximation assumes that the wavelength of the electromagnetic radiation is much large than the size of a molecule, *i.e.* $|\boldsymbol{k}||\boldsymbol{r}|$ is much less than unity. Hence, in the equation B.2 we have:

$$e^{\pm i\boldsymbol{k}\cdot\boldsymbol{r}} = 1 + (\pm i\boldsymbol{k}\cdot\boldsymbol{r}) + \frac{1}{2}(\pm i\boldsymbol{k}\cdot\boldsymbol{r})^2 + \cdots \approx 1\,.$$

In this approximation the A^2 terms give no contribution to Raman scattering due to the orthogonality with the set of zeroth-order molecular eigenstates.

Now we can move to considering the transition probability for light scattering. We use the Fermi's golden, so the transition probability from the initial state

$$\Psi_0 = \Psi_n(\boldsymbol{r},\boldsymbol{Q})u_{n_0}(q_0)u_{n_f}(q_f)$$

with the energy

$$E_0 = E_n + n_0\hbar\omega_0 + n_f\hbar\omega_f$$

to the final state

$$\Psi_F = \Psi_m(\boldsymbol{r},\boldsymbol{Q})u_{n_0-1}(q_0)u_{n_f+1}(q_f),$$

$$E_F = E_m + (n_0 - 1)\hbar\omega_0 + (n_f + 1)\hbar\omega_f$$

is given by the following expression:

$$W_{F0} = \frac{2\pi}{\hbar}\rho_f|H'|^2.$$

Where, ρ_f is the density of final states for scattered photons and the $|H'|^2$ is the matrix element of the interaction (perturbed) Hamiltonian. It has both terms linear and quadratic

in $\boldsymbol{A}$, *i.e.* the first- and the second-order terms. Hence, as we plug in the interaction Hamiltonian, we obtain the following transition probability

$$W_{F0} = \frac{2\pi}{\hbar}\rho_f \left| H'_{F0} + \sum_{I,II} \left\{ \frac{H'_{FI}H'_{I0}}{E_0 - E_1} + \frac{H'_{FII}H'_{II0}}{E_0 - E_1} \right\} \right|^2 .$$

Here, H'_{F0} is the first order term, the second order term is summed over two types of intermediate states. The first-order term the scattering can be described as simultaneous emission and absorption of photons of frequency ω_0 and ω_f, respectively. The second-order description of scattering involved two types of intermediate states: 1) the photon ω_0 is absorbed and the molecule forms and intermediate state Ψ_r; the photon ω_f is emitted (spontaneously) and the final state Ψ_m is formed; 2) conversely, the molecule may spontaneously emit the photon ω_f and form a different intermediate state $\Psi_{r'}$, the incident photon is absorbed to form the final state. The matrix elements then are:

$$H'_{F0} = \langle \Psi_m u_{n_0-1} u_{n_f+1} | H' | \Psi_n u_{n_0} u_{n_f} \rangle ,$$

$$H'_{FI} = \langle \Psi_m u_{n_0-1} u_{n_f+1} | H' | \Psi_r u_{n_0-1} u_{n_f} \rangle ,$$

$$H'_{I0} = \langle \Psi_r u_{n_0-1} u_{n_f} | H' | \Psi_n u_{n_0} u_{n_f} \rangle ,$$

$$H'_{FII} = \langle \Psi_m u_{n_0-1} u_{n_f+1} | H' | \Psi_r u_{n_0} u_{n_f+1} \rangle ,$$

$$H'_{II0} = \langle \Psi_r u_{n_0} u_{n_f+1} | H' | \Psi_n u_{n_0} u_{n_f} \rangle .$$

At this point it is useful to discuss the approximations we made. The first one was the electric dipole approximation. Consequence of this is that for Raman scattering the first order matrix element and the terms involving $\boldsymbol{A}^2$ in the second order matrix elements are zero. The second approximation is to neglect completely the nuclear term H'_N in the

perturbation operator H'. To use that we again assume the Born-Oppenheimer approximation and harmonic oscillator nuclear wave function. In general, the anharmonicity of the potentials will slight shift the energy levels spacing, so here it can be neglected. Hence, we omit the nuclear-nuclear term which is nonzero only for resulting in Rayleigh scattering and overtone and combinations bands in Raman scattering. The nuclear-electron term, in general, has a small contribution to the scattering process.

Performing the integration over the q variables of radiation space first, and using the relationships for the harmonic oscillator eigenfunctions we obtain for the matrix elements:

$$H'_{FI} = \left[\frac{(n_f+1)\hbar}{2\omega_f}\frac{4\pi e^2}{m_e^2}\right]^{\frac{1}{2}} \langle\Psi_m| - \sum_{i=1}^{N} \boldsymbol{p_i}\cdot\hat{\boldsymbol{e}}_{\boldsymbol{f}}|\Psi_r\rangle,$$

$$H'_{I0} = \left[\frac{n_0\hbar}{2\omega_f}\frac{4\pi e^2}{m_e^2}\right]^{\frac{1}{2}} \langle\Psi_r| - \sum_{i=1}^{N} \boldsymbol{p_i}\cdot\hat{\boldsymbol{e}}_{\boldsymbol{0}}|\Psi_n\rangle,$$

$$H'_{I0} = \left[\frac{n_0\hbar}{2\omega_f}\frac{4\pi e^2}{m_e^2}\right]^{\frac{1}{2}} \langle\Psi_m| - \sum_{i=1}^{N} \boldsymbol{p_i}\cdot\hat{\boldsymbol{e}}_{\boldsymbol{0}}|\Psi_r\rangle,$$

$$H'_{I0} = \left[\frac{(n_f+1)\hbar}{2\omega_f}\frac{4\pi e^2}{m_e^2}\right]^{\frac{1}{2}} \langle\Psi_r| - \sum_{i=1}^{N} \boldsymbol{p_i}\cdot\hat{\boldsymbol{e}}_{\boldsymbol{f}}|\Psi_n\rangle.$$

From here w suppress the sum over i and introduce the notation

$$\boldsymbol{p_{rn}} = \langle\Psi_r(\boldsymbol{r_r}, \boldsymbol{Q_r})|\boldsymbol{p}|\Psi_n(\boldsymbol{r_n}, \boldsymbol{Q_n})\rangle.$$

We note, that the actual coordinates in the ground state n and intermediate state r are different as the wavefunctions Ψ_r and Ψ_n relate to the different potentials. This fact also

affects the energies E_n and E_r, so in the exact calculation one should take into account the actual shift of the potential well ($\boldsymbol{Q}$ coordinates) in the excited or intermediate state.

$$W_{F0} = \frac{2\pi}{\hbar}\rho_f \left[\frac{(n_f+1)\hbar}{2\omega_f}\frac{n_0\hbar}{2\omega_0}\right]\frac{2^4\pi^2e^4}{m_e^4} \times \left|\sum_r \left\{\frac{\boldsymbol{p_{mr}}\cdot\hat{\boldsymbol{e}}_{\boldsymbol{f}}\,\boldsymbol{p_{rn}}\cdot\hat{\boldsymbol{e}}_{\boldsymbol{0}}}{E_n - E_r + \hbar\omega_0} + \frac{\boldsymbol{p_{mr}}\cdot\hat{\boldsymbol{e}}_{\boldsymbol{0}}\,\boldsymbol{p_{rn}}\cdot\hat{\boldsymbol{e}}_{\boldsymbol{f}}}{E_n - E_r - \hbar\omega_0}\right\}\right|^2.$$

Then, introducing the expression for density of states ρ_f and setting $n_f = 0$ (spontaneous Scattering), we have the transition probability for the Raman process with the incident photon beam being inelastically scattered into the solid angle $d\Omega_\mathrm{f}$ as

$$W_{F0}d\Omega_\mathrm{f} = \frac{\omega_f}{\omega_0}\frac{n_0e^4}{c^3m_e^4} \times \left|\sum_r \left\{\frac{\boldsymbol{p_{mr}}\cdot\hat{\boldsymbol{e}}_{\boldsymbol{f}}\,\boldsymbol{p_{rn}}\cdot\hat{\boldsymbol{e}}_{\boldsymbol{0}}}{E_n - E_r + \hbar\omega_0} + \frac{\boldsymbol{p_{mr}}\cdot\hat{\boldsymbol{e}}_{\boldsymbol{0}}\,\boldsymbol{p_{rn}}\cdot\hat{\boldsymbol{e}}_{\boldsymbol{f}}}{E_n - E_r - \hbar\omega_0}\right\}\right|^2 d\Omega_\mathrm{f}.$$

Now, by taking $n_0 = 1$, *i.e.* a single photon scattering and dividing by the relative velocity of incident flux (approximately c) we obtain collision cross section (Kramers-Heisenberg-Dirac formula):

$$\frac{d\sigma}{d\Omega} = \frac{\omega_f}{\omega_0}\frac{e^4}{c^4m_e^4}\left|\sum_r \left\{\frac{\boldsymbol{p_{mr}}\cdot\hat{\boldsymbol{e}}_{\boldsymbol{f}}\,\boldsymbol{p_{rn}}\cdot\hat{\boldsymbol{e}}_{\boldsymbol{0}}}{E_n - E_r + \hbar\omega_0} + \frac{\boldsymbol{p_{mr}}\cdot\hat{\boldsymbol{e}}_{\boldsymbol{0}}\,\boldsymbol{p_{rn}}\cdot\hat{\boldsymbol{e}}_{\boldsymbol{f}}}{E_m - E_r - \hbar\omega_0}\right\}\right|^2.$$

or, using an expression for classical electron radius $r_0 = e^2/mc^2$:

$$\frac{d\sigma}{d\Omega} = \frac{\omega_f}{\omega_0}r_0^2\left|\frac{1}{m_e}\sum_r \left\{\frac{\boldsymbol{p_{mr}}\cdot\hat{\boldsymbol{e}}_{\boldsymbol{f}}\,\boldsymbol{p_{rn}}\cdot\hat{\boldsymbol{e}}_{\boldsymbol{0}}}{E_n - E_r + \hbar\omega_0} + \frac{\boldsymbol{p_{mr}}\cdot\hat{\boldsymbol{e}}_{\boldsymbol{0}}\,\boldsymbol{p_{rn}}\cdot\hat{\boldsymbol{e}}_{\boldsymbol{f}}}{E_m - E_r - \hbar\omega_0}\right\}\right|^2.$$

As we neglected the finite width of the intermediate state r in our derivation, the denominator turns into zero at the resonant case $\hbar\omega_0 = E_n - E_r$. The lifetime Γ_r factors can be manually added to the final expression, so it will match the form in equation 1.3 and solve this problem.

To get an estimation for order of its values we can assume the same polarization for the incident and emitted light and average over molecular orientations:

$$\frac{d\sigma}{d\Omega} \approx 4\pi \frac{\omega_f}{\omega_0} r_0^2 \left| \frac{1}{m_e} \sum_r \boldsymbol{p_{mr}}\, \boldsymbol{p_{rn}} [(E_n - E_r + \hbar\omega_0)^{-1} + (E_m - E_r - \hbar\omega_0)^{-1}] \right|^2 .$$

Sometimes it is more convenient to use the dipole length form of matrix elements $\boldsymbol{r_{mn}}$, instead of dipole momentum form used here. Then, we obtain

$$\frac{d\sigma}{d\Omega} = 4\pi \frac{\omega_f}{\omega_0} r_0^2 \left| \frac{1}{m_e} \omega_0 \omega_f \frac{m_e}{e} \frac{m_e}{e} \sum_r \boldsymbol{r_{mr} r_{rn}} [(E_{nr} + \hbar\omega_0)^{-1} + (E_{mr} - \hbar\omega_0)^{-1}] \right|^2 ,$$

$$\frac{d\sigma}{d\Omega} = 4\pi \omega_0 \omega_f^3 r_0^2 \left| \frac{m_e}{e^2} \sum_r \boldsymbol{r_{mr} r_{rn}} [(E_{nr} + \hbar\omega_0)^{-1} + (E_{mr} - \hbar\omega_0)^{-1}] \right|^2 .$$

Or, alternatively:

$$\frac{d\sigma}{d\Omega} = 4\pi \frac{\omega_0 \omega_f^3}{c^4} \left| e^2 \sum_r \boldsymbol{r_{mr} r_{rn}} [(E_{nr} + \hbar\omega_0)^{-1} + (E_{mr} - \hbar\omega_0)^{-1}] \right|^2 . \qquad (B.3)$$

The usage of e^2 inside the sum is explained by the fact, that the conventional units for the transition dipole moment matrix elements are statC*cm or Debye = 10^{-18} statC*cm. To verify this result (equation B.3) we perform the dimensionality check:

$$cm^2 = \sec^{-4} cm^{-4} \sec^4 \times statC^4\, cm^4 erg^{-2}$$

$$cm^2 = (statC^2 erg^{-1})^2 = (statC^2\, statC^{-2}\, cm^1)^2 = cm^2$$

Finally, we will get an order of magnitude estimation for the cross section values. Let us assume the scattering of a single photon having wavelength 600 nm, or the frequency $\omega_0 = 2\pi \times 5 \times 10^{14}\ Hz$. Assuming the pure vibrational transition, which are

typically on the order of $\tilde{\nu}\sim 1600\ cm^{-1} = 2\pi \times 5 \times 10^{13}\ Hz.$, we have $\omega_f = \omega_0 + \tilde{\nu} \approx \omega_0$. The term outside the sum in the equation B.3 is then equals:

$$4\pi \frac{\omega_0 \omega_f^3}{c^4} = 8\pi^5 \times (0.5 \times 10^{14} \times 3 \times 10^{-10})^4\ cm^{-4} \approx 10^4 \times 10^{16} cm^{-4} = 10^{20}\ cm^{-4}.$$

To estimate the summation term, we can assume that the energies $E_{nr} = E_n - E_r$ and $E_{mr} = E_m - E_r$ are much higher than the photon energy $\hbar\omega_0$. This is valid when we consider the off-resonant case. For instance, the electron energy levels for diatomic gases are on the order of 10 eV or $1.6 \times 10^{-12}\ erg$. Now, assuming the typical transition dipole moment value 1 $D = 10^{-18}\ statC \cdot cm$, we have then:

$$\left| e^2 \sum_r \boldsymbol{r_{mr} r_{rn}} [(E_{nr} + \hbar\omega_0)^{-1} + (E_{mr} - \hbar\omega_0)^{-1}] \right|^2 \sim$$

$$\sim \left| 2 \times \frac{10^{-18} statC \cdot cm \times 10^{-18} statC \cdot cm}{1.6 \times 10^{-11}\ erg} \right|^2 \approx 10^{-50} cm^6$$

Finally, we can estimate the differential Raman cross section:

$$\frac{d\sigma}{d\Omega} \sim 10^{20} cm^{-4} \times 10^{-50} cm^6 = 10^{-30}\ cm^2.$$

Although we made several approximations and simplifications, this estimation rather well corresponds to the experimentally measured cross sections. For instance, for the value for the experimentally obtained cross section for N_2 molecule and pure vibrational transition at 337.1 nm is $39 \times 10^{-30}\ cm^2$, which according to the ω^4 scaling at 600 nm becomes $3.9 \times 10^{-30}\ cm^2$. In the Appendix C we will make some additional estimations for the cross section values and also estimate the relative intensities one can expect to obtain in the real world experiment.

APPENDIX C

EXPERIMENTALLY OBTAINED RAMAN SCATTERING CROSS SECTION VALUES

As it was discussed in the Section 1.3 and in Appendixes A and B, the value of Raman scattering cross section depends on the frequency of electromagnetic radiation ($\sim\omega^4$ dependence) and values of the transition dipole moments incorporated into the molecular polarizability α. To demonstrate the orders of magnitude using classical theory and compare it with experimental values of Raman scattering cross sections let us perform the following analysis using SI units.

Let us first consider an off-resonant case. The general differential scattering cross section (m^2 sr^{-1} $molecule^{-1}$) can be defined as following:

$$\sigma' = \frac{I}{F},$$

where I – the power of scattered (Raman of Rayleigh) light in W sr^{-1} $molecule^{-1}$ and F is the irradiance of the incident radiation in W m^2. The scattering cross section is related to the transition polarizability:

$$\sigma' = K\omega^4 \left|\alpha_{G,F}\right|^2$$

and constant K because of SI units has dimensionality of C^{-2} V^2 sec^4. Since Raman spectrum are typically shown using cm^{-1} units, it is convenient to switch to the frequency in m^{-1} $\tilde{\nu} = \omega/2\pi c$, where c is the speed of light in vacuum. Then the scattering cross section becomes:

$$\sigma'(\tilde{\nu}) = K_{\tilde{\nu}}\, \tilde{\nu}^4 \left|\alpha_{G,F}\right|^2.$$

The constant $K_{\tilde{\nu}}$ average over all molecule orientations has the value 1.3×10^{23} and units (SI) $C^{-2}\,V^2\,m^2$. Hence, to evaluate the scattering cross section, we can take the typical value of polarizability for diatomic nitrogen [26]: $4.5 \times 10^{-26}\ cm^3 \times 4\pi\varepsilon_0 \times 10^6 \approx 5 \times 10^{-42} C\ V^{-1} m^2$. We can then consider Q-branch Stokes scattering of nitrogen molecule (pure vibrational with $\Delta\nu = 2331$ cm^{-1}) using 337.1 nm excitation wavelength, thus, $\tilde{\nu}^4$ having a value of 3.2×10^{-6} m^{-1}. Hence, the scattering cross section has a value 3.4×10^{-34} m^2 sr^{-1} molecule^{-1}, which is very close to the experimentally observed value of 3.1×10^{-34} m^2 sr^{-1} molecule^{-1} (see, for example, [22]) and the estimation made in the Appendix B.

Now we will consider the scattering intensity I. Let us assume the irradiance of the order 10^{10} W m^{-2}, which can be achieved by focusing 1 W laser to a spot with an area of 10^{-10} m^2 (focal spot diameter $\approx 10^{-5}$ m^2). Then we obtain intensity $I = 3.4 \times 10^{-24}$ W sr^{-1} per molecule. A typical focal volume 10^{-12} m^3 contains approximately 3×10^{13} molecules of gas (such as nitrogen) at standard temperature and pressure. Hence, the total scattered power is on the order of 10^{-7} W or 0.1 μW. At the same time, as the scattering photon energy is 4 eV or 6.4×10^{-19} J, we can expect scattering of the order of 10^8 photons per steradian per second. Although Raman scattering generate relatively low powers, these levels of signal nowadays can be easily detected by widely available photodiodes, CCD detectors and photo multiplier tubes.

Finally, we briefly mention the typical values of enhancements provided by the resonance effects. While the determination of exact values will require to consider the specific electronic molecular structure, we can get an order of magnitude estimate by

considering the experimental values of Raman scattering cross sections obtained for NH_4NO_3 (ammonium nitrate) by Ghosh *et al.* [66]. As we can see from Table 1 in their work, the values of cross section for excitation with the laser having 257 nm wavelength are on the order 0.1—0.3 10^{-30} cm^2 per molecule per steradian. However, for the 204 nm excitation wavelength, these values are 30-70 times larger! Obviously, these scaling cannot be explained solely by ω^4 scaling, as one would expect only 2.5 enhancement in this case. Hence, we can conclude that 10-100 times stronger signals are provided by the resonance enhancements and are easily achievable under real experimental conditions.